



HAL
open science

Modelling the Madden-Julian oscillation during its passage over the Indian Ocean and the Maritime continent

Daria Kuznetsova

► **To cite this version:**

Daria Kuznetsova. Modelling the Madden-Julian oscillation during its passage over the Indian Ocean and the Maritime continent. Meteorology. Université Paul Sabatier - Toulouse III, 2018. English. NNT : 2018TOU30220 . tel-02316247

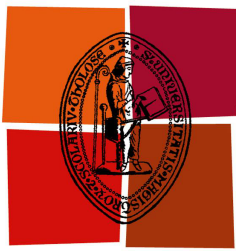
HAL Id: tel-02316247

<https://theses.hal.science/tel-02316247v1>

Submitted on 15 Oct 2019

HAL is a multi-disciplinary open access archive for the deposit and dissemination of scientific research documents, whether they are published or not. The documents may come from teaching and research institutions in France or abroad, or from public or private research centers.

L'archive ouverte pluridisciplinaire **HAL**, est destinée au dépôt et à la diffusion de documents scientifiques de niveau recherche, publiés ou non, émanant des établissements d'enseignement et de recherche français ou étrangers, des laboratoires publics ou privés.



Université
de Toulouse

THÈSE

En vue de l'obtention du

DOCTORAT DE L'UNIVERSITÉ DE TOULOUSE

Délivré par : *l'Université Toulouse 3 Paul Sabatier (UT3 Paul Sabatier)*

Présentée et soutenue le 18/09/2018 par :

Daria Kuznetsova

**Modélisation de l'oscillation Madden-Julian
lors de son passage sur l'océan Indien et le continent maritime
(Modelling the Madden-Julian oscillation
during its passage over the Indian Ocean
and the Maritime Continent)**

JURY

FRANK ROUX	LA, Toulouse	Président du Jury
CHRISTELLE BARTHE	LACy, La Réunion	Rapporteuse
SOPHIE BASTIN	LATMOS, Guyancourt	Rapporteuse
PETER HAYNES	DAMPT, Cambridge	Rapporteur
DOMINIQUE BOUNIOL	CNRM, Toulouse	Examinatrice
JEAN-PIERRE CHABOUREAU	LA, Toulouse	Directeur de thèse

École doctorale et spécialité :

SDU2E : Océan, Atmosphère, Climat

Unité de Recherche :

Laboratoire d'Aérodynamique, Université de Toulouse, CNRS, UPS

Directeur de Thèse :

Jean-Pierre Chaboureau

Rapporteurs :

Christelle Barthe, Sophie Bastin et Peter Haynes

*Modelling the Madden–Julian
oscillation
during its passage over the Indian
Ocean and the Maritime Continent*

Author:

Daria KUZNETSOVA

Supervisor:

Jean-Pierre CHABOUREAU

Preface

Going abroad for studies was a big step for me and I want to thank all people who made it possible. I am very grateful to everyone in Laboratoire d'Aérodynamique (LA)/ Observatoire Midi-Pyrénées/ Université Paul Sabatier (UPS) for welcoming me in Toulouse.

Thanks to the French Ministry of Higher Education and Research (Ministère de l'Enseignement supérieur et de la Recherche) for providing me a Ph.D. student scholarship.

Thanks to the LA directors Céline Mari and Frank Roux and to the Doctoral School "Sciences de l'Univers, de l'Espace et de l'Environnement" (SDU2E) directors Geneviève Soucail and Patrick Mascart, as well as to the assistant director Stéphane Bonnet.

Thanks to my advisor Jean-Pierre Chaboureau (LA) for introducing me to the subject of meteorology that I had previously known nothing about, and for giving me an opportunity to learn a lot.

Thanks to my thesis defense committee members: Frank Roux (LA), Christelle Barthe (LACy, La Réunion), Sophie Bastin (LATMOS, Guyancourt), Peter Haynes (DAMPT, Cambridge), Dominique Bouniol (CNRM, Toulouse). Their valuable remarks and comments helped to improve this manuscript.

Thanks to Chantal Claud (LMD, Paris) and Dominique Bouniol for being in my thesis evaluation committee during these three years, their feedback was of a great help for me.

Thanks to many others for reviewing and discussing my work, especially to Frank Roux, Eric Defer, Evelyne Richard. Also, thanks to the students, postdocs and interns, especially to Thibaut Dauhut and Irene Reinares Martínez for their

explanations and assistance, as well as to Laurent Labbouz, Nicolas Blanchard, Keun-Ok Lee, Léo Seyfried, Flore Tocquer, Phillip Scheffknecht and many others.

Thanks to the IT support team for their assistance.

Thanks to all the administrative support staff for their help in arranging the paperwork, especially to Karine Mercadier (LA), Marie-Claude Cathala (SDU2E), and Catherine Stasiulis (UPS).

Many thanks to Marisa Vialet (LA) for her constant encouragement, help and advices.

Also, special thanks go to Olga Krivonosova and Dmitriy Zhilenko from the Institute of Mechanics of Moscow State University, and to Maria Gritsevich from the University of Helsinki, for their support and discussions.

Getting to love science in all its forms is a life journey. I want to thank with all my heart my family, friends, and generally — every person who inspired me, helped me and motivated me on this journey, be it many years ago or during these three years of my Ph.D. studies.

I would like to finish this preface with beautiful words spoken by the person whose passion for science and whose views of the world have inspired so many people.

Carl Sagan, “Pale Blue Dot,” 1994 – about an image of the Earth taken by Voyager 1 spacecraft on 14 February, 1990.

Look again at that dot. That’s here. That’s home. That’s us. On it everyone you love, everyone you know, everyone you ever heard of, every human being who ever was, lived out their lives. The aggregate of our joy and suffering, thousands of confident religions, ideologies, and economic doctrines, every hunter and forager, every hero and coward, every creator and destroyer of civilization, every king and peasant, every young couple in love, every mother and father, hopeful child, inventor

and explorer, every teacher of morals, every corrupt politician, every “superstar,” every “supreme leader,” every saint and sinner in the history of our species lived there — on a mote of dust suspended in a sunbeam.

The Earth is a very small stage in a vast cosmic arena. Think of the rivers of blood spilled by all those generals and emperors so that, in glory and triumph, they could become the momentary masters of a fraction of a dot. Think of the endless cruelties visited by the inhabitants of one corner of this pixel on the scarcely distinguishable inhabitants of some other corner, how frequent their misunderstandings, how eager they are to kill one another, how fervent their hatreds.

Our posturings, our imagined self-importance, the delusion that we have some privileged position in the Universe, are challenged by this point of pale light. Our planet is a lonely speck in the great enveloping cosmic dark. In our obscurity, in all this vastness, there is no hint that help will come from elsewhere to save us from ourselves.

The Earth is the only world known so far to harbor life. There is nowhere else, at least in the near future, to which our species could migrate. Visit, yes. Settle, not yet. Like it or not, for the moment the Earth is where we make our stand.

It has been said that astronomy is a humbling and character-building experience. There is perhaps no better demonstration of the folly of human conceits than this distant image of our tiny world. To me, it underscores our responsibility to deal more kindly with one another, and to preserve and cherish the pale blue dot, the only home we’ve ever known.

Abstract

The Madden–Julian Oscillation (MJO) is the dominant component of the intraseasonal variability in the tropical atmosphere, propagating eastward in the equatorial band. It consists of a convective center (active phase) accompanied by the low-level zonal wind anomaly convergence and the upper-level zonal wind anomaly divergence, and zones of weak convection (suppressed phases). Three time periods of the MJO activity over the Indian Ocean and the Maritime Continent were chosen: 6–14 April 2009, 23–30 November 2011, and 9–28 February 2013. The simulations with and without convective parameterizations were performed for a large domain with the atmospheric model Méso-NH. It was obtained that the simulations with parameterized convection were not able to reproduce an MJO signal. For 2009 and 2011 when the coupling between convection and large-scale circulation was strong, the convection-permitting simulations showed a visible MJO propagation, which was not the case for 2013. For the 2011 episode, the processes contributing to the suppression of the convection were studied using an isentropic analysis to separate the ascending air masses with high equivalent potential temperature from the subsiding air masses with low equivalent potential temperature. Three large-scale circulations were found: a tropospheric circulation, an overshoot circulation within the tropical tropopause layer, and a circulation of air masses with low equivalent potential temperature in the lower troposphere. The latter corresponds to the large-scale dry air intrusions from the subtropical zones into the equatorial band, mostly found during the suppressed MJO phase over the Indian Ocean.

Résumé

L'oscillation de Madden–Julian (MJO) est la composante dominante de la variabilité intrasaisonnière dans l'atmosphère tropicale, se propageant vers l'est dans la bande équatoriale. Elle se compose d'un centre convectif (phase active) accompagné de la convergence des anomalies du vent zonal de bas niveau et de la divergence de niveau supérieur, et de zones de convection faible (phases supprimées). Trois périodes de l'activité MJO sur l'océan Indien et le continent maritime ont été choisies : 6–14 avril 2009, 23–30 novembre 2011 et 9–28 février 2013. Les simulations avec et sans paramétrisation de la convection ont été réalisées pour un grand domaine avec le modèle atmosphérique Méso-NH. Il a été obtenu que les simulations avec convection paramétrée n'étaient pas capables de reproduire un signal MJO. Pour 2009 et 2011, lorsque le couplage entre la convection et la circulation de grande échelle était fort, les simulations avec convection explicite ont montré une propagation visible de la MJO, ce qui n'a pas été le cas pour 2013. Pour 2011, les processus contribuant à la suppression de la convection ont été étudiés avec une analyse isentropique pour séparer les masses d'air ascendantes ayant une température potentielle équivalente élevée des masses d'air subsidentes ayant une température potentielle équivalente faible. Trois circulations de grande échelle ont été trouvées : une circulation troposphérique, une circulation de percées nuageuses dans la couche de tropopause tropicale, et une circulation de masses d'air à faible température potentielle équivalente dans la basse troposphère. Cette dernière correspond aux intrusions d'air sec de grande échelle des zones subtropicales dans la bande équatoriale, trouvées principalement pendant la phase supprimée de la MJO sur l'océan Indien.

Table of Contents

Introduction	1
Introduction (en français)	7
1 The Madden–Julian oscillation	13
1.1 Overview of the MJO	14
1.2 Processes governing the evolution of the MJO	24
1.3 Observations and simulations of the MJO	27
2 Model, data and methods	37
2.1 The Méso-NH model	38
2.2 Simulations with the Méso-NH model	47
2.3 Other datasets	51
3 Assessment of the Méso-NH simulations	55
3.1 Overview of the MJO events	57
3.2 Simulations of three MJO events	59
3.3 Sensitivity of the 2011 simulation to the cloud fraction and turbulence parameterizations	91
4 Atmospheric overturning during the MJO	103
4.1 Introduction	104
4.2 Article: The three atmospheric circulations over the Indian Ocean and the Maritime Continent and their modulation by the passage of the MJO	106
4.3 Discussion	144
Conclusions and perspectives	155
Conclusions et perspectives (en français)	161
References	167

Introduction

A remarkable characteristic of the tropical convection and circulation is their possibility to organize into large-scale patterns. The most important such pattern in the tropical atmosphere is the Madden–Julian Oscillation (MJO), a planetary-scale phenomenon with the zonal extent of the order of 10000 km. The MJO is represented by the coupled signals in atmospheric circulation and deep convection, which move eastward over the Indian and Pacific Oceans having a local intraseasonal period of 30-90 days. It can be distinguished in particular as an eastward-propagating spatial configuration consisting of intensified and suppressed precipitation, accompanied by a coherent signature in cloudiness, lower- and upper-level wind, and many other fields such as the sea surface temperature and the evaporation at the surface of the ocean (Madden and Julian, 1971, 1972; Zhang, 2005).

The MJO is the dominant component of the intraseasonal variability in the tropical atmosphere. It interacts with convection on different scales, giving a broad influence on different local and global weather and climate phenomena such as rainfall patterns (Donald et al., 2006), active and break monsoon cycles (Goswami, 2005; Pai et al., 2011), tropical cyclone activity (Liebmann et al., 1994; Klotzbach, 2014; Duvel, 2015), El Niño–Southern Oscillation (ENSO) (Moore and Kleeman, 1999; Kapur et al., 2012) and so on. The influence of the

MJO extends to higher latitudes through teleconnections creating such phenomena as flooding, wildfires, lightning, cold air outbreaks and heat waves, stratospheric water vapor and aerosols transport, as described in the review of Zhang (2013). Thus, the MJO might influence the occurrence of extreme precipitation events in North America (Higgins et al., 2000), can modulate the Arctic sea ice (Henderson et al., 2014), interact with the Arctic Oscillation (Zhou and Miller, 2005; L'Heureux and Higgins, 2008) and North Atlantic Oscillation (Casou, 2008), influence the Antarctic circumpolar transport and the atmospheric Southern Annular Mode (Matthews and Meredith, 2004). Given such a broad influence of the MJO on the weather and climate, studying its fundamental properties is therefore crucial for our understanding of the physics of the tropical atmosphere.

Different theories link the MJO initiation and propagation with such processes as convective heating, surface evaporation, interactions with the midlatitudes, boundary layer moisture convergence, Kelvin or Rossby waves (Wang, 2005; Zhang, 2005). At the same time, there is no agreement in explaining the MJO properties e.g. its period/frequency or propagation speed, as well as in defining the driving processes of the MJO. The MJO has been a subject of numerous studies, programs, and campaigns that were dedicated to the exploration of the MJO characteristics and the improvement of the MJO simulations and predictions. For example, the MJO Working Group (MJOWG) was established by the US Climate Variability and Predictability Program (CLIVAR) and was active in 2006–2009. Its activity continued further in 2010–2013 by forming of the MJO Task Force (TF) which was included into the Year of Tropical Convection (YOTC) program. The diagnostics (“set of metrics”) were developed for assessing the model performance in the MJO simulations (CLIVAR Madden–Julian Oscillation Working Group: Waliser et al., 2009). A number of large field campaigns dedi-

cated to the MJO took place with the objective to gather in-situ atmospheric and oceanic data over the equatorial Indian and western Pacific Ocean, such as TOGA COARE (Tropical Ocean and Global Atmosphere Coupled Ocean–Atmosphere Response Experiment) in 1992–1993 (e.g. Webster and Lukas, 1992; Godfrey et al., 1998), MISMO (Mirai Indian Ocean Cruise for the Study of the MJO Onset) in 2006 (e.g. Yoneyama et al., 2008), CINDY/DYNAMO/AMIE (Cooperative Indian Ocean Experiment on Intraseasonal Variability/Dynamics of the Madden–Julian Oscillation/Atmospheric Radiation Measurement Program MJO Investigation Experiment) (e.g. Yoneyama et al., 2013; Zhang et al., 2013; Zhang and Yoneyama, 2017) in 2011–2012. This resulted in the creation of an extensive database, nevertheless, many questions still remain unresolved.

The numerical simulations of the MJO still are not always able to reproduce a visible MJO signal. Global climate models with the coarse horizontal grid spacing have difficulties in reproducing a realistic signal of the MJO, sometimes they can not even reproduce its eastward propagation (Slingo et al., 1996). One of the reasons is the parameterization of the convection in such models. Thus, the subgrid-scale processes associated with convection are approximated resulting in large biases. In contrast, the convection-permitting models with the horizontal resolution ~ 1 km allow the convection to be resolved, and the topographic features are more precisely described. This gives these models a potential for the improvement of the MJO simulation and thus, a possibility for the better comprehension of this phenomenon.

The objective of this thesis is to describe the evolution of the atmosphere and the changes in the convective activity during the passage of the MJO, and to demonstrate the processes that are contributing to its propagation. Several simulations are performed by means of the atmospheric model Méso-NH (Lafore et al., 1998; Lac et al., 2018) over a large domain covering the Indian Ocean and

the Maritime Continent. To find out how the resolution and the representation of convection influences the MJO simulation, the model is run at low resolution where convection is parameterized, and at high resolution where convection is explicit. Three MJO episodes are considered: (1) 6–14 April 2009, (2) 23–30 November 2011, and (3) 9–28 February 2013. These cases correspond to the periods when the MJO was active over the Indian Ocean and the Maritime Continent, where the MJO is generally the most visible. The evaluation of the simulations is performed using a satellite precipitation product and the ECMWF analyses.

The manuscript is organized into the four major sections. In chapter 1, a general overview of the MJO is given. The notions necessary to understand the context of this thesis are introduced, and the ways to identify the MJO signal in observations or simulations are presented. The existing hypotheses concerning the processes contributing to the MJO evolution are explained, and the representation of the MJO in the numerical models is discussed.

In chapter 2, the cases of study are presented. The non-hydrostatic mesoscale atmospheric model Méso-NH is described with the configurations necessary for the performing of the simulations. Two different types of simulations are presented: the low-resolution simulations with the parameterized convection and the high-resolution convection-permitting simulations. The datasets used for the evaluation of the simulations are described.

Chapter 3 presents the evaluation of the simulations. The results of the simulations with the parameterized convection are compared with those of the convection-permitting simulations as well as with the “reference” datasets. The sensitivity of the convection-permitting simulation to the turbulence scheme and the subgrid-scale cloud fraction parameterization is examined for the episode of 23–30 November 2011.

The dry air intrusions during the MJO propagation are discussed in chapter 4. The isentropic method used in this study is presented. Its principles are discussed, and it is explained how the atmospheric circulations of air masses can be described in terms of the isentropic diagrams. The application for the analysis of the evolution of the atmospheric circulations that exist during the passage of the MJO is shown. The results are presented in the article *The three atmospheric circulations over the Indian Ocean and the Maritime Continent and their modulation by the passage of the MJO* under review in *Journal of the Atmospheric Sciences*.

Finally, the conclusions are given, and some perspectives for future work are proposed.

Introduction (en français)

Une caractéristique remarquable de la convection et de la circulation dans les tropiques est leur possibilité de s'organiser en structures de grande échelle. La structure la plus importante dans l'atmosphère tropicale est l'oscillation de Madden–Julian (MJO) qui est un phénomène à l'échelle planétaire avec une étendue zonale de l'ordre de 10000 km. La MJO est représentée par des signaux couplés dans la circulation atmosphérique et la convection profonde, qui se déplacent vers l'est au-dessus des océans Indien et Pacifique avec une période intrasaisonnière locale de 30 à 90 jours. En particulier, elle peut être décrite comme une alternance entre des zones de précipitations intensifiées et de précipitations réduites, accompagnée d'une signature cohérente dans les nuages, les vents troposphériques dans les basses et les hautes couches et de nombreux autres champs comme la température de surface de la mer et l'évaporation à la surface de l'océan (Madden and Julian, 1971, 1972; Zhang, 2005).

La MJO est la composante dominante de la variabilité intrasaisonnière dans l'atmosphère tropicale. Elle interagit avec la convection à différentes échelles, donnant une large influence sur différents phénomènes météorologiques et climatiques locaux et globaux tels que les précipitations (Donald et al., 2006), les moussons (Goswami, 2005; Pai et al., 2011), la cyclogénèse (Liebmann et al., 1994; Klotzbach, 2014; Duvel, 2015), la El Niño–Southern Oscillation (ENSO)

(Moore and Kleeman, 1999; Kapur et al., 2012) etc. L'influence de la MJO s'étend à des latitudes plus hautes par le biais des téléconnexions qui créent des phénomènes tels que les inondations, les feux de forêts, les éclairs, les vagues de froid et de chaleur, le transport de vapeur d'eau et d'aérosols dans la stratosphère, comme décrit dans la revue de Zhang (2013). Par conséquent, la MJO pourrait influencer l'occurrence des précipitations extrêmes en Amérique du Nord (Higgins et al., 2000), moduler la banquise arctique (Henderson et al., 2014), interagir avec l'oscillation arctique (Zhou and Miller, 2005; L'Heureux and Higgins, 2008) et l'oscillation nord-atlantique (Cassou, 2008), influencer le transport circumpolaire antarctique et le mode annulaire austral (Matthews and Meredith, 2004). Puisque la MJO a une influence importante sur la météorologie et le climat, l'étude de ses propriétés fondamentales est donc cruciale pour notre compréhension de la physique de l'atmosphère.

Différentes théories relient l'initiation et la propagation de MJO à des processus tels que le chauffage par convection, l'évaporation de surface, les interactions avec les latitudes moyennes, la convergence de l'humidité de la couche limite, les ondes de Kelvin ou de Rossby (Wang, 2005; Zhang, 2005). En même temps, il n'y a pas d'accord pour expliquer les propriétés de la MJO, par ex. sa période / fréquence ou vitesse de propagation, ni pour définir les processus de pilotage de la MJO. La MJO a fait l'objet de nombreuses études, programmes et campagnes consacrés à l'exploration de ses caractéristiques et à l'amélioration de ses simulations et de sa prévision. Par exemple, le Groupe de travail sur la MJO (MJO Working Group, MJOWG) a été créé par le Programme américain de variabilité et de prévisibilité du climat (Climate Variability and Predictability, CLIVAR) et a été actif en 2006–2009. Son activité s'est poursuivie en 2010–2013 avec la création de la Task Force MJO (TF) qui a été incluse dans le programme YOTC (Year of Tropical Convection). Les diagnostics ont été développés pour

évaluer la performance des modèles dans les simulations de la MJO (Waliser et al., 2009)). Des grandes campagnes de terrain dédiées à la MJO ont eu lieu dans le but de recueillir des données atmosphériques et océaniques in situ sur les régions équatoriales de l’océan Indien et Pacifique Ouest, telles que TOGA COARE (Tropical Ocean and Global Atmosphere Coupled Ocean–Atmosphere Response Experiment) en 1992–1993 (e.g. Webster and Lukas, 1992; Godfrey et al., 1998), MISMO (Mirai Indian Ocean Cruise for the Study of the MJO Onset) en 2006 (e.g. Yoneyama et al., 2008), CINDY/DYNAMO/AMIE (Cooperative Indian Ocean Experiment on Intraseasonal Variability/Dynamics of the Madden–Julian Oscillation/Atmospheric Radiation Measurement Program MJO Investigation Experiment) (e.g. Yoneyama et al., 2013; Zhang et al., 2013; Zhang and Yoneyama, 2017) en 2011–2012. Cela a permis de créer une base de données étendue, mais de nombreuses questions restent toujours sans réponses.

Les simulations numériques de la MJO ne sont pas toujours capables de reproduire un signal MJO visible. Les modèles climatiques globaux avec un espacement grossier de la grille horizontale ont des difficultés à reproduire un signal réaliste de la MJO, parfois ils ne peuvent même pas reproduire sa propagation vers l’est (Slingo et al., 1996). L’une des raisons est la paramétrisation de la convection dans de tels modèles, ainsi les processus d’échelle sous-maille associés à la convection sont approchés, ce qui conduit à des biais importants. En revanche, les modèles permettant la convection avec une résolution horizontale ~ 1 km permettent de résoudre la convection et de décrire plus précisément les caractéristiques topographiques. Cela donne à ces modèles le potentiel de mieux simuler la MJO et donc la possibilité d’une meilleure compréhension de ce phénomène.

L’objectif de cette thèse est de décrire l’évolution de l’atmosphère et les changements dans l’activité convective lors du passage du MJO et de montrer les

processus qui contribuent à sa propagation. Pour ce faire, plusieurs simulations sont effectuées à l'aide du modèle atmosphérique Méso-NH (Lafore et al., 1998; Lac et al., 2018) sur un vaste domaine couvrant l'océan Indien et le continent maritime. Pour déterminer comment la résolution influence la représentation de la MJO, le modèle est lancé à basse résolution où la convection est paramétrée, et à haute résolution où la convection est explicitement représentée. Trois épisodes MJO sont examinés: (1) du 6 au 14 avril 2009, (2) du 23 au 30 novembre 2011 et (3) du 9 au 28 février 2013. Ces cas correspondent aux périodes pendant lesquelles la MJO était active sur l'océan Indien et le continent maritime, où la MJO est généralement la plus visible. L'évaluation des simulations est réalisée à l'aide du produit de précipitation satellitaire et des analyses ECMWF.

Le manuscrit est organisé en quatre sections principales. Dans le chapitre 1, un aperçu général de la MJO est donné. Les notions nécessaires à la compréhension du contexte de cette thèse sont présentées et les moyens d'identifier le signal MJO dans les observations ou les simulations sont présentés. Les hypothèses existantes concernant les processus contribuant à l'évolution de la MJO sont expliquées et la représentation de la MJO dans les modèles numériques est discutée.

Dans le chapitre 2, les cas d'étude sont présentés. Le modèle méso-échelle atmosphérique non-hydrostatique Méso-NH est décrit avec les configurations nécessaires pour l'exécution des simulations. Deux types différents de simulations sont présentés : les simulations à basse résolution avec convection paramétrée et les simulations à haute résolution avec convection résolue. Les jeux de données utilisés pour l'évaluation des simulations sont également décrits.

Le chapitre 3 présente l'évaluation des simulations. Les résultats des simulations avec convection paramétrée sont comparés avec ceux des simulations avec convection résolue ainsi qu'avec les ensembles de données de référence. La sen-

sibilité de la simulation avec convection résolue au schéma de turbulence et à la paramétrisation de la fraction nuageuse d'échelle sous-maille est examinée pour l'épisode du 23 au 30 novembre 2011.

Les intrusions d'air sec pendant la propagation de la MJO est étudié dans le chapitre 4. La méthode isentropique qui est utilisée pour cette étude est présentée. Ses principes sont discutés et il est montré comment les circulations atmosphériques des masses d'air peuvent être décrites par les diagrammes isentropiques. Les résultats sont présentés dans l'article *The three atmospheric circulations over the Indian Ocean and the Maritime Continent and their modulation by the passage of the MJO* en révision dans *Journal of the Atmospheric Sciences*.

Enfin, les conclusions sont données et des perspectives de travail futur sont proposées.

Chapter 1

The Madden–Julian oscillation

Contents

1.1 Overview of the MJO	14
1.1.1 Definition	14
1.1.2 Identification	20
1.2 Processes governing the evolution of the MJO	24
1.3 Observations and simulations of the MJO	27
1.3.1 Field programs dedicated to the MJO	27
1.3.2 Representation of the MJO in the numerical models . . .	32

1.1 Overview of the MJO

1.1.1 Definition

The MJO, Madden–Julian Oscillation, became known to the scientific community from the work of Madden and Julian in 1970s (Madden and Julian, 1971, 1972), though as noted by Li et al. (2018), it was documented in an earlier study of (Xie et al., 1963) in a Chinese journal. The MJO is an eastward-moving large-scale phenomenon (zonal extent around 12000–20000 km) and the dominant component of the intraseasonal variability in the tropical atmosphere. It is represented by coupled patterns in atmospheric circulation and convection and accompanied by a coherent signal in many other variables (Zhang, 2005). Thus, the MJO propagation can be traced in precipitation, zonal wind, Outgoing Longwave Radiation (OLR), humidity, water vapor etc.

The MJO consists of a zone of strong precipitation and deep convection, i.e. **active phase**, which is flanked to the east and to the west by zones of weak precipitation and convection, i.e. **suppressed phases**. The schematic structure of the MJO is depicted in Fig. 1.1 where the cloud symbol shows the convective center and the arrows show the direction of zonal wind anomalies. West of the convective center, low-level westerlies and upper-level easterlies are present while to the east of the convective center, low-level easterlies and upper-level westerlies are present, thus giving a convergence of the zonal wind close to the surface and a divergence in the upper troposphere.

The position of the convective center relative to the low-level wind

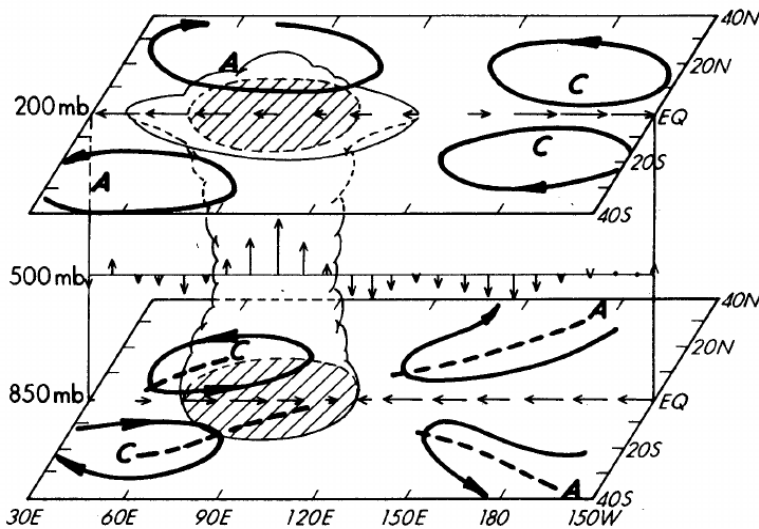


Figure 1.1: Schematic representation of the MJO structure. The cloud symbol shows the convective center. The shaded zones indicate the negative OLR anomalies. The horizontal arrows represent zonal wind anomalies at 850 and 200 hPa and the vertical arrows represent the vertical velocity anomalies at 500 hPa. Letters “A” and “C” indicate the anticyclonic and cyclonic circulation centers, respectively. Reproduced from Rui and Wang (1990).

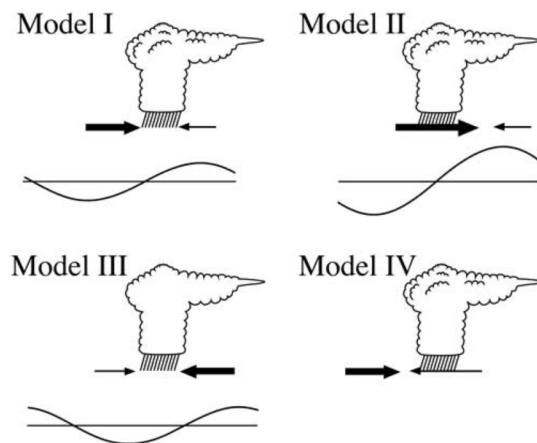


Figure 1.2: Schematic representation of the MJO structure showing the position of the convective center relative to the low-level wind convergence/upper-level wind divergence structure. Arrows width denotes their amplitudes. Curves at the bottom represent intraseasonal perturbations in sea surface temperature induced by the MJO, positive anomalies are located above the horizontal lines. Reproduced from Zhang (2005).

convergence/upper-level wind divergence structure is not constant. Four different configurations are shown in Fig. 1.2. During the MJO propagation over the

Indian Ocean, the convective center is generally located between the low-level westerlies to the west and easterlies to the east, shown as Model I in Fig. 1.2. Over the Pacific Ocean, the convective center is generally located to the west of the low-level wind convergence, shown as Model II in Fig. 1.2. Model III in Fig. 1.2 is theoretically predicted and Model IV is obtained in some numerical simulations, but neither of these configurations was observed (Zhang, 2005).

The MJO propagates eastward around the globe (Fig. 1.3), however, its speed and amplitude vary during its propagation as well as among different MJO events. The convective activity is generally the strongest over the Indian and western Pacific Oceans where the sea surface temperature (SST) is the highest, with an average speed of the MJO being 5–10 m s⁻¹, while over the eastern Pacific convection is much weaker and the MJO is mostly marked by the wind anomalies and larger speed of 10–15 m s⁻¹. The Indo–Pacific Maritime Continent is known for its “barrier effect” on the MJO, as the MJO often weakens or completely disappears during its passage over this region (e.g. Rui and Wang, 1990; Zhang and Ling, 2017). Nevertheless, in some cases the MJO initiates outside the Indian Ocean (Matthews, 2008; Bellenger and Duvel, 2012).

The MJO is a multi-scale phenomenon. Its active phase consists of a number of small-scale convective systems moving in different directions, e.g. Nakazawa (1988) notes the successive formation of convective cloud clusters inside the MJO (Fig. 1.4). In particular, while the MJO moves eastward as a whole, inside its active phase it is possible to see small-scale cloud clusters moving westward.

The satellite images of MJO signature in the water vapor channel in the equatorial band over the Indian Ocean are shown in Fig. 1.5 for 0000 UTC and 1200 UTC 23 November 2011, and 0000 UTC and 1200 UTC 24 November 2011. The development of the MJO and the eastward propagation of the large-scale envelope can be easily observed. The active MJO phase can be seen

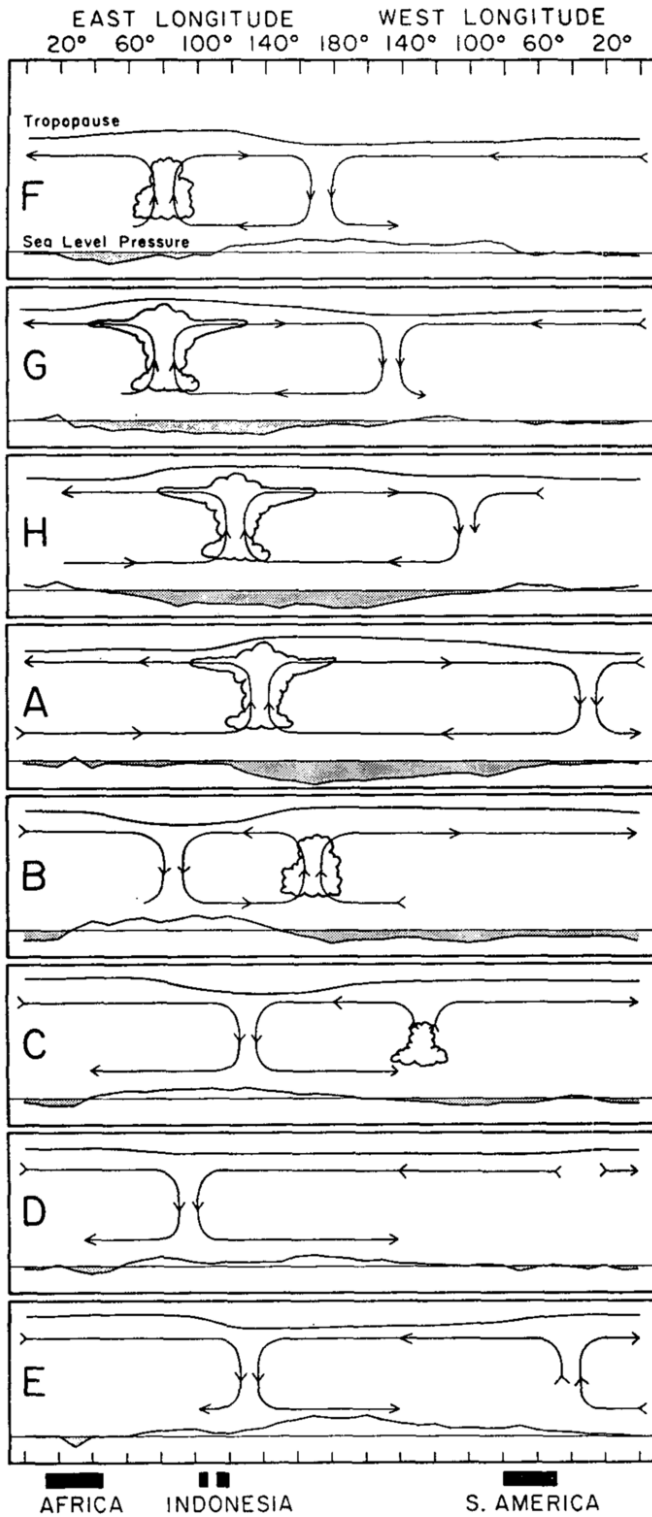


Figure 1.3: Schematic diagram showing the propagation of the MJO. The cloud symbol represents the convective center of the MJO. The line at the top indicates the tropopause height. In the bottom of the charts, the mean pressure disturbance is shown, negative anomalies being shaded. The arrows show the associated zonal circulation. Time increases from top to bottom, from "F" to "H" and then from "A" to "E". This diagram was constructed by Madden and Julian (1972) based on their observations at Canton Island (3°S, 172°W), "A" corresponds to the moment when the minimum pressure wave was observed. Reproduced from Madden and Julian (1972).

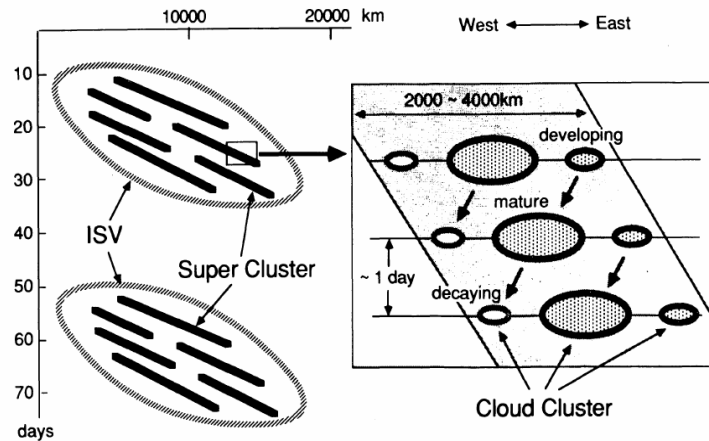


Figure 1.4: Schematic diagram showing the formation of cloud clusters inside the MJO. To the left, the existence of multiple eastward-moving super clusters during the active MJO phase is shown. To the right, the super cluster structure is represented. Reproduced from Nakazawa (1988).

as the large area of high water vapor content and deep convective clouds (white colour) while the suppressed MJO phase corresponds to a dry zone following the active phase.

The intraseasonal period of the MJO is 30–90 days (Madden and Julian, 1972; Zhang, 2005) though the MJO is not a regular periodic oscillation, its strength and period vary from one event to another. Due to the non-regular character of the MJO, Matthews (2008) stated that it is better to use the term “MJ event” rather than “MJO”, describing the MJO as a series of discrete events rather than an oscillation. The irregularity of the MJO is also seen in the atmospheric conditions between two consecutive events: an MJO event can develop after a quiet period (**primary MJ events**, according to Matthews (2008)) as well as redevelop from a previous cycle (**successive MJ events** in Matthews (2008)). Thus, the search of the MJO precursors in the atmosphere and the description of the initiation of the MJO are not well defined problems.

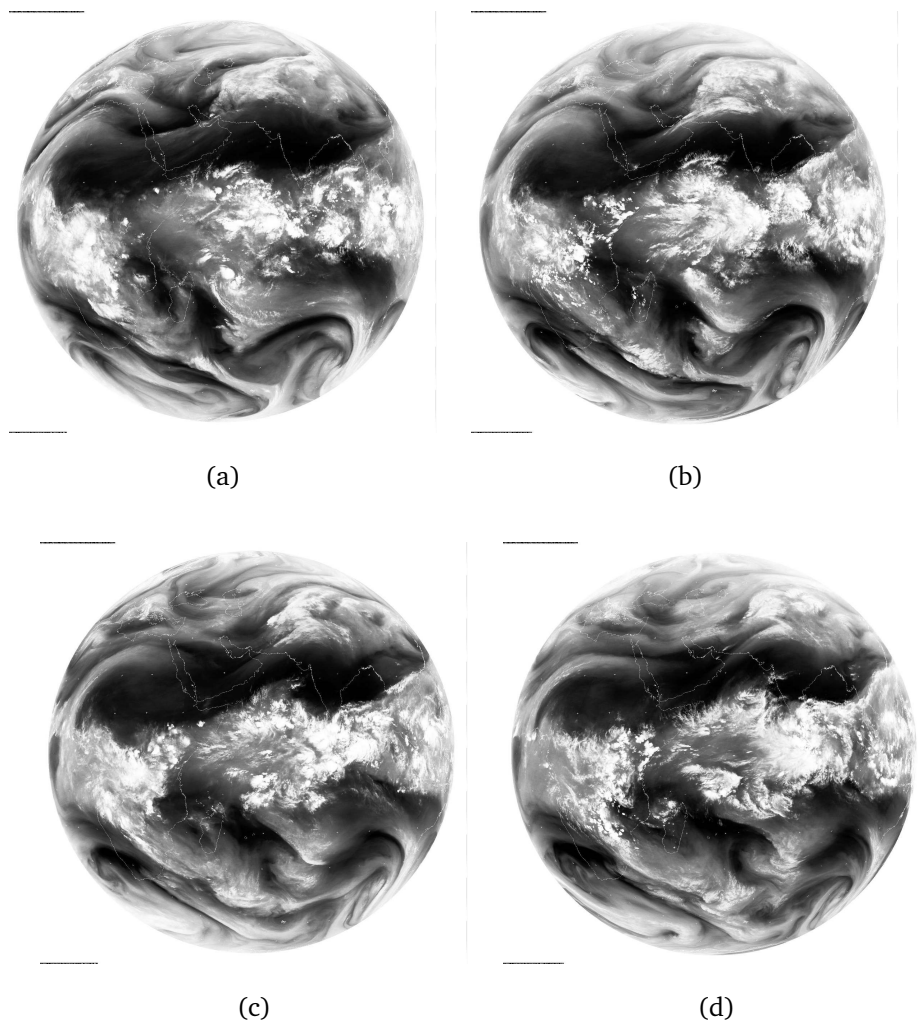


Figure 1.5: Meteosat satellite images showing the propagation of an MJO episode in 2011 as seen in water vapor over the Indian Ocean: (a) 0000 UTC 23 November, (b) 1200 UTC 23 November, (c) 0000 UTC 24 November, (d) 1200 UTC 24 November. Approximate wavelength range 5.7–7.1 μm , Mid-IR / Water vapor. The white colour shows the high content of water vapor and deep convective clouds and corresponds to the active MJO phase. Behind the areas with large water vapor content, areas with low water vapor content are seen, which shows the suppressed MJO phase located behind the active phase. The images are reproduced from the Web site of the NERC Satellite Receiving Station, Dundee University, Scotland: <http://www.sat.dundee.ac.uk/>.

1.1.2 Identification

The propagation of the MJO signal in the atmosphere can be described by choosing a method that shows (i) the presence of the MJO event, as indicated by a defined threshold, and (ii) the location of the active MJO phase in the tropical band.

Straub (2013) categorizes these methods in three groups based on:

- **cloudiness**: typically Outgoing Longwave Radiation (OLR), precipitation (e.g. Rui and Wang, 1990; Hendon and Salby, 1994; Hendon et al., 1999; Matthews and Kiladis, 1999; Kemball-Cook and Weare, 2001; Myers and Waliser, 2003; Benedict and Randall, 2007; Ling et al., 2014; Kerns and Chen, 2016);
- **atmospheric dynamics (circulation)**: zonal wind velocity, velocity potential (e.g. Krishnamurti and Subrahmanyam, 1982; Lorenc, 1984; Knutson et al., 1986; Knutson and Weickmann, 1987; Poehl and Matthews, 2007; Chen and Del Genio, 2009; Tromeur and Rossow, 2010);
- **combined cloudiness and circulation** (e.g. Weare, 2003; Wheeler and Hendon, 2004).

Methods using the principal component analysis. A classical method is based on the principal component (PC) analysis. It shows that it is possible to isolate the signal of the MJO in minimally filtered daily data by projection onto spatial patterns characteristic of the MJO. In this method, the empirical orthogonal functions (EOFs) are calculated based on daily data (e.g. wind, OLR, ...) available for a long enough time period, i.e. over several decades. The data are usually averaged over the range of latitudes corresponding to the equatorial band and filtered to remove the large-scale (seasonal, interannual and decadal)

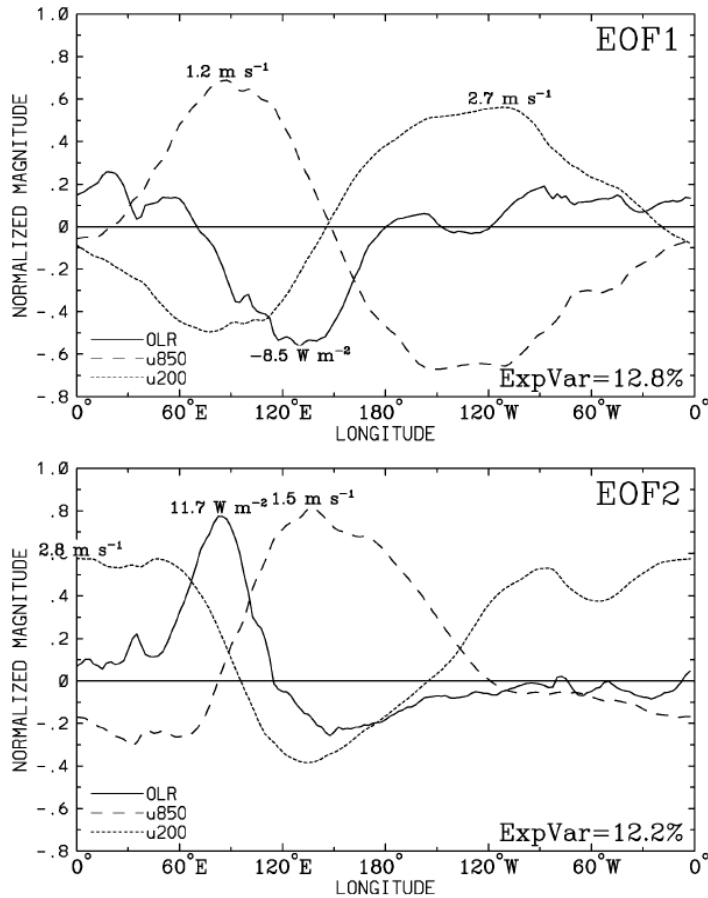


Figure 1.6: Spatial structures of EOF1 and EOF2 of the combined analysis applied to OLR, zonal wind speed at 850 hPa, and zonal wind speed at 200 hPa (each field is normalized by its global (all longitudes) variance before the EOF analysis). —, OLR; --, zonal wind speed at 850 hPa; - - -, zonal wind speed at 200 hPa. Reproduced from Wheeler and Hendon (2004).

variability. Generally, two first EOFs are sufficient to represent the MJO signal. Then, a phase diagram is constructed where the axes are the corresponding PCs: PC1 and PC2. A typical MJO event is thus represented as a loop in the phase space. A so-called “index” is obtained where each point denotes the amplitude of PC1 and PC2 at a given time, and a specific direction of rotation corresponds to the eastward MJO propagation. The resulting diagram is divided into parts corresponding to different regions of the tropical band: (i) Indian Ocean, (ii) Maritime Continent, (iii) Western Pacific, (iv) Western Hemisphere and Africa.

Thus, the location of a point on this curve traces the location of the MJO active phase in the tropical band. The distance between the origin ($PC1=0$, $PC2=0$) and a point of the curve shows the amplitude of an MJO event. Usually, a circle with a radius equal to a particular critical value is chosen to distinguish between the non-MJO periods and the MJO activity periods. This representation of the MJO is used in a large number of studies (e.g. Lorenc, 1984; Knutson and Weickmann, 1987; Lo and Hendon, 2000; Matthews, 2008).

One MJO index well known in the literature, is the **RMM index** described in the work of Wheeler and Hendon (2004), where RMM stands for “Real-Time Multivariate MJO series”. The EOFs are calculated for combined OLR and zonal wind speed at 850 hPa and 200 hPa (Fig. 1.6). Each field is normalized by its global (all longitudes) variance before the EOF analysis. Multiplication of each normalized field and the global variance gives the corresponding anomaly that occurs for 1 standard deviation perturbation of the PC, as given for the corresponding absolute maxima of this field. Physically, EOF1 corresponds to the enhanced convection (negative OLR anomalies) at the Maritime Continent, low-level westerly wind anomalies over the Indian Ocean and Maritime Continent, and low-level easterly wind anomalies over the Pacific Ocean, while upper-level wind anomalies are in the opposite direction to those of the low-level. EOF2 corresponds to the enhanced convection over the Pacific Ocean and wind structure in close quadrature to that of EOF1.

The RMM1 and RMM2 (Fig. 1.7) correspond to the normalized PC1 and PC2. The variations representing the MJO are visible, with noise existing during the absence of the MJO. The RMM2 is lagging RMM1 by 10–15 days.

The RMM index (Fig. 1.8) is constructed in a diagram with the axes (RMM1, RMM2). Thus, the RMM index is a combined cloudiness- and circulation-based according to the classification above. For this index, the am-

plitude is considered as strong (thus showing the period of MJO activity) if it is greater than 1, which is one standard-deviation anomaly in the RMM index. There are also other indices which are either cloudiness-based (Matthews, 2008; Kiladis et al., 2014) or circulation-based (Ventrice et al., 2013).

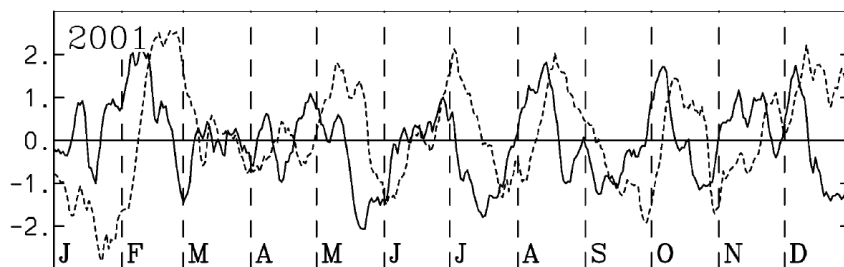


Figure 1.7: The RMM1 and RMM2 time series for 2001. Adapted from Wheeler and Hendon (2004).

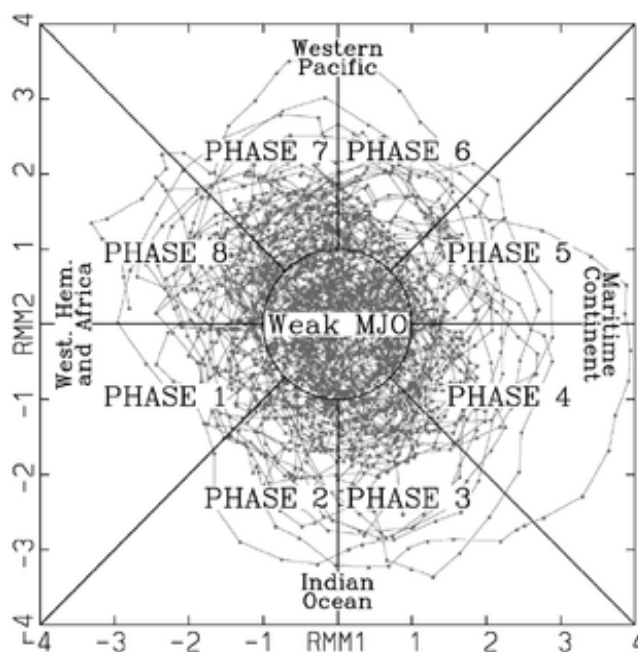


Figure 1.8: (RMM1, RMM2) diagram for the periods of December–January–February in 1974–2003. “Phases” from 1 to 8 are defined as in Wheeler and Hendon (2004) for the easier identification of the MJO location in the tropical band. Phases 2 and 3 correspond to the Indian Ocean, phases 4 and 5 — to the Maritime Continent, phases 6 and 7 — to the Western Pacific, and phases 8 and 1 — to the Western Hemisphere and Africa. Reproduced from Wheeler and Hendon (2004).

1.2 Processes governing the evolution of the MJO

There exist different hypotheses that try to describe the MJO properties such as its period, propagation speed, or multi-scale structure (e.g. the reviews of Zhang (2005); Wang (2005)). Nevertheless, the mechanisms governing the propagation of the MJO are still a matter of discussion among different studies. It must be also outlined that the MJO is not a solution of the classical Matsuno (1966) analysis which identifies distinct propagating modes as westward mixed-Rossby-gravity and equatorial Rossby waves, and eastward Kelvin waves.

One way to explain the existence of the MJO is to consider it as a response of the atmosphere to an independent forcing mechanism. Such mechanisms can be stationary or moving heating source in the tropics (Hu and Randall, 1994, 1995; Salby and Garcia, 1987; Yu and Neelin, 1994) or extratropical perturbations (Hsu et al., 1990; Lau et al., 1994; Matthews et al., 1996; Lin et al., 2000).

Another way is to describe the MJO as an instability arising from the interaction between large-scale dynamics and the convective heating. The major hypotheses to explain this instability consider the interaction of convective heating and large-scale wave motion (wave-CISK, Conditional Instability of the Second Kind) (Lau and Peng, 1987); the “evaporation-wind feedback” (EWF) (Neelin et al., 1987) or “wind-ensued surface heat exchange” (WISHE) (Emanuel, 1987; Yano and Emanuel, 1991); or the friction-induced moisture-convergence interaction (Wang, 1988).

Other important processes are the role of water vapor accumulation (Bladé and Hartmann, 1993), the convective-radiation feedback (Hu and Randall, 1994, 1995), the influence of the seasonal mean circulation and moist static energy distribution (Wang and Xie, 1997) or the thermodynamic feedback between at-

mosphere and ocean (Flatau et al., 1997; Wang and Xie, 1998; Waliser et al., 1999).

It was found in the observations (Myers and Waliser, 2003; Johnson and Ciesielski, 2013; Xu and Rutledge, 2014) that the free-tropospheric moisture profile is influenced by the MJO passage, thus modifying the large-scale organized convection. Several MJO models were constructed based on the coupling of the convection and the moisture, suggesting that the MJO can be explained as a moisture mode instability (Raymond and Fuchs, 2009; Sobel and Maloney, 2013; Adames and Kim, 2016).

The difficulty to explain the MJO properties arises from the fact that all the processes mentioned above contribute to it. Different theories can be interrelated and it is too complicated to analyze a particular process without making several approximations and thus probably neglecting other processes.

The interaction between the large-scale dynamics and convection is more and more often considered to be essential for the MJO. Before the active MJO phase, the free troposphere is humidified, which is also associated with the development of clouds and facilitates convection. Deep convection heats the troposphere and leads to a large-scale dynamic response, which creates the westerly (easterly) wind anomalies to the west (east) of the convective center in the lower troposphere. The westerly wind over the Indian Ocean intensifies and increases the ocean–atmosphere fluxes, which influences the development of deep convection by providing humid air into the lower layers of the troposphere. Hence, the large-scale circulation favours rising motion and contributes to the further development of convection.

The explanation of the MJO period and the eastward propagation is also complicated (Zhang, 2005; Risi and Duvel, 2014). A hypothesis to explain the period of the MJO is the mechanism of moisture recharge-discharge. During the

suppressed MJO phase, the atmosphere is dry. The oceanic mixing layer, the sea surface, and the atmospheric boundary layer are gradually warming up due to the effect of strong solar radiation and weak turbulent fluxes of evaporation (latent heat) and energy (sensible heat) in weak wind conditions. The energy and moisture of the atmospheric boundary layer increase, then convective clouds start to develop and to humidify the low troposphere. After the developing of cumulus congestus clouds (up to around 5 km), the moisture is transported upwards and thus humidify the middle troposphere. This humidification seems to be essential for triggering deep convection. In fact, convective plumes can be weakened by the entrainment of cooler and drier surrounding air. In the presence of strong humidity, convective plumes will be more developed and reach higher altitudes (up to 15 km) giving more precipitation. The evaporation of the precipitation would then be weaker, which limits the cooling of the lower layers and thus, the stabilization of the atmosphere. The typical MJO period of 30–60 days could therefore be representative of the time needed to humidify the whole troposphere and to create favourable conditions for very deep convection. The accumulated convective energy will then be dissipated by the deep convective clouds associated with the active phase of the MJO. In this recharge-discharge mechanism, the initiation of the active phase can be determined by different factors, like perturbations from mid-latitudes or the MJO propagation itself, e.g. the return of the MJO signal to the western Indian Ocean after it has completed a tour of the Earth could initiate a new MJO event and thus influence its periodicity (Matthews, 2008).

The eastward propagation is a characteristic of Kelvin equatorial waves, thus these waves were naturally considered as an explanation for the MJO propagation. Equatorial wave theory, however, does not provide a simple explanation of the observed frequency and velocity of the MJO. The speed of Kelvin waves is

about three times faster than the speed of the MJO. Attempts have been made to explain this difference (e.g. Lau and Peng, 1987; Wang, 1988), but the results have not shown a correct MJO-like phenomenon. Some processes for the explanation of the eastward speed of the MJO are related to thermodynamics e.g. the cooling of the surface to the west of the convective center, while the eastern regions are kept convectively unstable. Other processes are related to the dynamic characteristics such as the meridional circulations that develop on both sides of the equator west of the convective region and contribute to the stabilization of the atmosphere by carrying dry air from the mid-latitudes.

The fundamental processes relevant to the MJO are shown in Fig. 1.9. The marble shading represents the convective relationships with dynamics that are considered to be essential for the understanding of the MJO: the interactions of convective heating, low-frequency equatorial waves (Rossby and Kelvin), boundary layer processes, and moisture distribution. Also, other processes are shown: impact of seasonal mean flows, air–ocean interaction and cloud–radiation feedback. The background circulations could explain the seasonal behaviour of the MJO.

1.3 Observations and simulations of the MJO

1.3.1 Field programs dedicated to the MJO

Due to the importance of the MJO in weather and climate, several campaigns and projects had been carried out to gather in-situ observations. This is essential to be able to test the hypotheses on the MJO-related processes, validate the numerical models, and further improve them.

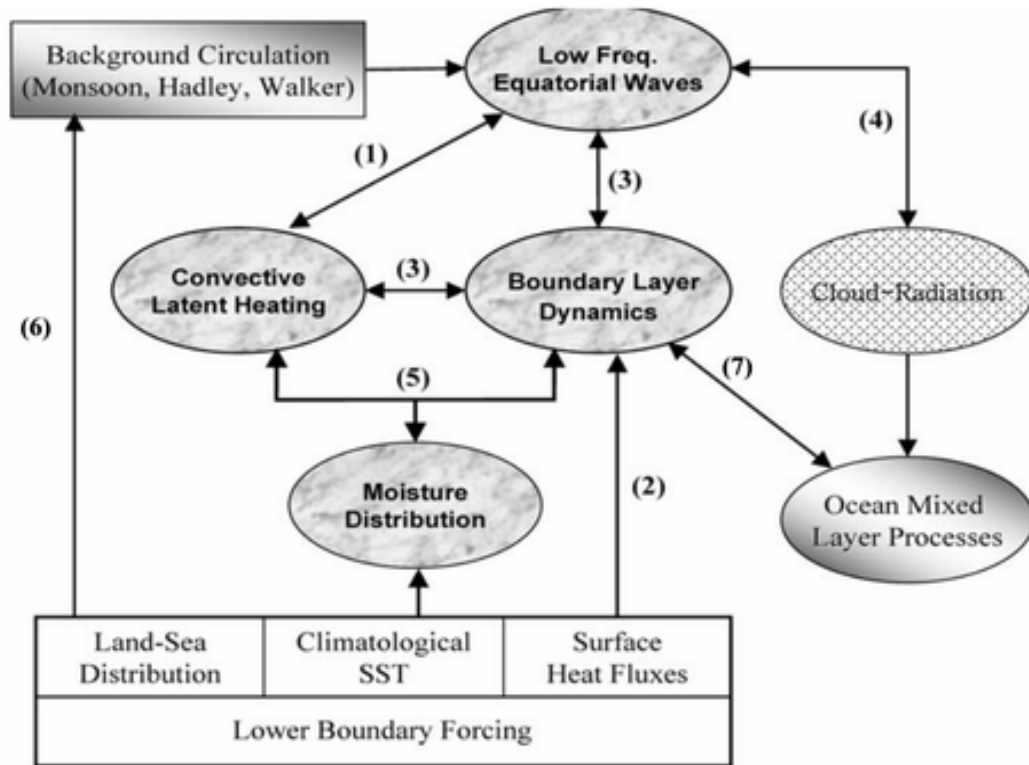


Figure 1.9: Fundamental processes relevant to the MJO. Reproduced from Wang (2005).

TOGA COARE campaign. Tropical Ocean and Global Atmosphere Coupled Ocean–Atmosphere Response Experiment (TOGA COARE) was held during November 1992 – February 1993 to observe the properties of the MJO in the western Pacific warm pool (Fig. 1.10). Such processes were observed as the ocean-atmosphere interaction, westerly wind bursts, precipitation, surface fluxes, equatorial waves (Godfrey et al., 1998). The objectives were to study the organization of the convection, the ocean–atmosphere coupling processes, the oceanic response to combined buoyancy and wind-stress forcing, and the scale interactions contributing to the influence of the western Pacific warm-pool system to other regions and vice versa (Webster and Lukas, 1992). Three MJO episodes occurred during this campaign as seen in the westerly wind bursts,

preceded by the heavy precipitation 1–3 weeks earlier. The maximum westerlies were generally located between two synoptic-scale cyclonic gyres, often not symmetric with respect to the equator in the low-level wind field. In four cases, tropical cyclones developed from the gyres. Important MJO characteristics were observed such as the strong low-level convergence and upper-level divergence as well as the multi-scale structure with the signals in atmospheric variables and SST organized on lengthscales 10–10000 km and timescales from hours to weeks (Webster and Lukas, 1992; Chen et al., 1996).

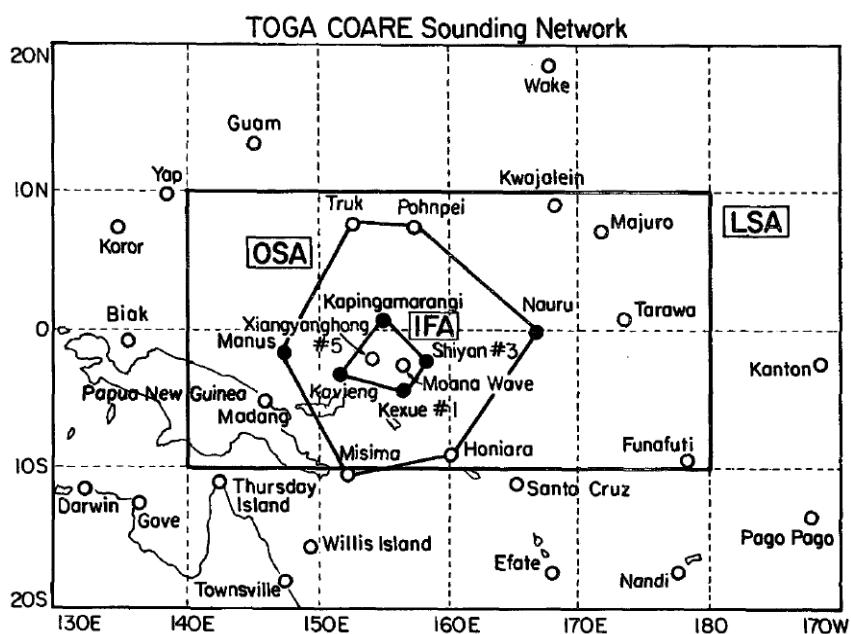


Figure 1.10: TOGA COARE sounding network, consisting of nested arrays: large-scale array (LSA), outer sounding array (OSA), intensive flux array (IFA). Integrated sounding systems (ISS) are indicated by the solid circles, other sounding stations, by the open circles. Reproduced from Lin and Johnson (1996).

MISMO campaign. The Mirai Indian Ocean Cruise for the Study of the MJO Onset (MISMO) was dedicated to the study of the MJO convection onset mechanism in the equatorial Indian Ocean and conducted in October–December 2006 by the Japan Agency for Marine–Earth Science and Technology (JAMSTEC). The

observations were made with the research vessel (R/V) *Mirai*, moored buoys, and several land-based sites at the Maldives (Fig. 1.11).

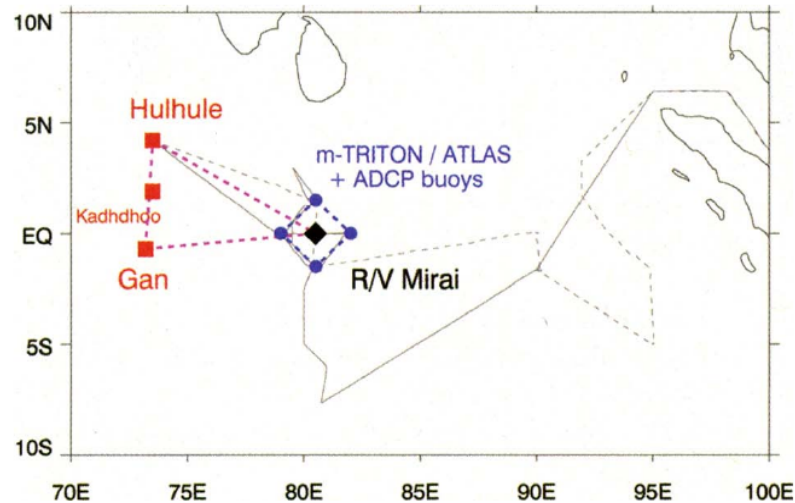


Figure 1.11: Observation network of MISMO campaign. Atmospheric sounding array is shown in red, dashed. Oceanic buoy array is shown in blue, dashed. Stationary observation site (0° , 80.5°E) of the R/V *Mirai* is represented by the solid diamond. Cruise tracks of the R/V *Mirai* (leg 1 and leg 2) are shown in black solid and dashed lines. Reproduced from Yoneyama et al. (2008).

This campaign focused on the air-sea interaction, variations of the ocean surface, evolution of the low-tropospheric moisture convergence and vertical profiles of cloud-related atmospheric parameters and of the wind (Yoneyama et al., 2008). Among other results, the evolution of the convective activity was observed: suppressed in late October – early November, developing in mid-November, and strong activity over the Indian Ocean in late November preceded by gradual deepening of the convection in the divergence field. The preconditioning of the development of the active MJO phase is suggested to be related to the easterly propagating cloud systems which contributed to the deepening of the moist layer and are being driven, in particular, by shallow convection (Katsumata et al., 2009). Also, the appearance of large-scale cloud systems was accompanied by the abrupt change in the upper-tropospheric zonal wind from

westerlies to easterlies, which was probably related to equatorial Rossby waves.

CINDY/DYNAMO/AMIE campaign. The most extensive international field campaign dedicated to the MJO, Cooperative Indian Ocean Experiment on Intraseasonal Variability (CINDY)/ Dynamics of the Madden–Julian Oscillation (DYNAMO)/ Atmospheric Radiation Measurement Program (ARM) MJO Investigation Experiment (AMIE) (Yoneyama et al., 2013; Zhang et al., 2013; Zhang and Yoneyama, 2017), took place in 2011–2012.

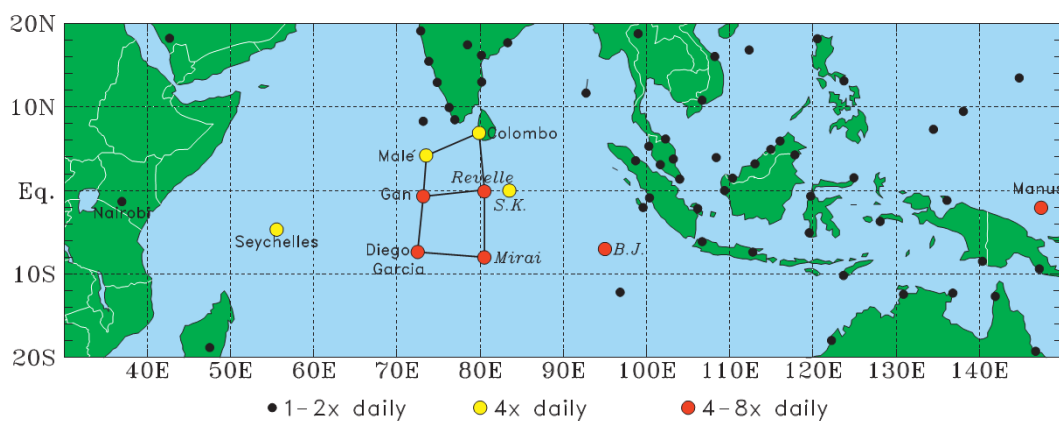


Figure 1.12: DYNAMO/CINDY/AMIE sounding network. The high-frequency soundings (yellow and red dots) and priority sounding sites (black dots) are shown, as well as the research vessels Sagar Kanya (S. K.) and Baruna Jaya (B. J.), which were active for brief periods (25 Sep–19 October for S. K. and 5–18 December for B. J.). Reproduced from Johnson and Ciesielski (2013).

It was focused on tropical intraseasonal variability and in particular, on the MJO life cycle. The CINDY/DYNAMO/AMIE campaign consisted of a sounding-radar array that was formed by a number of research vessels as well as island sites, aircrafts, and enhanced moorings inside and near the array (Fig. 1.12). Its objective was to gather in-situ atmospheric as well as oceanic data over the equatorial Indian Ocean, e.g. related to the structure of cloud and precipitation, moistening, heating, surface fluxes, mixing, and turbulence (https://www.eol.ucar.edu/field_projects/dynamo).

In Fig. 1.13 (top), a schematic representation of the vertical structure of two

MJO events that occurred during the October–November 2011, is shown. The signals in the zonal wind, moisture, vertical wind, temperature are distinct. Also, the observational data (middle) show the signals in SST, which is decreasing during the active phase, while Tropical Rainfall Measuring Mission (TRMM) satellite data shows the rainfall increase during the MJO passages. The active MJO phase is thus forming after the gradual moistening of the low and middle troposphere (Johnson and Ciesielski, 2013). The relative humidity and wind structure allow for the developing of cumulus, congestus, and finally, deep convection. In the upper troposphere and lower stratosphere, tilted warm/cool temperature anomalies and zonal wind anomalies are visible, demonstrating the initiation of gravity or Kelvin waves by the MJO (Kiladis et al., 2001; Virts and Wallace, 2010; Virts et al., 2010).

1.3.2 Representation of the MJO in the numerical models

The numerical simulations and predictions of the MJO remain a big challenge as the models struggle to represent the MJO realistically. Often, the models can not reproduce a coherent propagation of the MJO envelope from the Indian Ocean into the Pacific Ocean. Other typical problems are e.g. too weak amplitude or too short period, incorrect spatial and temporal distributions, incorrect eastward propagation speed.

In global circulation models (GCMs) with the horizontal grid spacing of the order of 100 km, the realistic representation of the MJO depends on the convection parameterization as well as on many other factors such as model physics or mean background state. Among the common difficulties are the reproducing of the propagation of the MJO as shown in multi-model studies (Slingo et al., 1996; Lin et al., 2006; Kim et al., 2011), the interaction between the MJO and

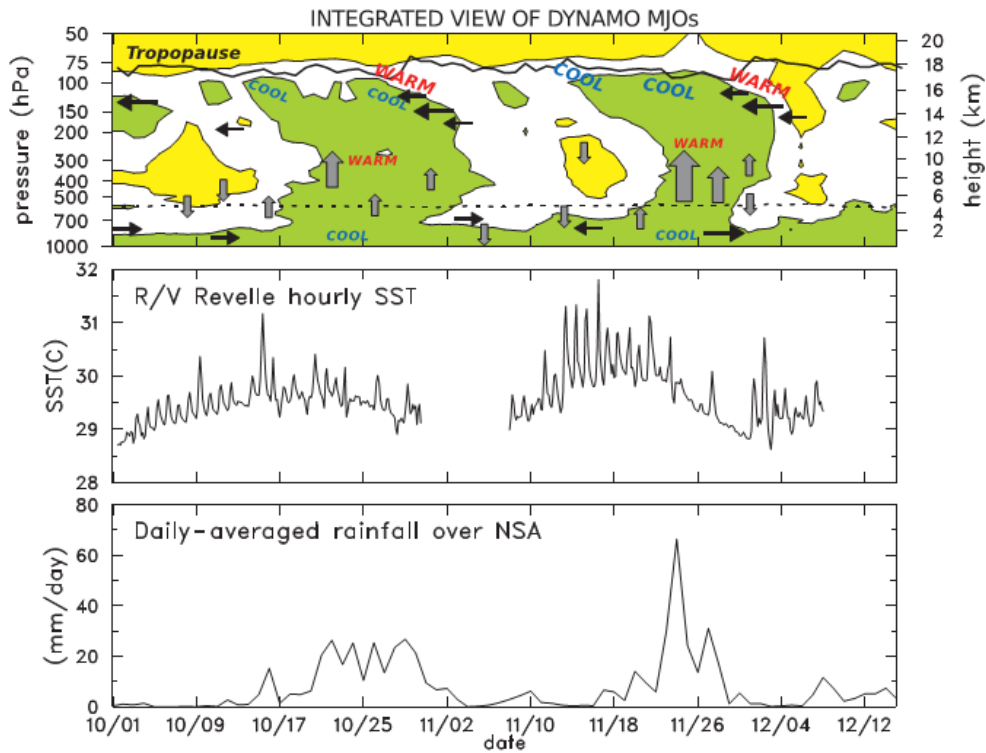


Figure 1.13: Top: Schematic representation of vertical structure of two MJOs during the period 1 October–15 December 2011 (based on average fields measured by the northern sounding array). Green (yellow) color shows areas with the relative humidity greater than 70% (less than 40%), respectively. Thin black arrows indicate the locations of zonal wind maxima. Thick gray arrows represent the locations of the vertical motion maxima. The dashed line shows the daily averaged 0°C level. The solid line denotes the cold-point tropopause level. The indications “cool” and “warm” correspond to the centers of cool and warm temperature anomalies. Middle: Hourly SST at the R/V Revelle. Bottom: The daily-averaged rainfall rate over the northern sounding array, according to TRMM 3B42. Reproduced from Johnson and Ciesielski (2013).

the rainfall diurnal cycle (Peatman et al., 2015), the transition from shallow to deep convection that takes place prior to the development of the active MJO phase (Del Genio et al., 2012).

A possible approach to improve the parameterizations is tuning them e.g. to modify the relationship between the convection and the environmental moisture (Zhang and Mu, 2005; Bechtold et al., 2008) or to include convective momentum transport (Wu et al., 2007; Ling et al., 2009). Also, in regional models with parameterized convection the nudging of a certain field from the global analyses

can be performed e.g. for moisture (Hagos et al., 2011; Subramanian and Zhang, 2014). These approaches can be helpful but their disadvantage is the lack of proper physical justification of the relationship between the MJO convection and the changed field, thus other aspects of the simulations can be degraded.

Including the air-sea coupling might be helpful (Shinoda and Hendon, 1998; Waliser et al., 1999; Maloney and Sobel, 2004; Woolnough et al., 2007) but this interaction is not always necessary for the MJO simulation as some atmospheric models could simulate the MJO without the coupling with the ocean (Hendon, 2000).

Another approach is to use the superparameterizations where instead of the convection parameterization, 2D cloud-system-resolving models are used in each grid cell of the global model and they interact through the large-scale dynamics. Mesoscale convection is explicit in these models and the parameterization is done not for cumulus but for the cloud microphysics. Such models allow to better simulate the MJO or MJO-like systems (Liu et al., 2009; Benedict and Randall, 2009; Grabowski, 2003; Khairoutdinov et al., 2005). Nevertheless, these simulations are computationally expensive and another drawback is that the 3D structure of convection can be important for the MJO simulations.

There have been attempts to simulate the MJO with single-column models, where the forcing data can be taken from observations (Abdel-Lathif et al., 2018), GSM simulations (Woolnough et al., 2010), or even high-resolution convection-permitting simulations (Christensen et al., 2018). However, the challenge here is to derive the required forcing data, and the final analysis might be impacted by different factors such as the missing data, insufficient temporal resolution, etc.

Finally, the models with the resolved subgrid scale processes are very promising. The increase of the resolution allows these models to reproduce mesoscale

features that were not resolved previously by a convective parameterization. This gives a more accurate description of the physics of convective systems in numerical weather prediction (Done et al., 2004). Despite the need of “spinup” time when the high-resolution model progressively develops structure from the analysis with lower resolution, there can be a significant improvement in the reproducing of the precipitation (Lean et al., 2008). Convection-permitting simulations allow also to develop and improve parameterizations in the models with parameterized convection, e.g. by studying the moist thermodynamic processes that determine the time scale and energy of the MJO (Hagos and Leung, 2011). Comparing the simulations performed by the same model but with explicit and parameterized convection can be especially beneficial to see the impact of the explicit treatment of convection (Holloway et al., 2013, 2015). Convection-permitting models with a realistic MJO signal show that the relationship between the moisture and the convection is a key process for MJO initiation and propagation (Holloway et al., 2013, 2015; Takemi, 2015).

In this work, we use the atmospheric non-hydrostatic regional model Méso-NH (Lafore et al., 1998; Lac et al., 2018) which allows us to perform low-resolution simulations with parameterized convection and high-resolution simulations with explicit convection. There have been very few cases of the MJO simulations run with Méso-NH. It was used as a single-column model with the forcing data taken from a GSM for model intercomparison (Woolnough et al., 2010) of three periods during the TOGA–COARE campaign. It has been found that during the transition from the suppressed phase to the active phase, Méso-NH using its available convection parameterization is unable to capture the moistening, drying out and giving lower precipitation rates than most of the other models. In the Ph.D. work of Meeto (2014) dedicated to the study of tropical cyclogenesis in the Southwestern Indian Ocean, the active MJO phase was detected in

the Méso-NH simulations of the cyclone Alenga in November–December 2011. A sequence of nested domains was used with the horizontal resolutions of 32 km, 8 km and several domains with the resolution of 2 km following the cyclone trajectory.

Apart from that, there have been no detailed investigation of the capacity of the Méso-NH model to reproduce the MJO signal and especially using the explicit representation of convection. Thus, one of the objectives of this thesis is to evaluate the capacity of Méso-NH to simulate the MJO and to examine the impact of using explicit convection in a very large domain, which nowadays became possible thanks to the improved performance of parallel computing. Another objective is to study the evolution of the atmosphere during the MJO passage and the processes accompanying the propagation of MJO.

Chapter 2

Model, data and methods

Contents

2.1	The Méso-NH model	38
2.1.1	General description	38
2.1.2	Dynamics	40
2.1.3	Physical parameterizations	40
2.1.4	Preparation of the simulations	45
2.2	Simulations with the Méso-NH model	47
2.2.1	The HiRes simulations	49
2.2.2	The LowRes simulations	50
2.3	Other datasets	51
2.3.1	TRMM precipitation data	51
2.3.2	MJO indices and NCEP/NCAR/NOAA data	53

2.1 The Méso-NH model

2.1.1 General description

The Méso-NH (Lafore et al., 1998; Lac et al., 2018) is an atmospheric non-hydrostatic regional model developed by the Laboratoire d’Aérodynamique et Centre National de Recherches Météorologiques (CNRM) since 1993 (model-related documents can be found on the Web site: <http://mesonh.aero.obs-mip.fr/>). The Méso-NH model makes it possible to perform simulations with a different resolution, from large synoptic scales (order of 100 km and more, e.g. depressions, anticyclones) to convective scales (order of 100 m, e.g. small vortices in the surface boundary layer) to turbulent scales, thus allowing for modeling a large variety of the atmospheric phenomena.

In Méso-NH, the anelastic approach is used which allows to eliminate the acoustic waves from the considered set of equations. In the continuity equation and in the momentum equation the fluid density is approximated by the constant density profile except in the buoyancy term. The anelastic approximation uses the assumption that the atmosphere will stay close to a chosen “reference state”, which is considered here to correspond to the horizontally averaged initial profiles over the simulation domain.

The prognostic variables are the wind velocity components (u , v , w), the potential temperature (θ), the subgrid scale turbulence kinetic energy (TKE), the mixing ratio of water vapor and hydrometeors i.e. solid and liquid precipitating and nonprecipitating water particles (the mixing ratio is the ratio of the mass of considered substance to the mass of dry air within the considered volume). Up to seven different mixing ratios can be chosen depending on the cloud microphysics scheme: vapor (r_v), cloud droplets (r_c), rain water (r_r), cloud ice (r_i), snow (r_s), graupel (r_g), and hail (r_h). The pressure field is calculated us-

ing a diagnostic pressure equation that is based on the motion and continuity equations.

The Méso-NH code consists of three steps: (i) the preparation step of a simulation where the initial fields are chosen; (ii) the temporal integration, starting with the initialization step (Fig. 2.1); (iii) the post-processing step where additional diagnostic fields are computed.

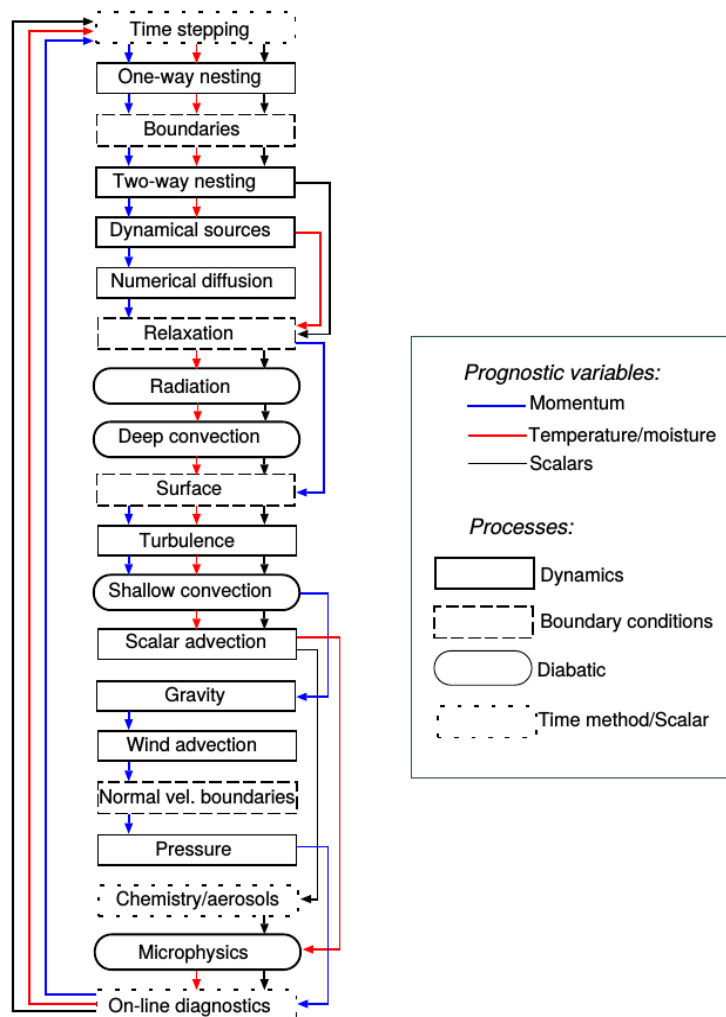


Figure 2.1: Block diagram representing one integration time step in Méso-NH. Reproduced from Lac et al. (2018).

2.1.2 Dynamics

The **advection schemes** in Méso-NH are of two kinds: those for momentum and those for scalar variables. The available advection schemes for momentum are flux-form conservative schemes centered in time. The available advection schemes for scalar variables are positive definite schemes. In this work, for the wind advection a 3-order scheme of WENO (Weighted Essentially Non Oscillatory) type is used, and for the advection of thermodynamic variables, the PPM (Piecewise Parabolic Method) scheme is used.

Méso-NH uses a **C-grid in the Arakawa convention** (Mesinger and Arakawa, 1976), both on the horizontal and on the vertical (Fig. 2.2). The meteorological variables (temperature, water substances, TKE) and the scalar variables are calculated in the center of grid cells (the mass points) while the momentum components are calculated on the faces of grid cells (the flux points). Heat exchanges, water phase transitions, subgrid scale processes or surface interactions are not taken into account in the dynamical core of Méso-NH and need to be parameterized.

2.1.3 Physical parameterizations

The surface schemes are externalized in the SURFEX (Surface Externalisée) model (Masson et al., 2013) (<http://www.cnrm-game-meteo.fr/surfex/>) coupled with Méso-NH. The surface and the atmosphere interact via energy fluxes applied at the base of the atmospheric numerical model. The fluxes provided to the atmospheric model are the momentum flux, turbulent sensible and latent heat fluxes, the upward radiative fluxes, and, as an option, the CO₂ flux.

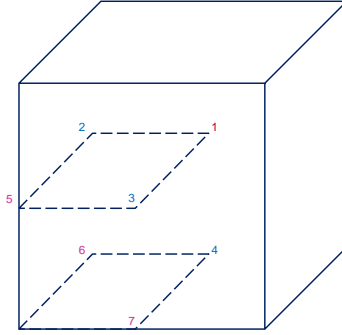


Figure 2.2: C-grid in the Arakawa convention. 1 — mass points, 2 — u points, 3 — v points, 4 — w points, 5 — vertical vorticity point, 6 — vorticity components along y , 7 — vorticity components along z .

The fraction of the grid cell corresponding to each surface type, is calculated, and then for every type the corresponding surface flux describing the surface-atmosphere interactions, can be computed. The main processes of SURFEX are schematically represented in Fig. 2.3.

For the four main surface types — sea, nature, town, and inland water — the following surface schemes are used. For natural soils, Méso-NH uses the Interactions between Soil, Biosphere, and Atmosphere (ISBA) parameterization (Noilhan and Planton, 1989). The input data for the ISBA scheme are the horizontal wind speed, humidity, pressure, temperature of air, precipitation, radiation, and concentrations of dust if necessary. The hydrology is represented by three soil layers where the evolution of water content is calculated by ISBA from the evaporation and precipitation. Over the urban (artificial) areas, the Town Energy Budget (TEB) is used (Masson, 2000). Lake surfaces are described by the freshwater lake model (FLake) (Mironov et al., 2010). Ocean surfaces in SURFEX are characterized by the sea surface temperature (SST) and the ocean surface currents. In Méso-NH, it is possible either to use the fields prescribed from the observations or analyses, or use the coupling with an oceanic model such as de-

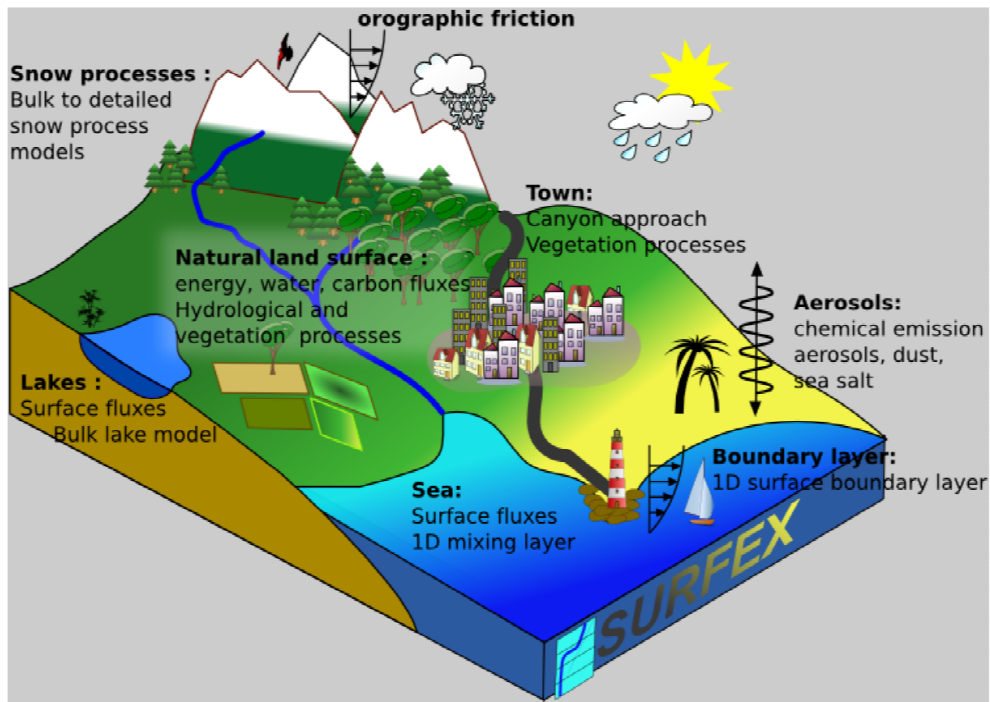


Figure 2.3: The main processes of SURFEX depending on the surface type: sea, nature, town, inland water. Reproduced from Masson et al. (2013).

scribed in Gaspar et al. (1990); Voltaire et al. (2017). For the exchanges over sea surfaces, the surface fluxes are parameterized for a wide range of wind and environmental conditions (Belamari and Pirani, 2007). In this work, the SST is constant in time and is provided by the ECMWF analyses at the initial time.

To parameterize the energy transfers from unresolved to resolved scales, a **turbulence scheme** is used. In Méso-NH, the turbulence is described by the 1.5-order closure scheme of Cuxart et al. (2000), where the TKE is prognostic and the mixing length is diagnostic. This scheme can be set in 1D mode as well as in 3D mode. In the 1D mode, the subgrid scale interactions between the grid cells are supposed to be only vertical while the horizontal fluxes are neglected, thus using the hypothesis of the horizontal homogeneity. This corresponds to the thermal turbulence which is mostly vertical. This method uses the mixing length

of Bougeault and Lacarrère (1989) and is usually activated in the mesoscale simulations. In the 3D mode, the dynamic turbulence is considered leading to the transports in all directions. The subgrid scale parameters in a grid cell thus depend on those in all the neighbour cells. This method uses the 3D mixing length of Deardorff (1980) and is usually activated in the large-eddy simulations (LES). Nevertheless, the use of 3D mode in a mesoscale simulation allows for better representation of the cloud organization and their life time duration as shown in Machado and Chaboureau (2015). In our simulations, we conduct a sensitivity test with the 3D mixing length.

A subgrid scale **shallow convection scheme** is necessary for the dry thermals and shallow cumuli representation within the boundary layer for horizontal resolutions coarser than 500 m–1 km. In this work, EDKF (Eddy-Diffusivity-Kain-Fritsch) scheme with the parameterisation of Pergaud et al. (2009) is used. The turbulent fluxes in the boundary layer are calculated from an eddy-diffusivity term for local mixing and a mass flux term for large eddies or plumes.

A **cloud microphysics scheme** is necessary to describe the processes involving water vapor and hydrometeors (liquid and solid precipitating and non-precipitating water particles): the formation, growth, decay and sedimentation of hydrometeors. Such scheme is important as it allows to calculate the surface precipitation rates as well as to represent the cloud-radiation interactions. The cloud dynamics is affected by the absorption and release of latent heat through the water phase transitions. These diabatic processes are very important in the tropical regions as they have a strong influence at the global scale. In Méso-NH, two assumptions are made in the microphysical schemes. The first one is the categorizing of the hydrometeors using a bulk approach, and there exist up to six types of hydrometeors depending on the chosen scheme: cloud droplets, rain water, cloud ice, graupel, snow and hail. The second assumption is the satura-

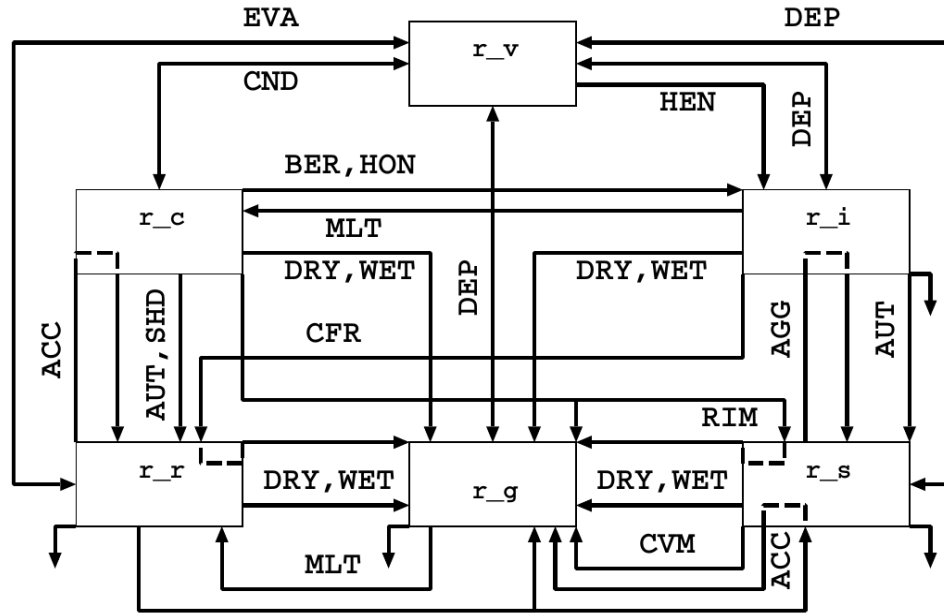


Figure 2.4: Microphysical processes in Méso-NH ICE3 scheme. Conversion processes: EVA — rain evaporation and condensation, DEP — deposition and sublimation, CND — cloud water condensation and evaporation, HEN — heterogeneous nucleation, BER — Bergeron-Findeisen effect, HON — homogeneous nucleation, MLT — melting, DRY — graupel dry growth, WET — graupel wet growth, ACC — accretion, AUT — autoconversion, SHD — liquid water shedding from the surface of the graupels, CFR — rain freezing by contact, AGG — aggregation, RIM — riming, CVM — conversion of snow into graupel by partial melting. Precipitating is shown by the downward arrows. Reproduced from Pinty and Jabouille (1998).

tion adjustment: a thermodynamic equilibrium is imposed, with the condition that after each time step neither supersaturation nor undersaturation is allowed. For the supersaturated air, water vapor should reach saturation, thus condensing or being deposited. For the undersaturated air, some hydrometeors should evaporate or sublimate. In Méso-NH, the cloud microphysics are described with the scheme ICE3 (Pinty and Jabouille, 1998) with six species — vapor, cloud droplets, rain water, cloud ice, snow, and graupel. In this microphysics scheme, more than 30 processes are represented such as nucleation, fusion, accretion (Fig. 2.4). Here it is considered that cloud droplets and cloud ice are not precipitating hydrometeor species while rain water, graupel and snow can precipitate.

The concentrations of these species are parameterized and are calculated from the mixing ratios. The size distributions are obtained from a gamma law, while the mass-size and the velocity-size relationships are taken as simple power laws.

The use of an assumption of the adjustment to saturation after each time step leads to the “all or nothing” method where the grid cell is supposed to be either clear sky or fully cloudy. Another approach of cloud parameterization is to use a statistical **subgrid scale cloud scheme** where the cloud fraction is parameterised as a function of turbulent and convective contributions (Chaboureau and Bechtold, 2005). In most of our simulations, this scheme is used while a sensitivity test with the “all or nothing” method is also conducted.

The **radiative transfer** in the atmosphere is described in simulations by the radiation scheme of the ECMWF operational model coupled with Méso-NH. The net total radiative flux in the model is represented as the sum of upward and downward fluxes: the shortwave radiation from the Sun which is subject to scattering, reflection, and absorption by the atmospheric particles, and the longwave radiation emitted by the Earth’s surface and clouds. The net total radiative heat flux is calculated in each atmospheric column and provides the potential temperature tendency. The schemes used in this work, is the Rapid Radiative Transfer Model (Mlawer et al., 1997) for longwave radiation and the two-stream formulation (Fouquart and Bonnel, 1986) for shortwave radiation.

2.1.4 Preparation of the simulations

The **initial and boundary conditions** need to be defined prior to running a simulation with Méso-NH. There are different possibilities for the lateral boundary conditions. They can be cyclic/rigid wall/open; coupled with the large-scale fields given by the ARPEGE (Action de Recherche Petite Echelle Grande

Echelle) or ECMWF (European Centre for Medium-range Weather Forecasts) models, forecast or analysis data, or with the higher resolution fields obtained from limited domain models like ALADIN (Aire Limitée, Adaptation dynamique, Développement InterNational — ARPEGE version on a domain located in European region) or AROME (Applications of Research to Operations at MEscale); or defined by the interactive grid-nesting. In this work, the ECMWF meteorological analyses are used to prescribe the prognostic model variables at the initial and boundary conditions for the variables existing in ECMWF, otherwise the variables are set as zero. The initialisation of the model is done at (1) 0000 UTC 6 April 2009, (2) 0000 UTC 23 November 2011, and (3) 0000 UTC 9 February 2013, where the ECMWF horizontal resolution is $\Delta x=25$ km for the case of 2009 and $\Delta x=16$ km for the cases of 2011 and 2013. During the simulation, files are coupled with the ECMWF analyses every 6 h, the boundary conditions for other time values are calculated as the linear approximation between two consecutive ECMWF analyses used as coupling files. No large-scale forcing is applied.

Before the start of a simulation, a **physiographic file** is produced containing the surface cover type which is obtained from the global ECOCLIMAP database (Masson et al., 2003). There are 250 available surface cover types which describe not only the landscape, but the whole ecosystem. There exist 15 land cover types e.g. different types of forest, soil, snow, wetlands, urbanized areas, and 16 climate types e.g. different types of tropical, marine, desert climate (sometimes different ecosystems can be aggregated into one representative system), thus giving vegetation parameters for areas all around the world. Orography and land cover are obtained from the GTOPO30 databases (<https://1ta.cr.usgs.gov/GTOPO30>) with the resolution 30 arc second (~ 1 km). As we consider a domain close to the equator, we chose the Mercator projection. For using in the model, the surface data are interpolated over the

grid mesh. A good representation of surface features is important for a realistic reproducing of meteorological phenomena, as they can be often influenced or generated by the topography: precipitation, mesoscale circulations, blocking of synoptic systems. The locations of land and water as well as different types of land cover are necessary to calculate the surface fluxes of moisture, heat and momentum. Four different types of the surface (natural landscape, urban zone, sea and inland water) are deduced from the cover types. During a Méso-NH simulation, a specific surface scheme is used for each of these types. Then, the physiographic data together with information on the vertical grid and with the interpolated ECMWF analyses are used to start a simulation or for the boundary conditions.

In the vertical, we use the **Gal-Chen and Sommerville coordinate** following the surface elevation. In our case, the vertical grid spacing varies from 60 to 600 m. In the all simulations we used 72 vertical levels. The upper boundary is supposed to be a rigid horizontal lid with a free slip condition on the atmosphere. To damp the gravity waves generated by convection, a sponge layer is usually inserted near the upper boundary and the prognostic variables are relaxed towards the large-scale values in this sponge layer. In our case, the model top was set to 30 km with the upper 3 km being a sponge layer. An additional absorbing zone is located close to the lateral boundaries, it allows to damp outward propagating waves or to slowly incorporate inward propagating larger scale waves.

2.2 Simulations with the Méso-NH model

While low-resolution simulations (with the horizontal resolution of 10–100 km) give the possibility to explore the large-scale motions, in such simulations

the processes that are not resolved within grid spacings, need to be parameterized. Thus a question of the quality of these simulations arises (e.g. the review of Prein et al. (2015)). The convection parameterization schemes used in low-resolution simulations have been identified as a main reason of model errors and uncertainties (Ellingson et al., 1991; Henderson-Sellers et al., 1993; Pederesen and Winther, 2005; Déqué et al., 2007). One especially important subgrid scale process in climate models is the deep convection that is a major source of precipitation in many regions, i.e. the tropics. The triggering of deep convection depends on the interaction of processes at scales from the microscale to the synoptic scale, thus making the parameterizing of deep convection very complicated. The convection parameterization schemes can thus introduce errors at different scales, from the diurnal cycle of convective precipitation (Brockhaus et al., 2008) to intraseasonal or interannual variability (Song and Zhang, 2009; Zhang and Song, 2010; Chikira, 2010). High-resolution simulations no longer need convective parameterizations, and moreover, the orography in such simulations is more accurately represented. The added value of the high-resolution simulations exists thus in regions where deep convection is important and in regions with a strongly heterogeneous orography, making the high-resolution simulations useful for studying atmospheric processes that are difficult to observe directly.

Using the Méso-NH model, we can compare the simulations with the different resolutions. To estimate the impact of the explicit-convection modeling i.e. to analyze the effects of the resolution and representation of convection on precipitation, low-resolution simulations were also performed. In total, eight simulations were performed to investigate three different episodes of the MJO passage over the Indian Ocean and the Maritime Continent. All simulations were performed with the Méso-NH version 5-1-3 at the supercomputers Occigen

(<https://www.cines.fr/>) and Nuwa (<http://nuwa.aero.obs-mip.fr/>).

We consider three time periods when the MJO was active over the Indian Ocean and the Maritime Continent: (1) 6–14 April 2009 (9 days), (2) 23–30 November 2011 (8 days), and (3) 9–28 February 2013 (20 days). We concentrate on the Indian Ocean and the Maritime Continent, where the MJO propagation is generally the most visible. We performed simulations for a large domain 26.7°S – 26.7°N , 44.6° – 155.4°E which is shown in Fig. 2.5 (different subdomains of the simulation domain are used for different types of analysis). This domain was chosen to describe the MJO propagation in different regions and compare the MJO properties in active and suppressed phases of the MJO during its passage over the same location. The choice of a large simulation domain was possible thanks to the parallel computing capability of Méso-NH model (Pantillon et al., 2011).

2.2.1 The HiRes simulations

For every time period (2009, 2011, and 2013), a high-resolution simulation is performed where convection is calculated explicitly. In this thesis, these simulations will be referred to as HiRes-2009, HiRes-2011, and HiRes-2013. In all these simulations, the 1D turbulence scheme is used with the mixing length of Bougeault and Lacarrère (1989). For the 2011 period, we have also conducted two different sensitivity tests. In the first one, a HiRes simulation (HiRes-2011a) was performed using “all or nothing” method of cloud parameterization instead of the statistical subgrid scale cloud scheme described in Chapter 2.1.3. In the second sensitivity test, a HiRes simulation (HiRes-2011b) was performed using the 3D turbulence scheme with the mixing length of Deardorff (1980).

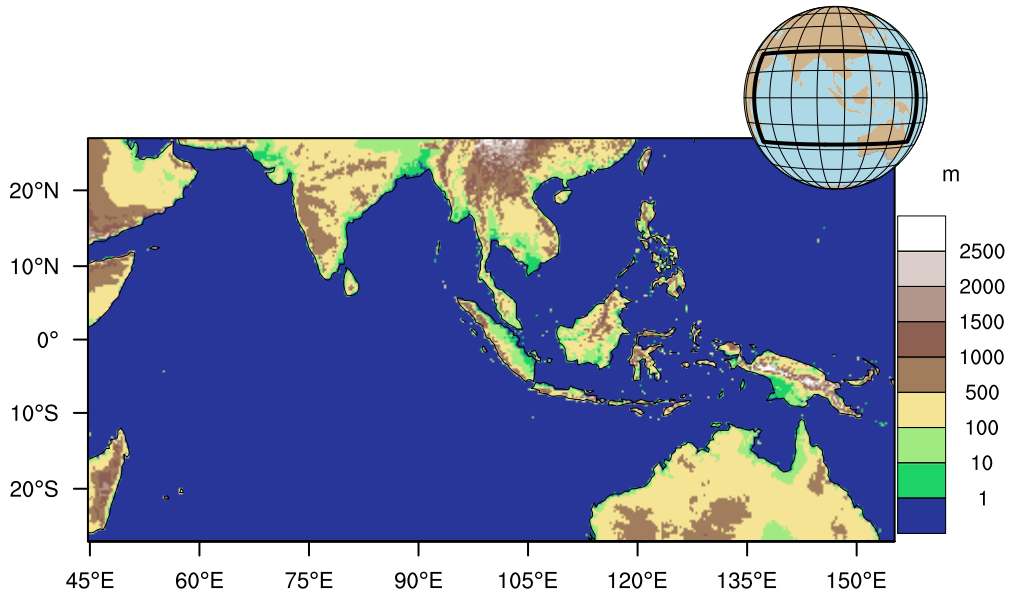


Figure 2.5: Simulation domain (Indian Ocean and Maritime Continent). In color, the elevation (m) is shown.

For a domain of approximately $6000 \times 12300 \times 30 \text{ km}^3$, HiRes simulations need $1538 \times 3074 \times 72$ grid points (~ 340 millions).

2.2.2 The LowRes simulations

For every time period, a low-resolution simulation (LowRes) with the parameterized convection, where the horizontal grid spacing is $\Delta x = 32 \text{ km}$, was also performed. These simulations will be further referred to as LowRes-2009, LowRes-2011, and LowRes-2013. In the low-resolution simulations (generally $> 10 \text{ km}$), the deep convective motions have scales smaller than the horizontal resolution, and thus are subgrid scale and it is necessary to use parameterizations. In Méso-NH, the deep convection is based on the mass flux scheme of

Kain and Fritsch (KAFR) adapted to Méso-NH by Bechtold et al. (2001). For a domain of $\sim 6000 \times 12300 \times 30$ km³ LowRes simulations need $194 \times 386 \times 72$ grid points (~ 5 millions).

2.3 Other datasets

2.3.1 TRMM precipitation data

To evaluate the results of the simulations, the 3B42 precipitation product of the Tropical Rainfall Measuring Mission (TRMM) is used (Simpson et al., 1996; Huffman et al., 2007).

The objective of TRMM (1997–2015, developed jointly by the USA and Japan) was to monitor and measure tropical and subtropical rainfall using microwave and visible infrared sensors, including the first spaceborne rain radar. Its data was analyzed and combined with other various satellite systems as well with land surface precipitation gauge analyses, to obtain the final calibrated product. The postprocessing consisted of two steps: first, an experimental best-effort real-time monitoring product (approximately 9 h after real time) was obtained, and then the further processing was performed to obtain a research-quality product (Huffman et al., 2007). The block diagram of TRMM data postprocessing is shown in Fig. 2.6.

The passive microwave measurements were taken from a variety of low earth orbit (LEO) satellites, including the Microwave Imager (TMI) on TRMM, Advanced Microwave Scanning Radiometer-Earth Observing System (AMSR-E) on Aqua, the Advanced Microwave Sounding Unit-B (AMSU-B) on the National Oceanic and Atmospheric Administration (NOAA) satellite series, and Special

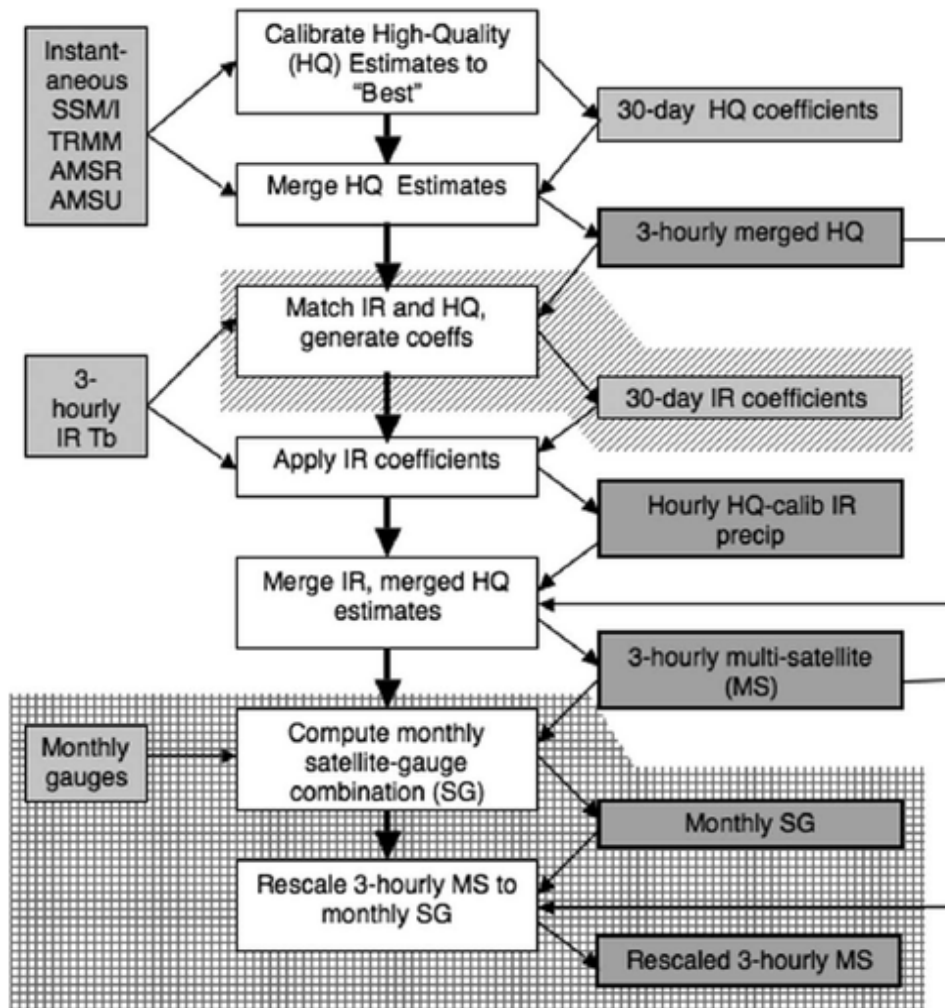


Figure 2.6: Block diagram showing the TRMM data postprocessing. Input data are shown in the left, processing is described in the center, and the output data are on the right. The slanted shading shows the asynchronous calculation for the real time algorithm. The grid shading shows the operations performed only for the research product. Reproduced from Huffman et al. (2007).

Sensor Microwave Imager (SSM/I) on Defense Meteorological Satellite Program (DMSP) satellites.

The 3B42 precipitation product of the Tropical Rainfall Measuring Mission (TRMM) consists of merged high quality / infrared precipitation and root-mean-square (RMS) precipitation-error estimates. This product has 3-hour temporal

resolution and the spatial resolution of $0.25^\circ \times 0.25^\circ$, the data are available in a global belt extending from 50°S to 50°N latitude. The 3B42 estimates are produced in four stages: (i) the microwave precipitation estimates are calibrated and combined; (ii) infrared precipitation estimates are created using the calibrated microwave precipitation; (iii) the microwave and IR estimates are combined; (iv) rescaling to monthly rain gauge data is applied.

The spatiotemporal sampling of the TRMM 3B42 product is convenient for the analysis of the MJO and of the diurnal cycle of precipitation. This explains that the TRMM 3B42 product has been widely employed (e.g. Kerns and Chen, 2016; Reinares Martínez and Chaboureau, 2018).

2.3.2 MJO indices and NCEP/NCAR/NOAA data

MJO indices. Different MJO indices can be used to identify the MJO phase and to determine the location of the MJO on the globe, as explained previously (Chapter 1). In this work, they are used to evaluate the ability of the simulations to reproduce the MJO propagation and to explain the differences between the different MJO episodes. Here, the OLR MJO Index (OMI) (Kiladis et al., 2014), the Velocity Potential MJO index (VPM) (Ventrice et al., 2013), and Real-Time Multivariate MJO series (RMM) (Wheeler and Hendon, 2004) are used. OMI is constructed by the projection of 20–96 day filtered OLR onto the daily spatial EOF patterns of 30–96 day eastward filtered OLR. (For the comparison of OMI and RMM at the same diagram, the sign of OMI PC1 and the PC ordering need to be reversed, as OMI(PC2) is analogous to RMM(PC1) and $-OMI(PC1)$ is analogous to RMM (PC2).) VPM index is calculated similarly to RMM, but in the combined EOF calculation 200-hPa velocity potential is used instead of OLR, together with U200 and U850. OMI

and VPM indices were obtained from the NOAA/ESRL Physical Sciences Division (PSD) Web site: <https://www.esrl.noaa.gov/psd/mjo/mjoindex/> and the RMM index was obtained from the Bureau of Meteorology (Australia) Web site: <http://www.bom.gov.au/climate/mjo/>.

NCEP/NCAR datasets. To obtain the wind climatology fields necessary to calculate the wind anomalies, the datasets of the US National Centers for Environmental Prediction (NCEP)/National Center for Atmospheric Research (NCAR) 40-year Reanalysis Project are used. In the NCEP/NCAR 40-year Reanalysis Project, the atmospheric fields were recovered and later assimilated with a data assimilation system that is kept unchanged over the reanalysis period (Kalnay et al., 1996). Different sources of observation (land stations, aircraft, satellites etc.) were used for developing these datasets, including the data that were not available in real time and were provided later by many countries. In this work, NCEP/NCAR reanalyses for the zonal wind velocity “U, NCEP/NCAR Reanalysis 1” are used (<https://www.esrl.noaa.gov/psd/>). The spatial resolution of the zonal wind velocity is $2.5^{\circ} \times 2.5^{\circ}$ (144x73) (Kalnay et al., 1996) for the global domain $90^{\circ}\text{N}–90^{\circ}\text{S}$, $0.5^{\circ}\text{E}–359.5^{\circ}\text{E}$.

For the data analysis, we use the **NCAR Command Language (NCL)** (Version 6.1.2): Boulder, Colorado: UCAR/NCAR/CISL/VETS, <http://dx.doi.org/10.5065/D6WD3XH5>.

Chapter 3

Assessment of the Méso-NH simulations

Contents

3.1 Overview of the MJO events	57
3.2 Simulations of three MJO events	59
3.2.1 Initial conditions: distribution of surface pressure and SST	60
3.2.2 Distribution of precipitation	61
3.2.3 Eastward propagation of the precipitation signal	72
3.2.4 Coupling of the precipitation and the zonal wind signals	76
3.2.5 Diurnal cycle of precipitation	83
3.2.6 Summary	90
3.3 Sensitivity of the 2011 simulation to the cloud fraction and turbulence parameterizations	91
3.3.1 Impact on the propagation of the precipitation signal	92
3.3.2 Impact on the zonal wind	93

3.3.3	Impact on the water vapor and rain	95
3.3.4	Impact on the relative humidity	97
3.3.5	Summary	100

3.1 Overview of the MJO events

An overview of the three selected MJO events is first given using the RMM index and TRMM 3B42 precipitation data. The MJO events are described over the full equatorial band and during the month when they occurred, that is April 2009, November 2011, and February 2013.

Approximate periods can be defined corresponding to the strong MJO signal in RMM diagrams, showing the propagation through the Indian Ocean and the Maritime Continent. The RMM indices are presented in Figs. 3.1a–c. The diagrams show strong (larger than 1.5) amplitudes over the Indian Ocean and the Maritime Continent during the periods of approximately 6–14 April 2009 (Fig. 3.1a), 23–30 November 2011 (Fig. 3.1b), and 9–28 February 2013 (Fig. 3.1c). In the first case, a strong MJO signal appears in the RMM diagram before 6 April 2009. In the second case, the RMM amplitude is weak (i.e. close to 1) before 22 November 2011 and the signal starts to develop afterwards. These two periods were described in the literature i.e. the April episode was studied by Holloway et al. (2013), and the November episode took place during the CINDY/DYNAMO/AMIE campaign (e.g. Johnson and Ciesielski, 2013). In the case of 9–28 February 2013, the MJO signal is strong though it undergoes a fluctuation around 25 February, crossing the unity circle but still remaining close to it. Before the chosen initial date of 9 February, the RMM curve was located outside of the unity circle except a short fluctuation during the period 7–8 February when it makes two close crossings of the unity circle, changing the MJO state from strong to weak and back very fast.

The corresponding precipitation data as obtained by TRMM is shown in Hovmöller longitude–time diagrams (Figs. 3.1d–f). Precipitation is averaged be-

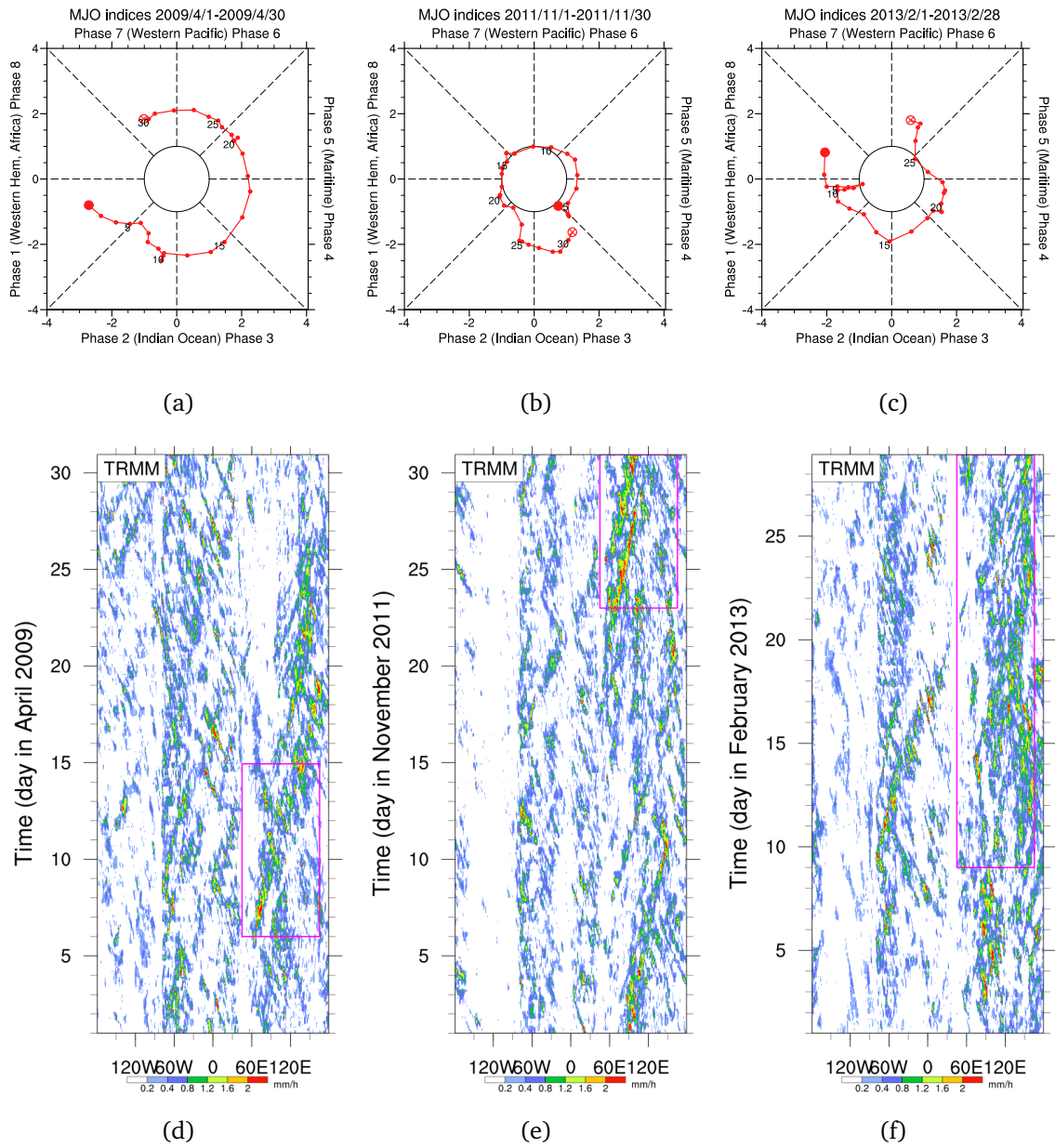


Figure 3.1: Top: RMM indices for (a) April 2009, (b) November 2011, and (c) February 2013, from the Bureau of Meteorology (Australia) Web site <http://www.bom.gov.au/climate/mjo/>. ●, the beginning; ⊗, the end of the corresponding month. Bottom: Hovmöller diagram of TRMM precipitation (mm h^{-1}) averaged between 7.5°S – 7.5°N for (d) April 2009, (e) November 2011, and (f) February 2013. The rectangles show the spatiotemporal domains of study.

tween 7.5°S – 7.5°N to better extract the MJO signal close to the equatorial band, as it is often done in the literature. The rectangles show the spatiotemporal domain of study containing the MJO signal. The vertical lines denote the longitudinal zone of interest, while the horizontal lines show approximate temporal boundaries of convective activity in this domain as chosen previously based on the RMM diagrams. The MJO signal in precipitation is well visible in cases of 2009 and 2011 (Figs. 3.1d,e). It is much weaker and dispersed but still existing, in case of 2013 (Fig. 3.1f), as opposed to Fig. 3.1c where the amplitude of the MJO signal was generally outside the unity circle. This also shows the difficulty to define an MJO signal using the RMM diagrams only. It can be said that the MJO is not well defined in this case, and the episode of February 2013 will be further used for the comparison with two other cases where the MJO signal was strong. Thus, the periods of 6–14 April 2009, 23–30 November 2011, and 9–28 February 2013 were selected for the simulation.

3.2 Simulations of three MJO events

An assessment of the simulations is presented for every selected MJO event. It is done for the simulations at both low and high resolutions (LowRes and HiRes, respectively). Results are shown in terms of distribution of precipitation, eastward propagation of precipitation and its coupling with the zonal wind, and diurnal cycle of precipitation.

3.2.1 Initial conditions: distribution of surface pressure and SST

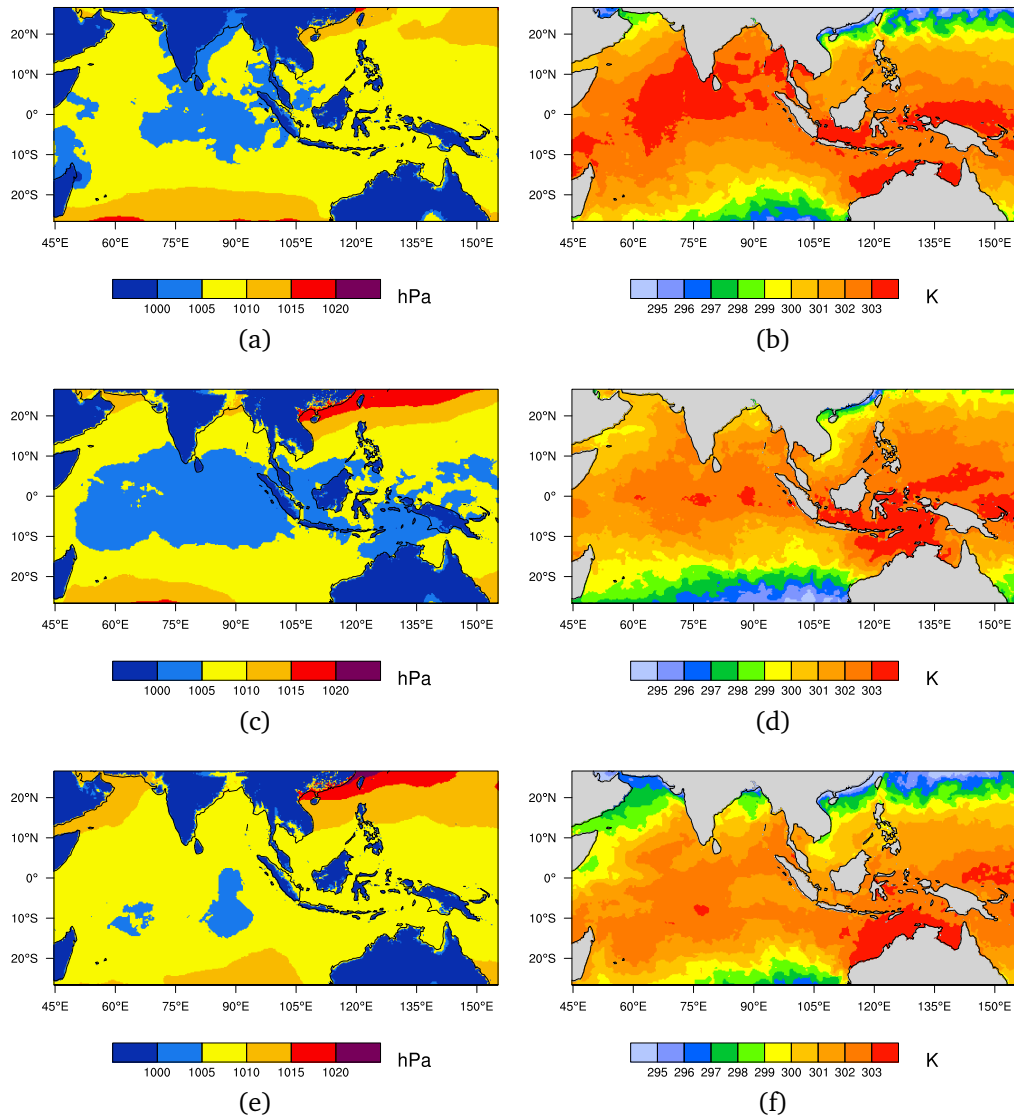


Figure 3.2: Spatial distribution of the initial conditions (taken from the ECMWF analyses): surface pressure (hPa; a,c,e) and SST (K; b,d,f). Cases of 2009, 2011, and 2013.

The initial distributions for the surface pressure and the SST for all cases of study is shown in Fig. 3.2. The surface pressure (Fig. 3.2a,c,e) has lower values (620–1000 hPa) over the land, while over the ocean the pressure is up to 1020 hPa. In all cases, there is a zone of lower pressure over the equatorial Indian Ocean (1000–1005 hPa). For the case of 2011, the surface pressure over the Indian Ocean and the Maritime Continent is lower than for the other two cases. The pressure is higher over the ocean part in the north and the south of the simulation domain.

The SST (Fig. 3.2b,d,f) has lower values at higher latitudes in the south and the north of the simulation domain. The highest values are located at the northern and the equatorial part of the Indian Ocean, the ocean part of the Maritime Continent, and near the northern Australia.

3.2.2 Distribution of precipitation

The **spatial distribution of the mean precipitation** for TRMM, LowRes, and HiRes for every episode is shown in Figs. 3.3–3.5. For better visualization, HiRes and LowRes simulations were adapted to TRMM grid.

For the 2009 event (Fig. 3.3), TRMM shows the most intensive precipitation over the central and eastern Indian Ocean with amplitudes up to 30 mm day^{-1} . Strong precipitation exists also over the Maritime Continent, especially in its central region (Sumatra and Borneo). The Severe Tropical Storm Jade (3–14 April) is seen that was located around (50°E , 16°S) on 4 April and then moved towards the southern boundary of the simulation domain. Also, the initiation of the Cyclonic Storm Bijli (14–17 April) is visible that started to form on 14 April from an organized area of rains and thunderstorms over the southeast Bay of Bengal.

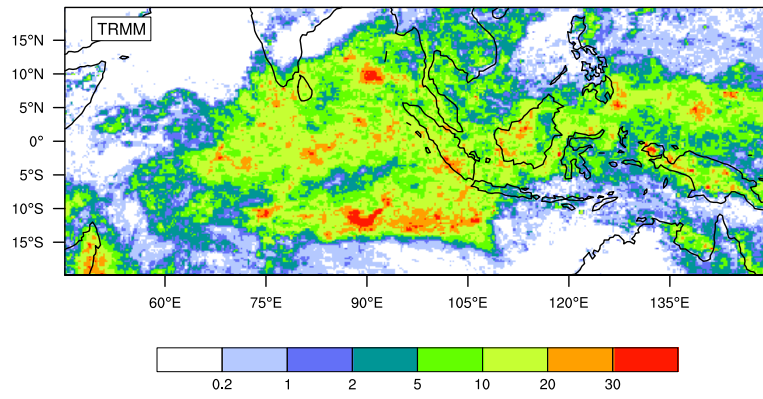
In LowRes, there exists a deficit in precipitation over the central Indian Ocean and an excess in the southwestern part of the simulation domain. Over the Maritime Continent, the precipitation is mostly concentrated over the islands. HiRes reproduces the mean precipitation pattern over the Indian Ocean better, even though it still gives a precipitation deficit near the equator over the Indian Ocean and over the ocean part of the Maritime Continent. In both simulations, the Severe Tropical Storm Jade is also visible and gives stronger precipitation than in TRMM, while the formation of the Cyclonic Storm Bijli is not seen. Another common feature of the two simulations is the presence of a large amount of weak rain (less than 1 mm day^{-1}) which is absent in TRMM. Nevertheless, TRMM precipitation product might be not able to well reproduce weak rain rates due to such factors as instrument measurement thresholds, calibration and combination of different instruments, or the approximations used in the calculating of 3B42 product, thus it is not possible to estimate the quality of the simulations for weak precipitation.

For the 2011 event (Fig. 3.4), strong precipitation in TRMM is located along the equator over the Indian Ocean extending to the south and north up to 10° – 15° latitudes. Precipitation is also intensive over the Maritime Continent though its amplitude is weaker. Also, the path of the Deep Depression ARB 04 (26 November – 1 December) is visible moving along the southwestern side of the Indian subcontinent. In both LowRes and HiRes, the areas where the intensive precipitation is concentrated are fairly well reproduced. LowRes however shows weaker precipitation over the Maritime Continent and an excess of precipitation in the northeast and the west of the simulation domain. HiRes gives more scattered precipitation but the spatial patterns are well reproduced. The path of the Deep Depression ARB 04 is clearly visible in LowRes while having higher intensity than in TRMM. In HiRes, it is visible but much weaker.

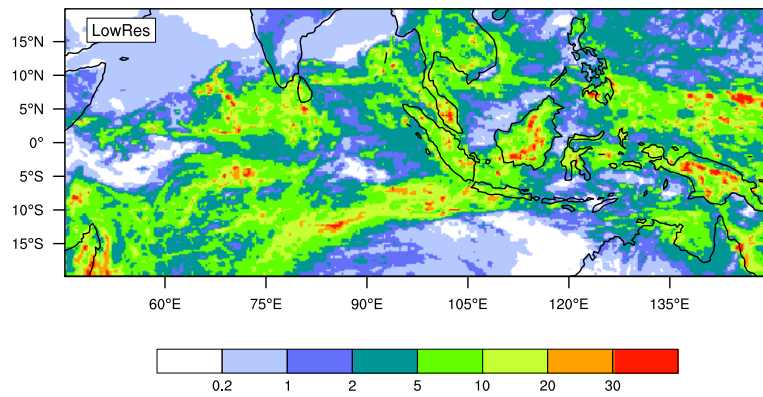
For the 2013 event (Fig. 3.5), the strongest precipitation in TRMM is located in the eastern part of the simulation domain. It is weaker over the Indian Ocean. In both simulations, there is a deficit of precipitation near the equator over the Indian Ocean. The precipitation over the Maritime Continent is located mostly over the islands, contrary to TRMM. The simulations also overestimate the rainfall associated with cyclones, located around 15°–20°S: Tropical Cyclone Haruna (14–28 February, 45°E), Tropical Cyclone Gino (11–15 February, 80°E), and Severe Tropical Cyclone Rusty (22 February – 5 March, 120°E). The cyclones are less noticeable in TRMM data.

To provide a quantitative assessment, precipitation accumulated over the simulation period is calculated over the whole domain (Table 3.1). The both simulations have lower values of the total accumulated precipitation in the 2009 and 2013 episodes than TRMM. LowRes shows an excess in the total accumulated precipitation as compared to TRMM, in the 2011 episode. HiRes gives the lowest values for all three episodes.

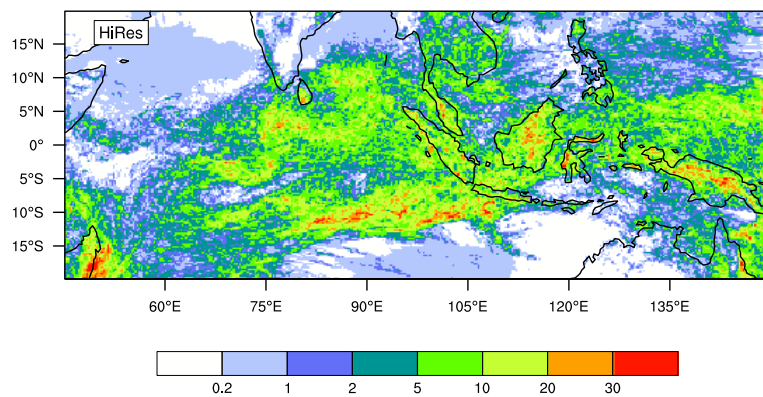
When examining the average total precipitation values per day (Table 3.2), the episode of 2011 had the highest average total precipitation values per day as compared to 2009 and 2013 episodes. The simulations show less precipitation than TRMM with the exception of LowRes in 2011.



(a)

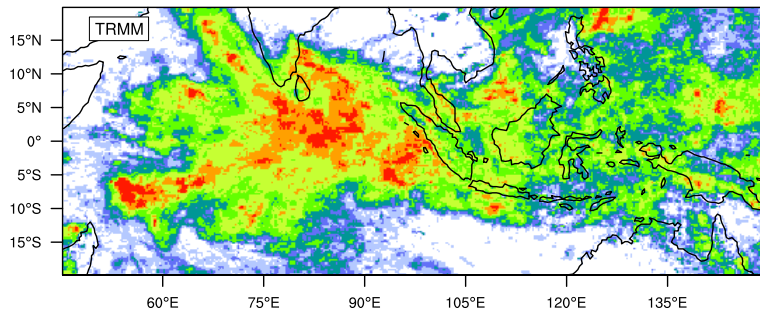


(b)

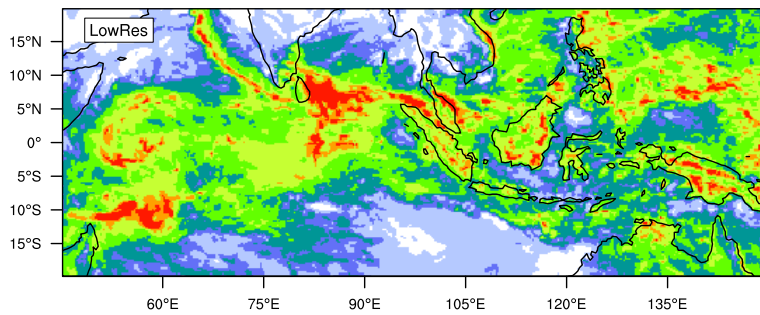


(c)

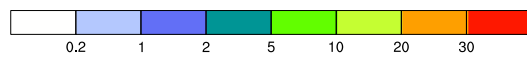
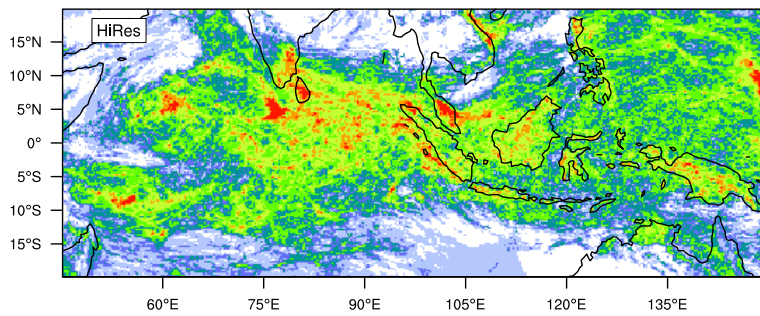
Figure 3.3: Spatial distribution of mean precipitation (mm day^{-1}) for 6–14 April 2009. (a): TRMM, (b): LowRes, (c): HiRes.



(a)

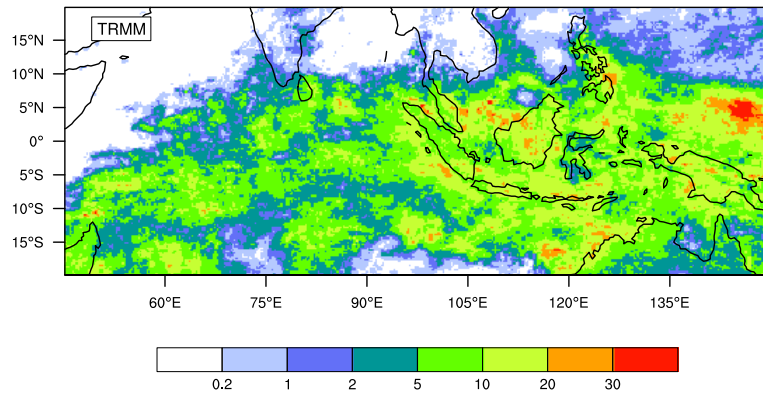


(b)

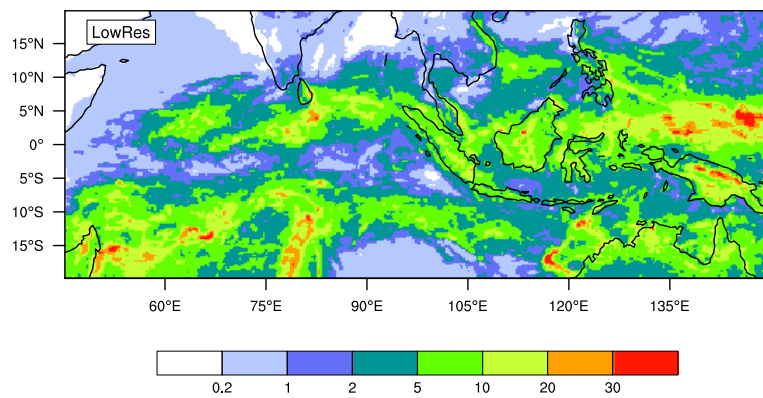


(c)

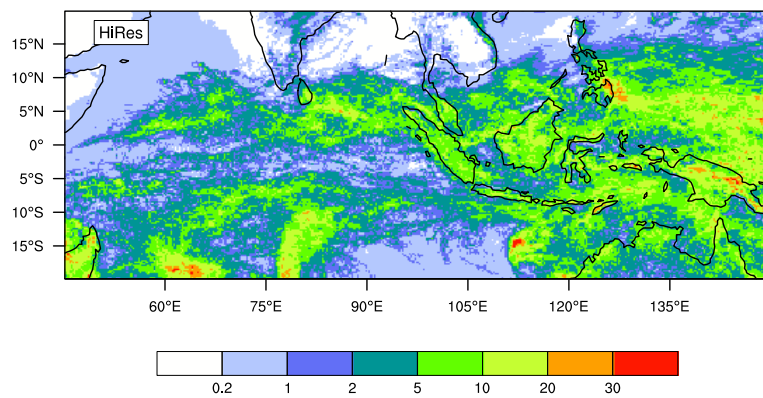
Figure 3.4: As in Fig. 3.3, but for 23–30 November 2011.



(a)



(b)



(c)

Figure 3.5: As in Fig. 3.3, but for 9–28 February 2013.

Episode / Data	TRMM	LowRes	HiRes
2009	48.14	43.60	37.76
2011	53.64	57.33	43.81
2013	112.07	97.03	81.49

Table 3.1: Accumulated precipitation (mm) for TRMM, LowRes, and HiRes.

Episode / Data	TRMM	LowRes	HiRes
2009	5.35	4.84	4.20
2011	6.71	7.17	5.48
2013	5.60	4.85	4.07

Table 3.2: Average precipitation per day (mm day^{-1}) for TRMM, LowRes, and HiRes.

In the LowRes simulations, the total precipitation is the summation of the **explicit precipitation** and **parameterized precipitation**, i.e. due to convective parameterizations. To better understand the generating of precipitation in the LowRes simulations, the spatial distribution of both precipitation types is shown in Figs. 3.6–3.8.

In the episode of 2009, the parameterized part of the precipitation has values around $1\text{--}20 \text{ mm day}^{-1}$ (Fig. 3.6a) and covers the large part of the simulation domain. The zones with rain values $5\text{--}20 \text{ mm day}^{-1}$ are visible as large-scale elongated zones over the Indian Ocean and zones close to or covering the islands of the Maritime Continent. The explicit part (Fig. 3.6b) has wider range of precipitation values. Weak rain (less than 1 mm day^{-1}) is seen in large zones near the northern and southern boundaries of the domain, closer to the subtropics (around $45^\circ\text{--}75^\circ\text{E}$, $5^\circ\text{--}20^\circ\text{N}$; $80^\circ\text{--}95^\circ\text{E}$, $10^\circ\text{--}20^\circ\text{N}$; and $90^\circ\text{--}110^\circ\text{E}$, $15^\circ\text{--}20^\circ\text{S}$), and several elongated zones near the equator accompanying the zones with stronger rain. Stronger rain is more scattered and generally corresponds to the isolated storms, which are thus represented by both explicit and parameterized precipitation. Also, the Severe Tropical Storm Jade in the left lower corner of the domain is seen as an increase in both explicit and parameterized

precipitation. The corresponding contribution of the explicit and parameterized parts to the total precipitation in every grid point is shown in Figs. 3.6c–d. Over the large part of the simulation domain, the percentage of the parameterized precipitation exceeds 90%. The highest percentage of the explicit precipitation (exceeding 90%) is located in two large zones in the northeastern part of the domain as well as in the zone 90°–110°E, 15°–20°S that correspond to the weak rain as shown previously. A zone with slightly lower percentage (40–90%) corresponds to the location of the Severe Tropical Storm Jade. For the isolated storms, the percentages of both convective and explicit rain are around 40–80%.

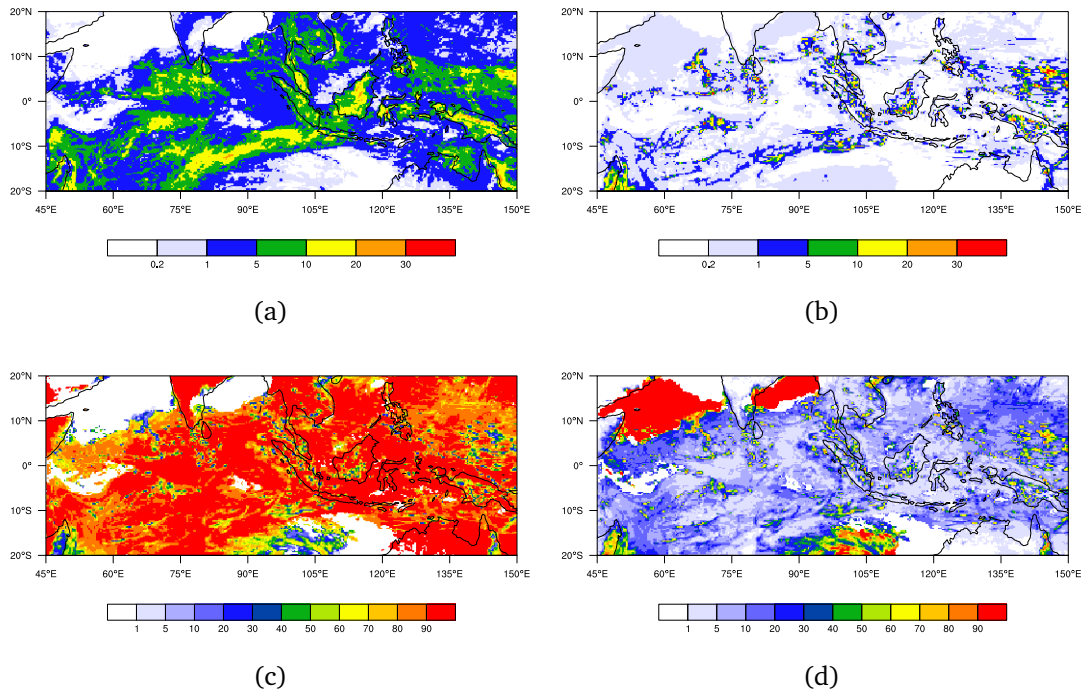


Figure 3.6: Spatial distribution of mean precipitation (in mm day^{-1} ; a,b) vs spatial distribution of the percentage of mean precipitation (in %; c,d) for LowRes, case of 2009. (a,c): parameterized precipitation, (b,d): explicit precipitation. Mean precipitation less than 0.2 mm day^{-1} was not included in the calculation.

A similar pattern is seen for the cases of 2011 (Fig. 3.7) and 2013 (Fig. 3.8). For 2011, the parameterized part of the precipitation (Fig. 3.7a) has values

around $1\text{--}20\text{ mm day}^{-1}$ in the large part of the domain and the corresponding percentage exceeds 90% (Fig. 3.7c). There is more parameterized precipitation exceeding 10 mm day^{-1} near the equator than in 2009 case. The explicit part (Fig. 3.7b) has several zones with weak precipitation which are not visible in the parameterized part, the corresponding percentage exceeds 90% (Fig. 3.7d). Stronger explicit precipitation with the percentage of 40–90% is scattered and corresponds to the isolated storms or MCSs, they are more developed and their number is more than in 2009 case. The path of the Deep Depression ARB 04 is more pronounced in the explicit precipitation, with the values exceeding 30 mm day^{-1} while the parameterized precipitation gives the values less than 20 mm day^{-1} .

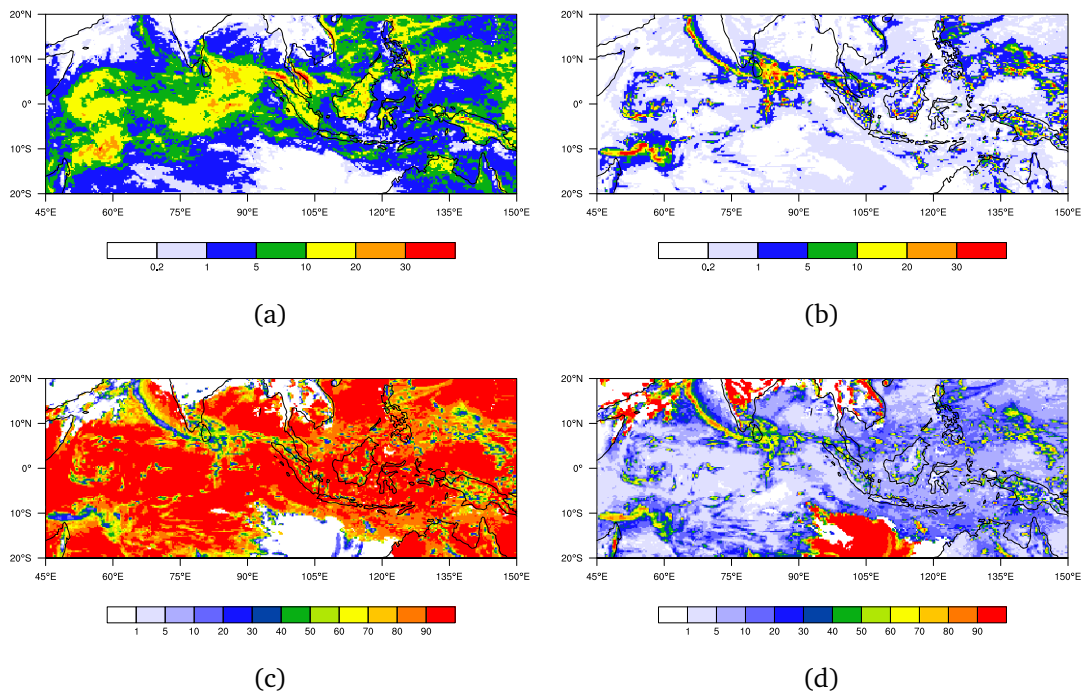


Figure 3.7: As in Fig. 3.6, but for the 2011 episode.

For 2013, it was shown that there is a strong deficit in the simulated precipitation near the equator over the Indian Ocean (Fig. 3.5). Here, this zone

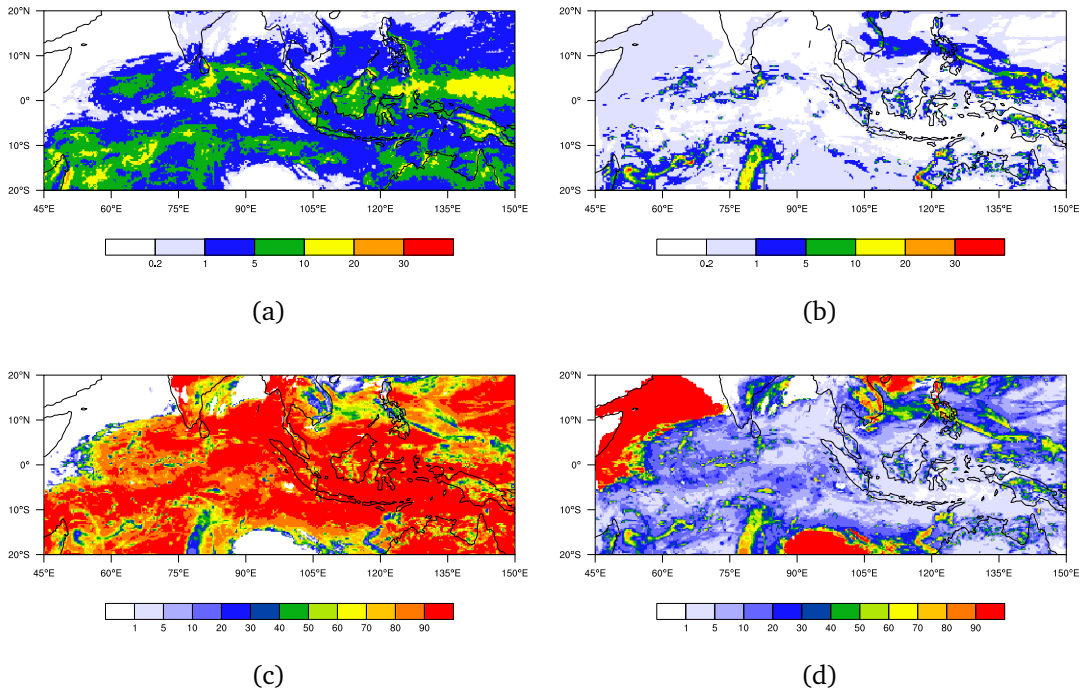


Figure 3.8: As in Fig. 3.6, but for the 2013 episode.

can be seen as an elongated zone near the equator with the weak precipitation in the parameterized part (Fig. 3.8a) and almost no corresponding explicit precipitation (Fig. 3.8b). Apart from that, the general pattern is similar to the two other episodes, with the parameterized precipitation having high percentage values in the large part of the domain (Fig. 3.8c) and the high-percentage explicit precipitation showing scattered isolated storms and the cyclones Gino and Rusty (Fig. 3.8d).

In other words, the parameterized part of LowRes simulations generally reproduces the large-scale organized rain patterns while the explicit part reproduces smaller-scale patterns such as cyclones. This happens because the explicit part shows the precipitation due to the systems which are larger than the size of a grid cell. These systems are localized and their number is not large while the convection in these systems is strong. At the same time, the parameterized

part shows the precipitation with the scales less than the size of a grid cell. The number of the grid cells in this case is larger and the convection is less intensive.

The **frequency distributions of grid points for different precipitation rates** for TRMM, LowRes, and HiRes are shown in Fig. 3.9. The precipitation rates where the corresponding number of grid points was less than 10, were excluded. Figures 3.9d–e show the zoom of Figs. 3.9a–c for low precipitation rates.

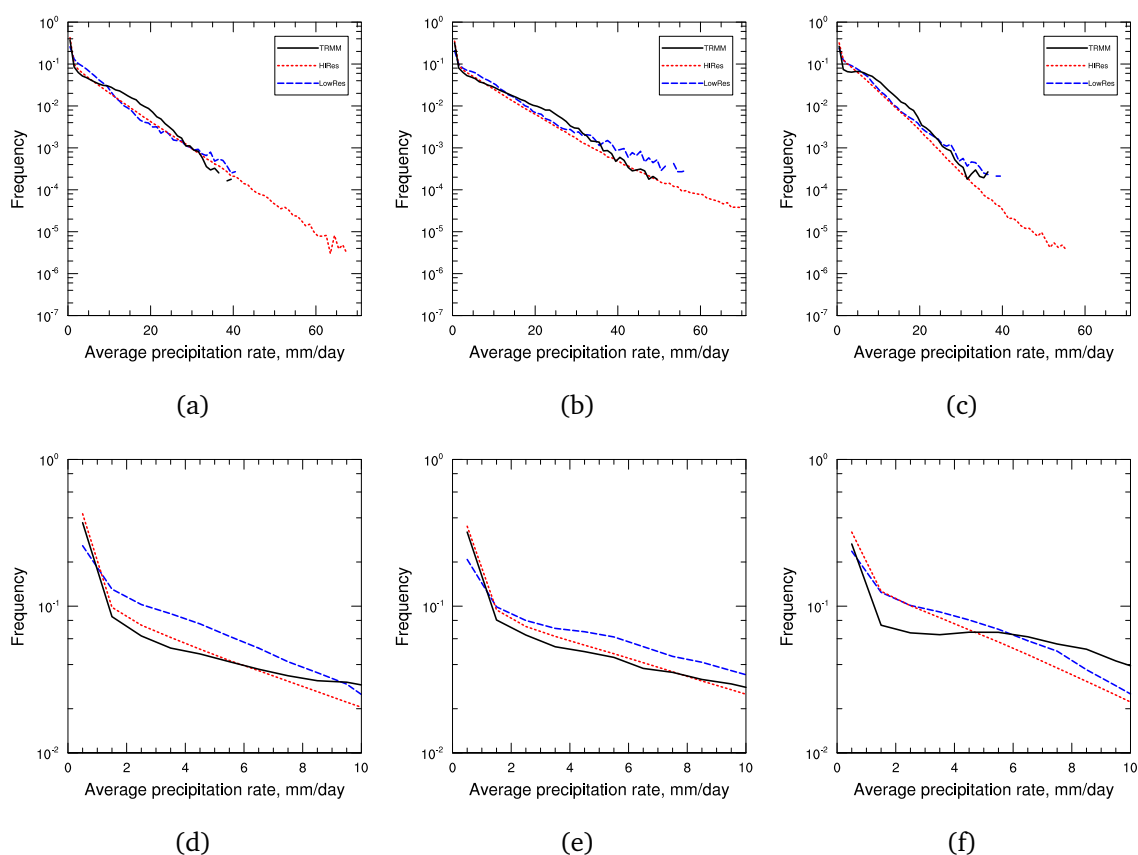


Figure 3.9: Frequency distribution of grid points for precipitation. (a,d): 6–14 April 2009, (b,e): 23–30 November 2011, (c,f): 9–28 February 2013. — (black), TRMM; - - (red), HiRes; - - (blue), LowRes. (d–e) show the zoom of (a–c) for low precipitation values.

TRMM and HiRes give similar frequency values for the weak rain (less than 1 mm day^{-1} for 2009 and 2011 cases and less than 0.6 mm day^{-1} for 2013 case)

while the corresponding values for LowRes are lower. Then, HiRes and LowRes have higher frequency as compared to TRMM up to some specific precipitation rate r_1 (different for HiRes and LowRes as well as for the episode). After that, HiRes and LowRes have lower frequency than TRMM up to some other precipitation rate r_2 . Close to this point, TRMM and LowRes curves start fluctuating due to the insufficient number of grid points for these rain rates. On the contrary, HiRes is able to reproduce higher rain rates — up to 65 mm day^{-1} for 2009, 70 mm day^{-1} for 2011, and 55 mm day^{-1} for 2013. For the case of 2011, it is also visible that for precipitation rates above 40 mm day^{-1} , HiRes gives similar values as TRMM.

3.2.3 Eastward propagation of the precipitation signal

The MJO eastward propagation is assessed by looking at the propagation of the precipitation along the equatorial band in the simulation domain. In the following, Hovmöller diagrams are shown for the three episodes in which precipitation is averaged between 7.5°S and 7.5°N .

In case of 2009, TRMM (Fig. 3.10a) shows an MJO signal that appears at 60°E on 6 April and propagates towards the east, reaching 135°E on 15 April. There is also another weaker east-propagating convective feature in TRMM that appears around 95°E on 6 April and disappears around 115°E on 8 April. In LowRes (Fig. 3.10b), two convective signals appear on 6 April, one corresponding to the MJO (around 60°E) and the other corresponding to the second east-propagating convective feature existing in TRMM. Nevertheless, neither of these features do not propagate towards the east and are almost stationary. In the eastern part of the simulation domain, weak rain is present which is not seen in TRMM. In HiRes (Fig. 3.10c), a well-developed east-propagating convective feature corre-

sponding to the MJO signal, is present from 6 to 11 April. It appears over 65°E and propagates further through a part of the Maritime Continent, up to 120°E. The second east-propagating convective feature is also present and is well reproduced comparing to TRMM, appearing at 100°E on 6 April and weakening at 120°E on 8 April. The improvement in the representation of the MJO eastward propagation by using simulations with explicit convection was also noted in the study of the same MJO episode by Holloway et al. (2013).

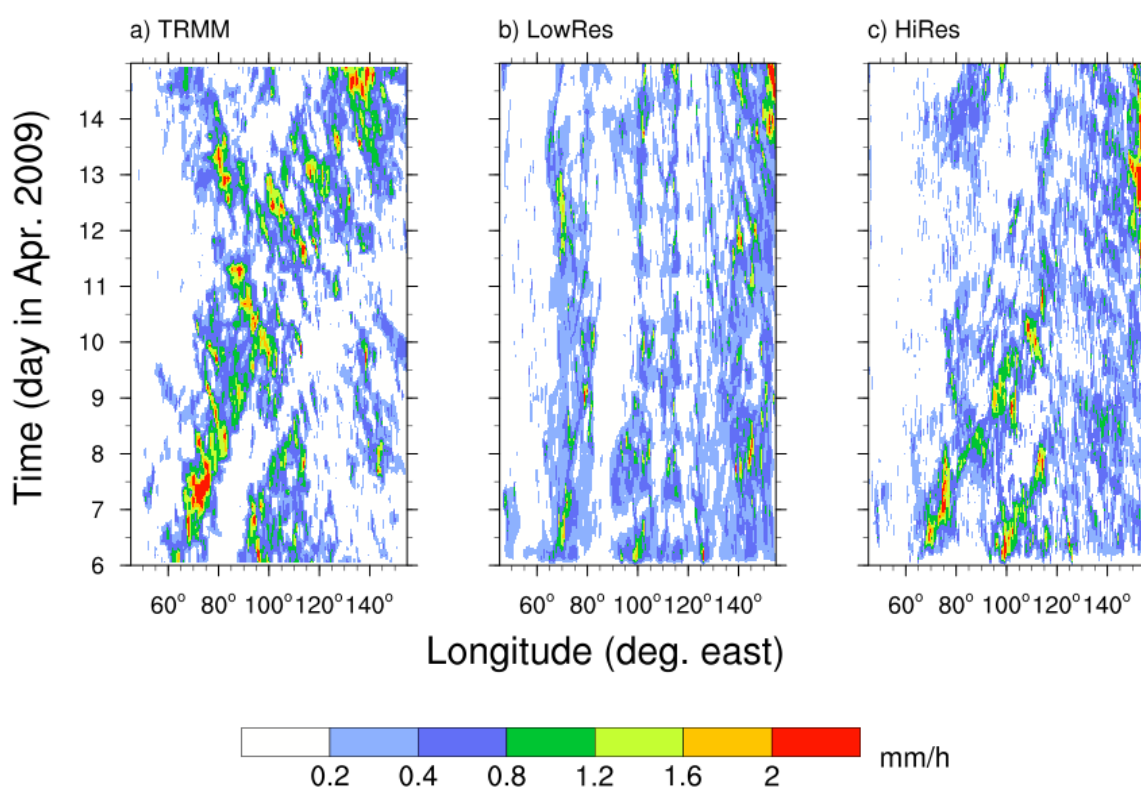


Figure 3.10: Hovmöller diagram of precipitation (mm h^{-1}) averaged between 7.5°S and 7.5°N for the April 2009 event. Fields are taken from (a) TRMM, (b) LowRes and (c) HiRes.

In case of 2011, TRMM (Fig. 3.11a) shows two strong eastward-propagating convective features over the Indian Ocean. They are separated by a break of

1–2 days that corresponds to dry air intrusions (Kerns and Chen, 2014). The first eastward-propagating feature appears around 60° – 70° E on 23 November and propagates towards the Maritime Continent, reaching it around 27 November. The second one appears at 55° – 65° E around 26 November and propagates similarly to the first one, reaching 100° E around 1 December. Convective activity is also present around 100° – 110° E on 23 November, weakening on 24 November. In LowRes (Fig. 3.11b), convective activity corresponding to the first eastward-propagating feature starts developing around 65° – 70° E on 23 November and further propagates towards 80° E. Then around 1200 UTC 24 November, there is a merging/splitting point with multiple signals, the strongest one starts moving back towards the west and finally stops while others decay earlier. The second eastward-propagating feature is present, appearing around 60° E on 25 November and weakening around 80° E on 29 November, but it has the amplitude much weaker and the horizontal extent much smaller than in TRMM. In HiRes (Fig. 3.11c), convective activity corresponding to the first eastward-propagating feature wave starts developing on 23 November around 60° – 75° E and further propagates towards the Maritime Continent (up to 100° E) until 28 November. On 24 November, the convective signal at 80° E divides into two parts, one continuing the eastward motion while the second is stationary and later weakens around 26 November. The second eastward-propagating feature appears around 60° E on 25 November and is initially weak but then starts developing, nevertheless remaining weaker than in TRMM.

In case of 2013, TRMM (Fig. 3.12a) shows that the signal is not continuous but is scattered, consisting of multiple small bursts of convection. During 9–11 February, there is some weak convective activity around 55° E, 85° E, and 105° E. Then, a precipitation maximum appears around 80° E on 13 February. Multiple bursts are then appearing, new ones forming over the Maritime Continent and

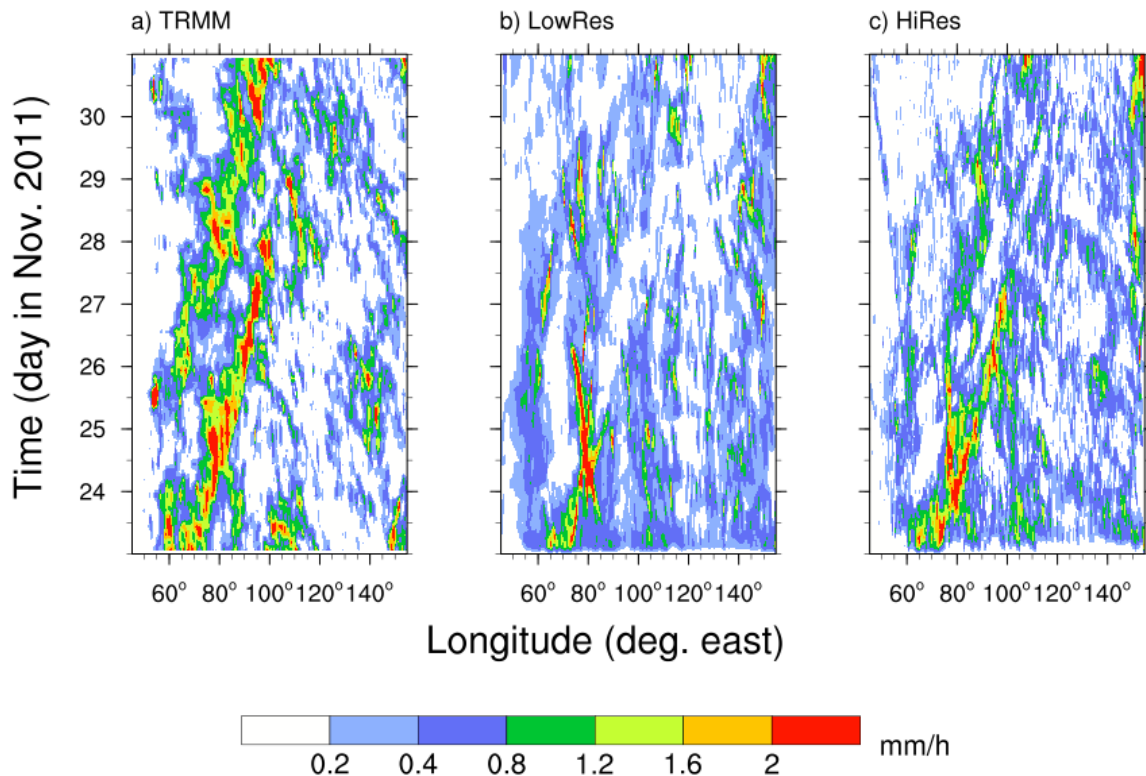


Figure 3.11: As in Fig. 3.10, but for the November 2011 event.

quickly weakening. It is possible to see that convective activity as a whole moves eastward. Over the Indian Ocean, the activity is weak during 12–27 February. In this case the MJO activity is generally weaker and a large number of small-scale convective systems can be clearly seen inside a large-scale envelope. In both LowRes (Fig. 3.12b) and HiRes (Fig. 3.12c), there is no distinct MJO signal. There is some convective activity in the east of the domain not related to the MJO. Also, in both cases a lot of weak precipitation is seen with the noticeable diurnal cycle, while there are very few convective systems with the amplitude exceeding 1.2 mm h^{-1} .

In summary, the LowRes simulations fail to reproduce the eastward propaga-

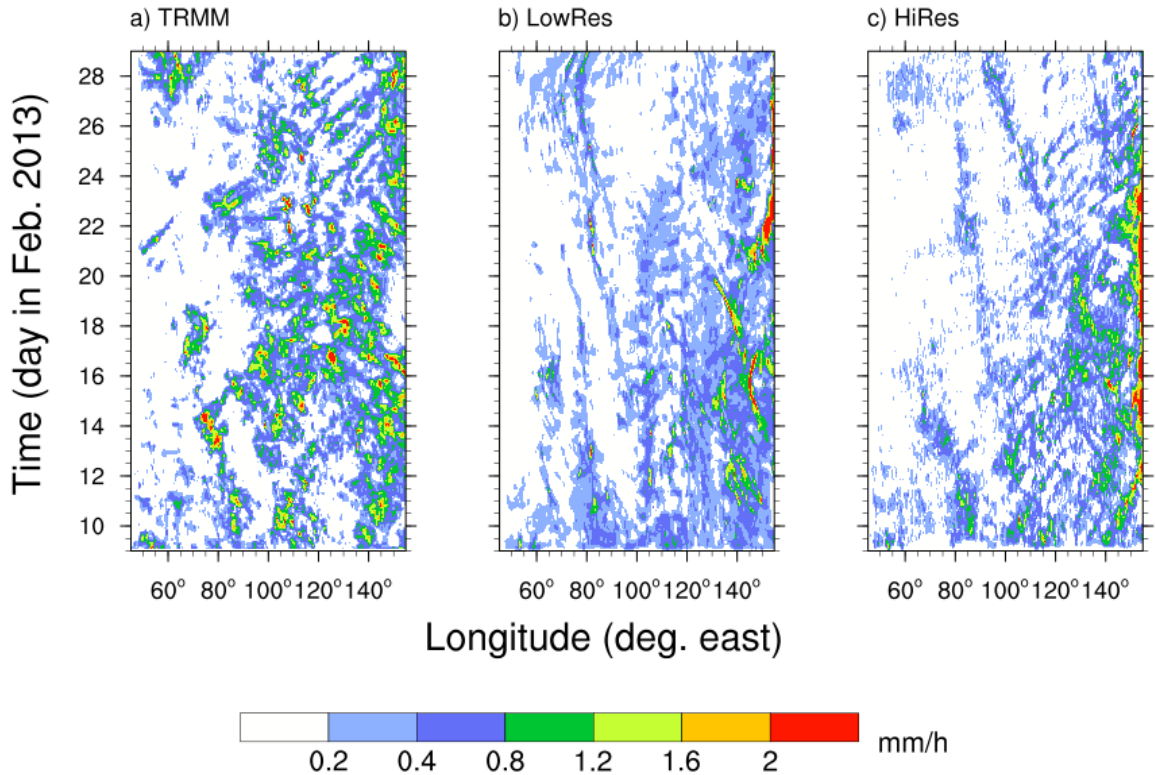


Figure 3.12: As in Fig. 3.10, but for the February 2013 event.

tion of precipitation. For both 2009 and 2011 MJO episodes, HiRes simulations succeed to represent the eastward propagation over the Indian Ocean and the part of the Maritime Continent, while for the February 2013 event there was no distinct MJO signal in HiRes.

3.2.4 Coupling of the precipitation and the zonal wind signals

The Hovmöller diagrams of the zonal wind velocity anomalies at 200 hPa and 850 hPa in ECMWF analyses, LowRes, and HiRes are shown in Figs. 3.13–

3.15. The contours show the 0.8 mm h^{-1} value of the 5-day running means for precipitations, where in Figs. 3.13a,d, Figs. 3.14a,d, and Figs. 3.15a,d, the precipitation fields are taken from TRMM. All the fields are averaged between 7.5°S and 7.5°N .

The anomalies represent the difference between the zonal wind velocity and the long-term climatology calculated with the NCEP/NCAR reanalyses. This allows to better capture the MJO signal in the circulation. The active MJO phase is characterized by the low-level convergence and the high-level divergence. As explained previously, often the 850 hPa and 200 hPa levels are considered. In each of Figs. 3.13–3.15, the plots in the top show the zonal wind velocity anomalies at 200 hPa and the plots in the bottom show the zonal wind velocity anomalies at 850 hPa. The positive values correspond to the eastward direction while the negative values correspond to the westward direction.

For the case of 2009, the MJO signal in ECMWF data is clearly visible, with the zonal wind anomaly convergence at the low levels and divergence at the high levels. The TRMM precipitation signal is propagating along the line dividing the positive and negative zonal wind anomalies. Two eastward-propagating precipitation features originating around 70°E and 100°E correspond to the zones where the zonal wind anomalies change the sign. In LowRes, the signal in the anomalies is stationary at 200 hPa and almost not visible at 850 hPa. Positive and negative anomalies exist but there is no eastward propagation, similarly to the simulated precipitation field. HiRes reproduces well the signal despite giving lower amplitudes for the zonal wind velocity anomalies. Both eastward-propagating precipitation features have also the corresponding signature in the wind anomalies, where the anomalies change sign or become closer to zero.

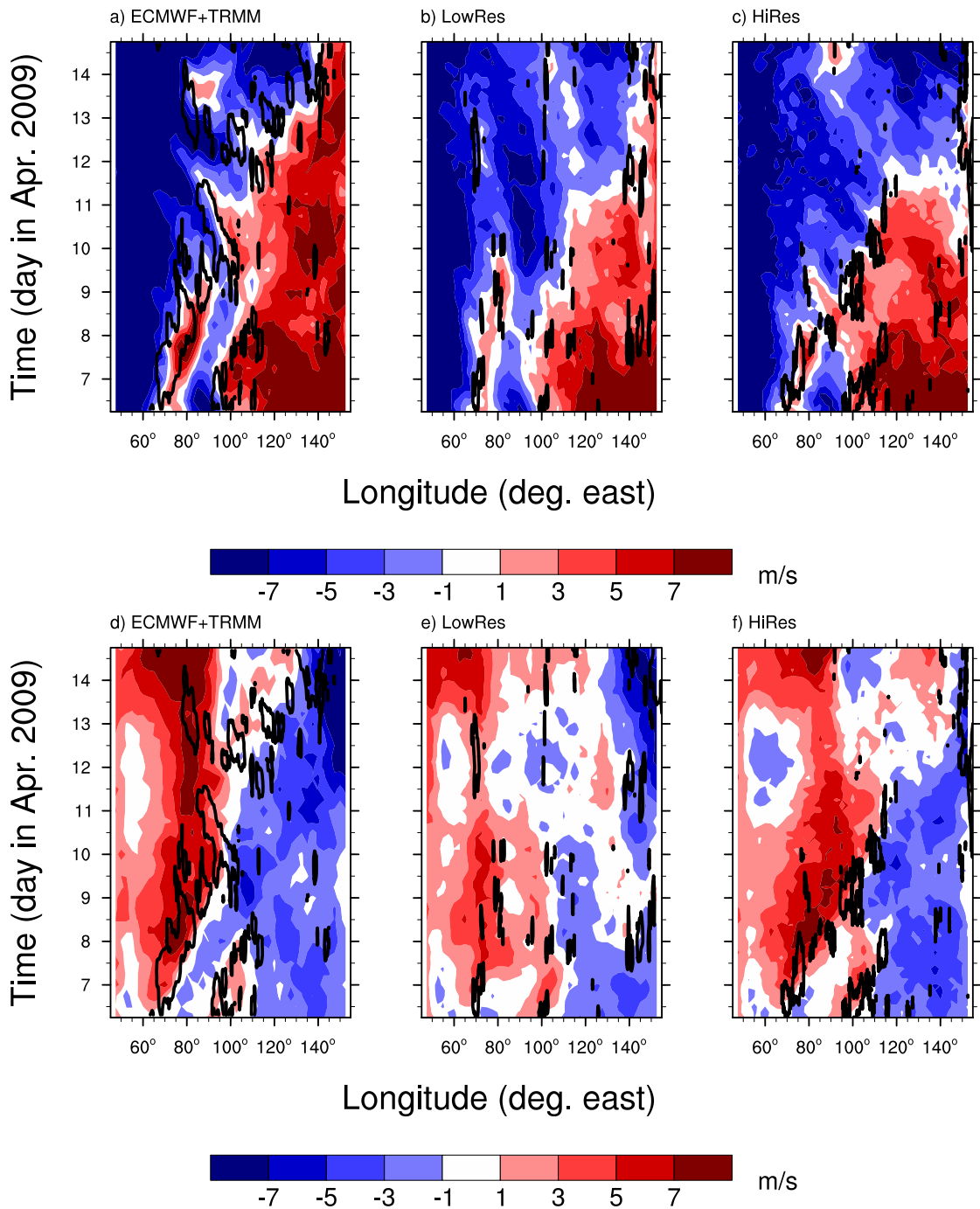


Figure 3.13: Hovmöller diagram of the zonal wind velocity anomalies at (a)–(c) 200 hPa and (d)–(f) 850 hPa (m s^{-1}) averaged between 7.5°S and 7.5°N for the April 2009 event. Contours correspond to the 5-day running mean of the 0.8 mm h^{-1} precipitation. Fields are taken from (a,d) ECMWF analysis and TRMM, (b,e) LowRes and (c,f) LowRes. The anomalies were obtained with the long-term climatology fields calculated from the NCEP/NCAR reanalyses.

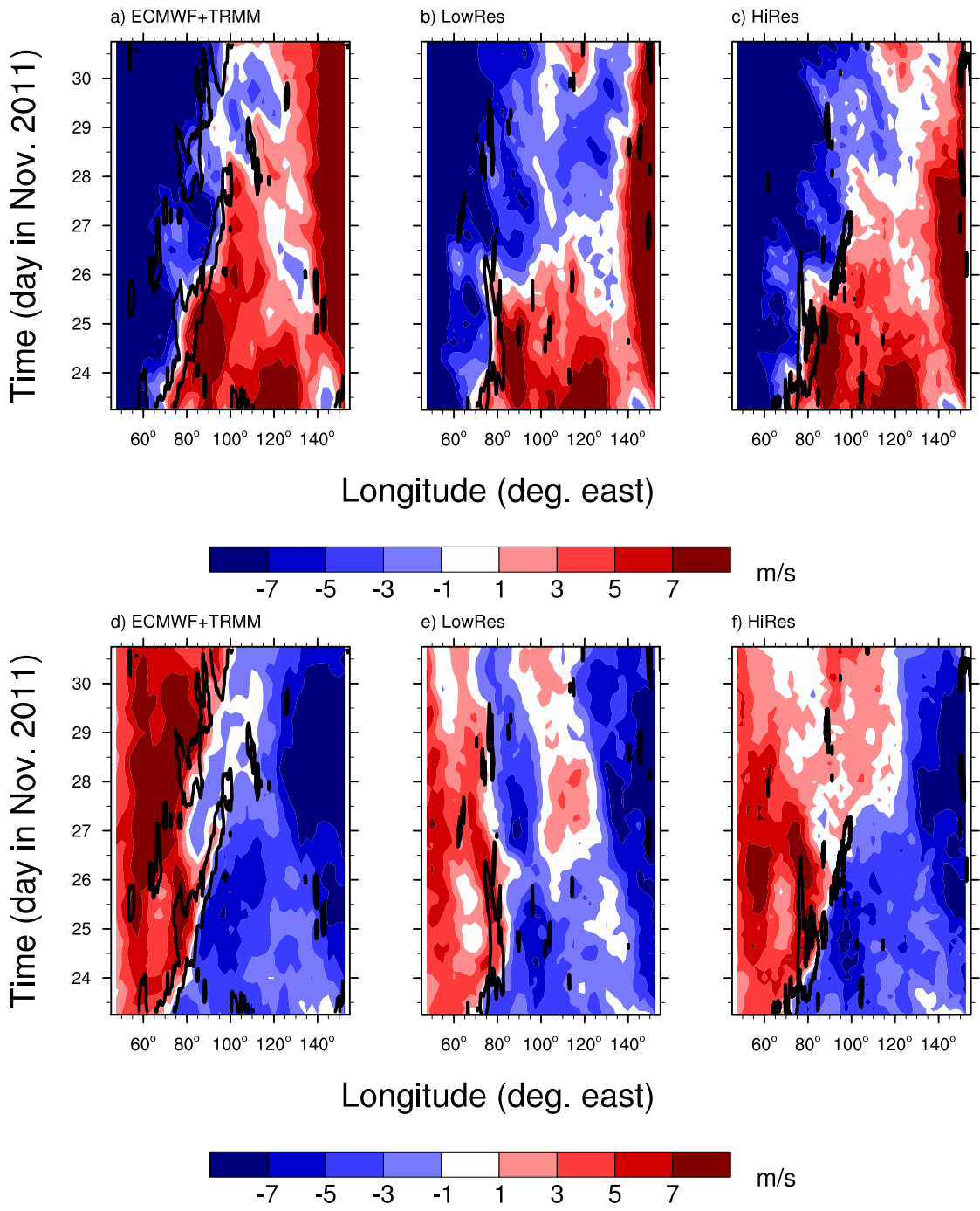


Figure 3.14: As in Fig. 3.13, but for the November 2011 event.

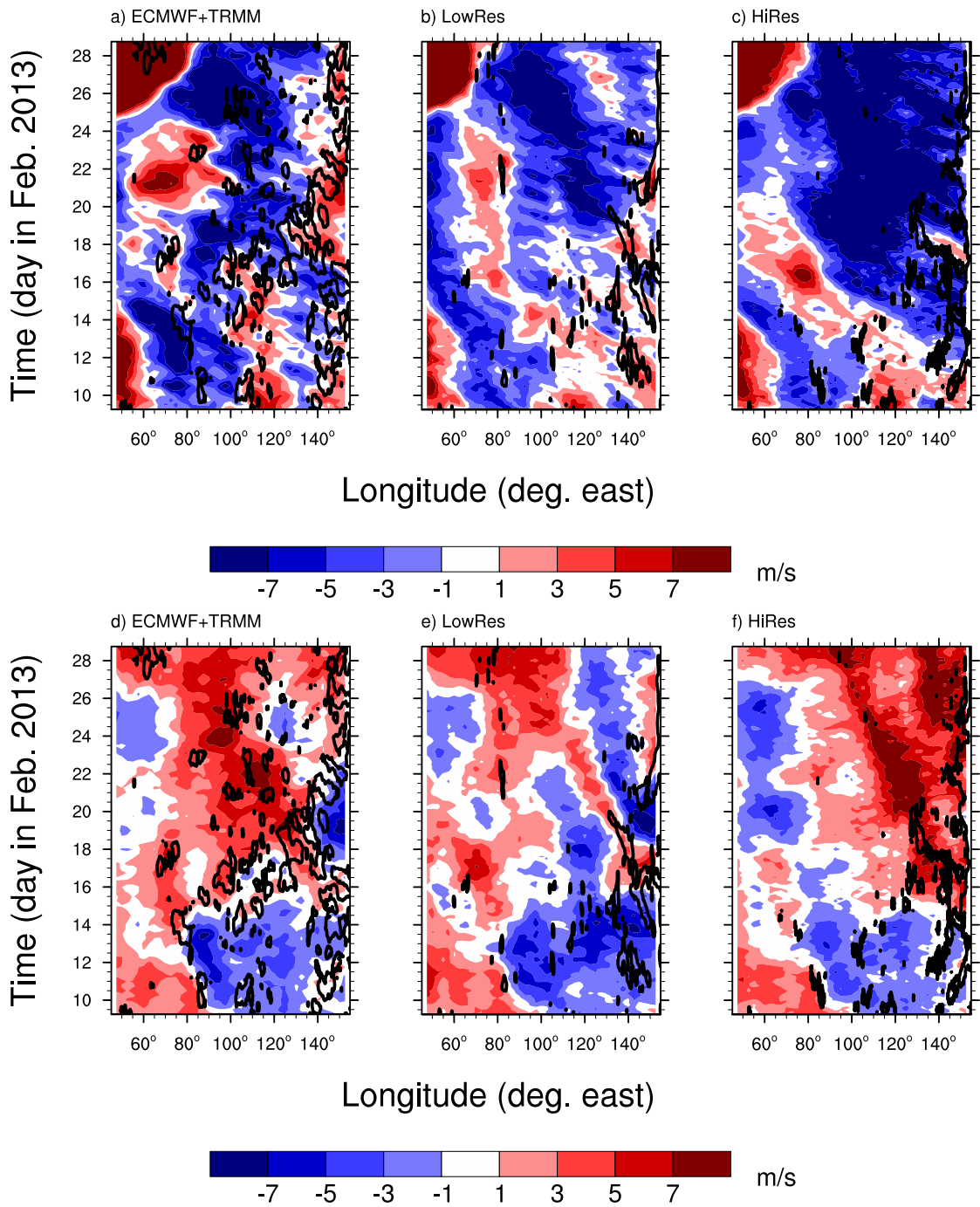


Figure 3.15: As in Fig. 3.13, but for the February 2013 event.

For the case of 2011, the signal in ECMWF is also distinct, with the zonal wind anomaly convergence at the low levels and divergence at the high levels. At 200 hPa level, one of the two eastward-propagating features in precipitation follows the line where the anomalies change sign, while the other is located in the zone with the negative anomalies corresponding to the increasing in the anomaly amplitude. At 850 hPa level, the first eastward-propagating feature also follows the sign-changing line until reaching 100°E, where both the wind convergence and the precipitation feature disappear. The second feature starts in the zone with the positive wind anomaly and corresponds to the increase in the amplitude of this anomaly. The dry air intrusion appears which is seen here as a zone with the negative anomaly appearing around 80°E on 26 November, and the second feature propagates further following the sign-changing line. In LowRes, the signal corresponding to the first of these features can be seen in the beginning of the simulation as the convergence in the lower troposphere and divergence in the upper troposphere, but it stops propagating towards the east around 25 November. The second feature is not very visible in LowRes. In HiRes, the first eastward-propagating feature can be tracked in the zonal wind anomalies, where it is quite distinct. The second feature is weaker in precipitation and also in the anomalies, as the wind is weaker in HiRes than in ECMWF.

The case of 2013 is different from the two previous cases. In upper-level anomalies, the MJO signal is not very distinct as the anomalies consist of several large-scale positive and negative zones. In lower-level anomalies it is more visible as there is a change of sign showing convergence corresponding to the presence of a large number of scattered precipitation zones, though the eastward propagation in the wind anomalies is not continuously present. The general pattern present in the ECMWF anomalies is reproduced in LowRes, but the presence of “additional” positive and negative zones makes observing the MJO signal more

difficult, especially in upper-level anomalies due to the presence of a westward-propagating feature around 14–24 February corresponding to the sign change. The representation of the anomaly signal in HiRes is similar to LowRes and there is no significant improvement even if the convection is no longer parameterized as in LowRes.

The absence of eastward propagation in the zonal wind suggests a decoupling between precipitation and large-scale circulation. To understand the possible reasons for these differences in the simulations, we can look at the MJO indices. As described previously, the RMM index is based on both convection and circulation, while it is also possible to use the separate indices for convection (e.g. the OLR MJO Index, OMI) or circulation (e.g. the Velocity Potential MJO index, VPM).

The MJO indices RMM, OMI, and VPM for the three simulation periods are shown in Fig. 3.16. For 2009 and 2011 cases, all indices show the strong amplitude as the curves are located outside of the unity circle (Figs. 3.16a,b). For the 2013 case, OMI shows strong amplitude during the whole period 9–28 February (Fig. 3.16c). RMM has a fluctuation around 24 February, but the curve is located close to the unity circle. At the same time, VPM show weak amplitude around 22–25 February. Thus, there is a disagreement in the indices. It can be explained by the strength of the MJO signal in convection and circulation, and the coupling between the two. For 2009 and 2011, the coupling between convection and large-scale circulation is strong, thus giving a strong amplitude of the indices. For 2013, the coupling between convection and large-scale circulation is weaker and there is a disagreement in the indices. For this case, the weaker convection-circulation coupling explains the poor capability of the model to simulate the MJO signal.

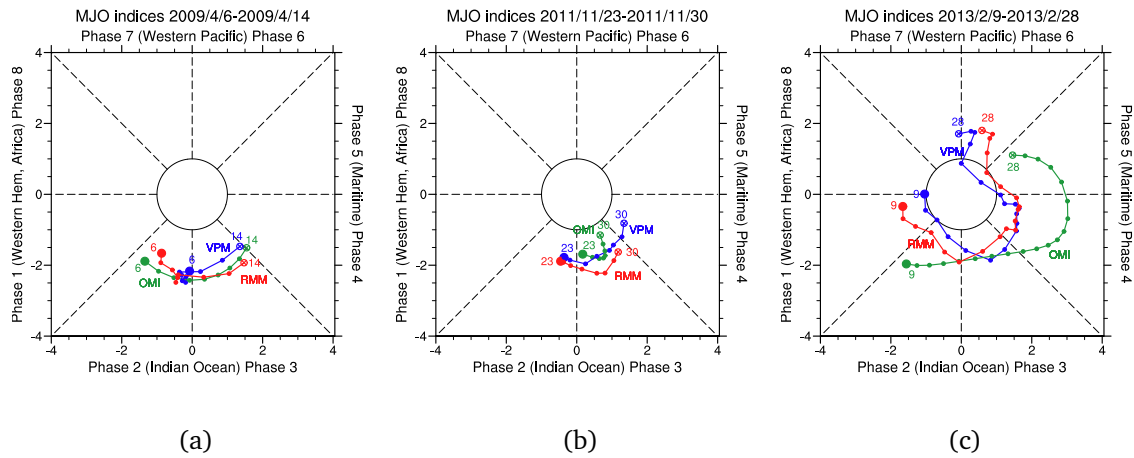


Figure 3.16: RMM (in red), OMI (in green) and VPM (in blue) indices for (a) April 2009, (b) November 2011, and (c) February 2013. Each point corresponds to one day. The dates of the start and the end of every chosen period are indicated. The indices were obtained from <https://www.esrl.noaa.gov/psd/mjo/mjoindex/> and <http://www.bom.gov.au/climate/mjo/>.

3.2.5 Diurnal cycle of precipitation

The diurnal cycle is one of the most important modes of the atmospheric variability in the tropics, together with the MJO. This is due to the diurnal cycle of solar radiation, which results in a stronger daytime boundary-layer heating over land and a upper-tropospheric cooling during night. The Maritime Continent, located in the “warm pool” i.e. a region with the high sea surface temperature, is known for its heavy precipitation and its role in the global atmospheric circulation due to the significant latent heat release (Ramage, 1968; Neale and Slingo, 2003). The presence of the large number of islands mixed with the ocean regions creates an additional issue for models with a too low horizontal resolution. The coarse resolution leads to a too smooth description of the orography, and convective systems are poorly represented due to the parameterization of the convection.

Numerous studies suggest the interaction of the diurnal cycle with the MJO.

While this problem is beyond the scope of this work, the correct representation of the diurnal cycle is important for assessing the model skill. The diurnal cycle of precipitation is examined here by averaging the precipitation for the three MJO episodes with respect to the local solar time (LST). The amplitude and time of the daily precipitation maximum are thus obtained.

The **spatial distribution of the daily precipitation maximum** for the case of 2009 is shown in Figs. 3.17a,c,e for TRMM, LowRes and HiRes. The **corresponding LST of the daily precipitation maximum** is shown in Figs. 3.17b,d,f. For TRMM, there are several peaks over the Indian Ocean and the islands of the Maritime Continent. The time of the daily precipitation maximum over the Indian Ocean shows a noisy signal due to the presence of a large number of isolated storms which peak at different times. Over the land part of the Maritime Continent, the precipitation peaks mostly between 2100 and 0300 LST, with several small areas corresponding to the time from 0300 to 0900 LST. This contrasts with the ocean part of the Maritime Continent, where the precipitation peaks mostly at times 0900–1800 LST. LowRes shows a lower maximum precipitation, with a rain deficit over the Indian Ocean compared to TRMM. The maxima are located over the islands and there is also a peak corresponding to the Severe Tropical Storm Jade. The time of the precipitation maximum over the islands is several hours earlier than in TRMM. HiRes reproduces better the maximum precipitation than LowRes, in both the magnitude and the spatial pattern. The precipitation is higher over the islands, as in TRMM. The corresponding LST is closer to TRMM, 2100–0300 LST, with small zones where precipitation peaks at 0300–0900 LST.

The case of 2011 is shown in Fig. 3.18. Here, TRMM gives higher amplitudes of precipitation over the Indian Ocean than in the case of 2009 while the amplitudes over the Maritime Continent are lower. Again, the precipitation peaks

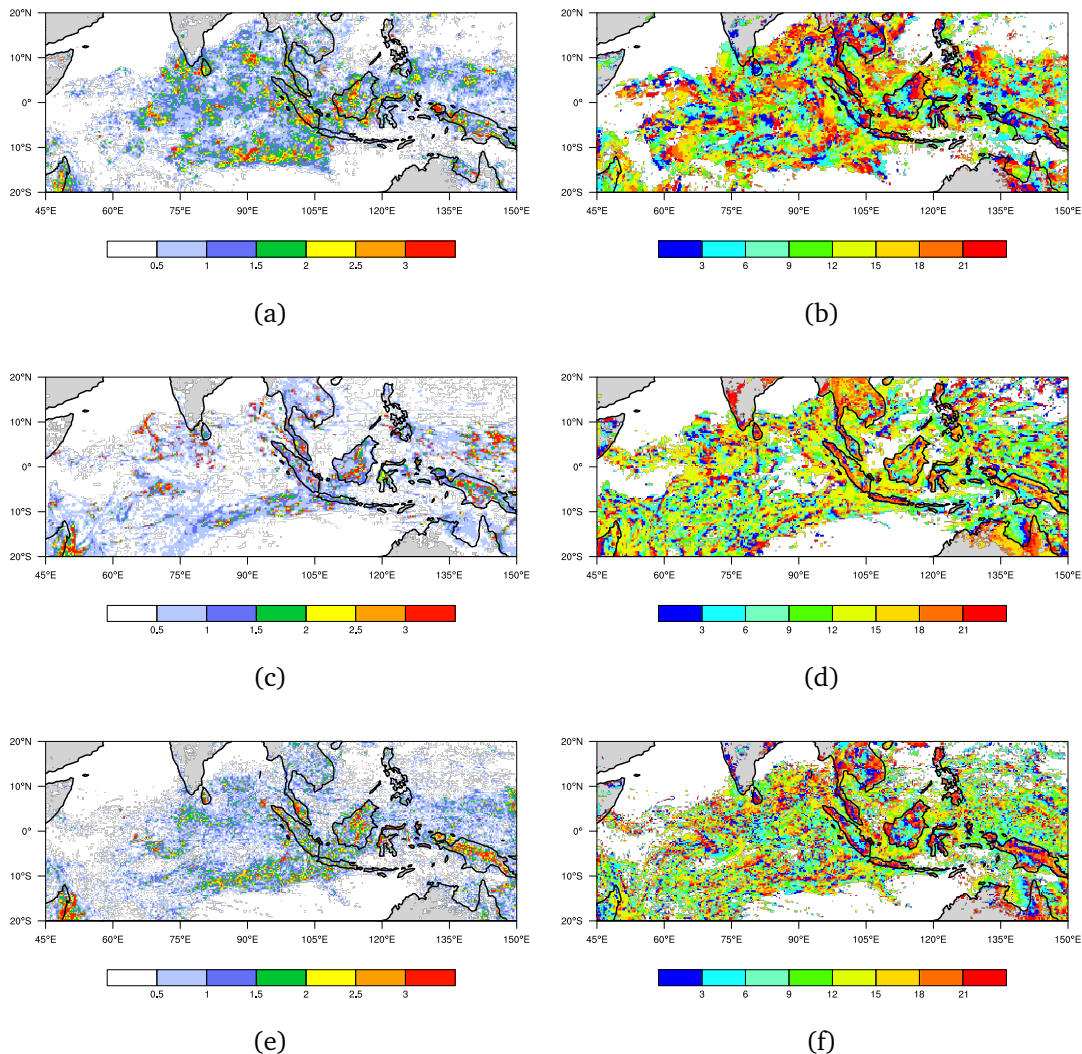


Figure 3.17: Spatial distribution of the daily precipitation maximum (mm; a,c,e) and of its local solar time (b,d,f). Case of 2009. (a,b): TRMM, (c,d): LowRes, (e,f): HiRes. Mean precipitation less than 0.2 mm day^{-1} was not included in the calculation.

mostly at night or early morning (2100–0600 LST) over the land part of the Maritime Continent and at 0900–1800 LST over the ocean part of the Maritime Continent, while the times of maximum over the Indian Ocean do not show any specific pattern. As LowRes exaggerates the path of the Deep Depression ARB 04 along the western coast of the Indian subcontinent, it has a distinct signature

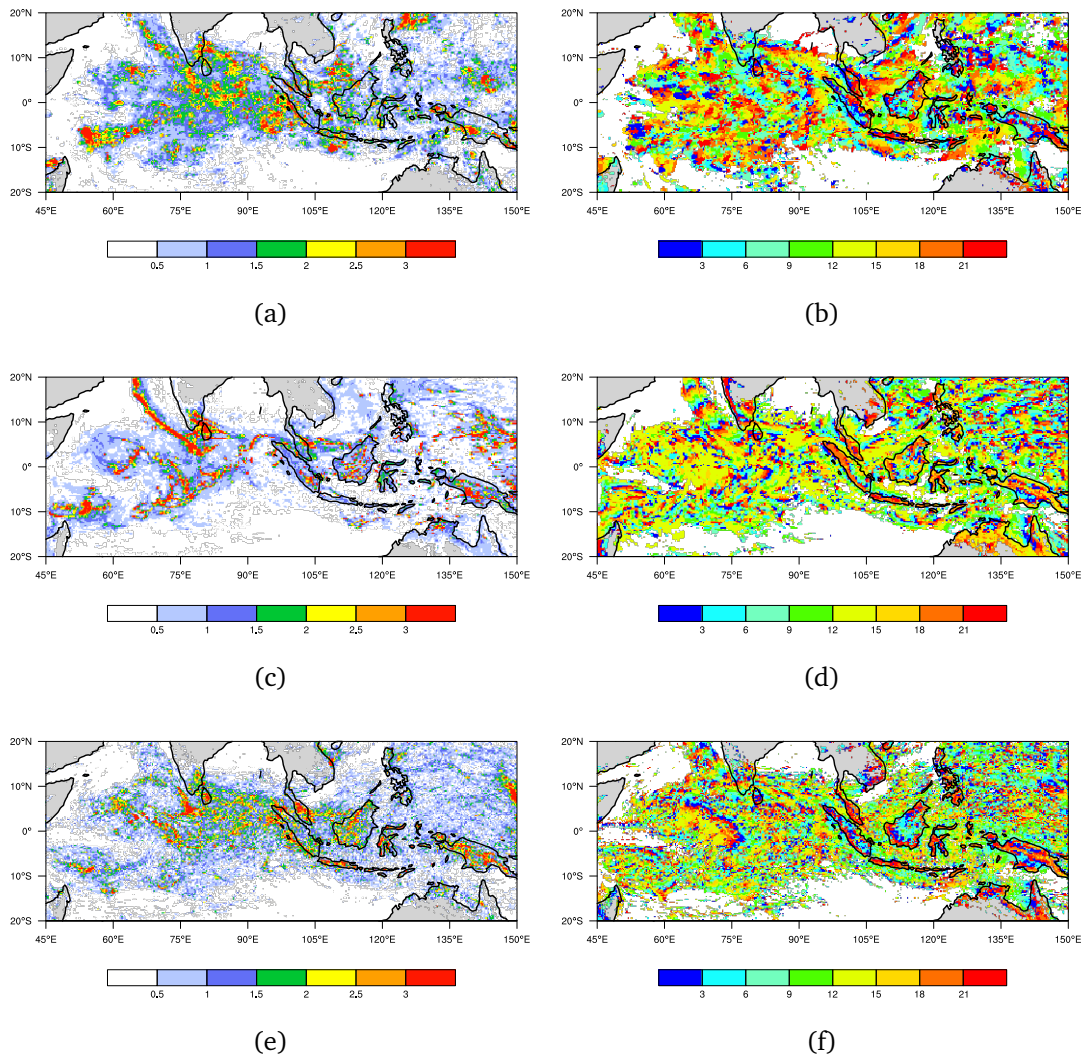


Figure 3.18: Same as in Fig. 3.17, but for the case of 2011.

in the maximum precipitation. There are other “lines” over the Indian Ocean showing the paths of the isolated convective systems, while the weaker amplitudes are not very well reproduced as compared to TRMM. Over the Maritime Continent, the maximum precipitation is located mostly over the islands where it peaks too early compared to TRMM, generally in the afternoon (1500–2100 LST). HiRes shows a spatial pattern similar to TRMM despite the precipitation

being more scattered. The maximum amplitudes are over the Indian Ocean and the land part of the Maritime Continent. The times of the maximum amplitude over the Indian Ocean give a noisy signal except a distinct feature around 60° – 75° E, 3° S– 5° N. This shows the path of a depression or an isolated storm, which has developed around 1200 LST and started propagating eastward, influencing the time of maximum amplitudes in the average diurnal cycle. Over the Maritime Continent, the peak time over the land is at night or early morning (2100–0600 LST) while the peak time over the ocean is several hours earlier.

The case of 2013 is shown in Fig. 3.19. For this case, the maximum precipitation is located on the islands of the Maritime Continent while the precipitation over the Indian Ocean is scattered and weak. The distribution of the peak time is similar to the cases of 2009 and 2011. LowRes and HiRes show a deficit in precipitation over the Indian Ocean, with the absence of precipitation more than 0.5 mm day^{-1} near the equator. The amplitudes of the cyclones are overestimated. Nevertheless, HiRes reproduces better the precipitation over the Maritime Continent, giving higher amplitudes over the islands than LowRes. It shows precipitation over the ocean part of the Maritime Continent while this precipitation is mostly absent in LowRes. The peak times are also better reproduced in HiRes, similarly to the cases of 2009 and 2011.

In summary, HiRes reproduces the spatial locations as well as the time of the maximum amplitudes in the diurnal cycle of precipitation better than LowRes as compared to TRMM. The diurnal cycle is more pronounced over the islands of the Maritime Continent (peaking at night) and there are several maxima located over the Indian Ocean, while the peak time does not have a distinct spatial pattern over the Indian Ocean.

To analyse the difference between the **diurnal cycles over land and ocean**, two subdomains were chosen: (i) 60° – 90° E, 20° S– 20° N, corresponding to the

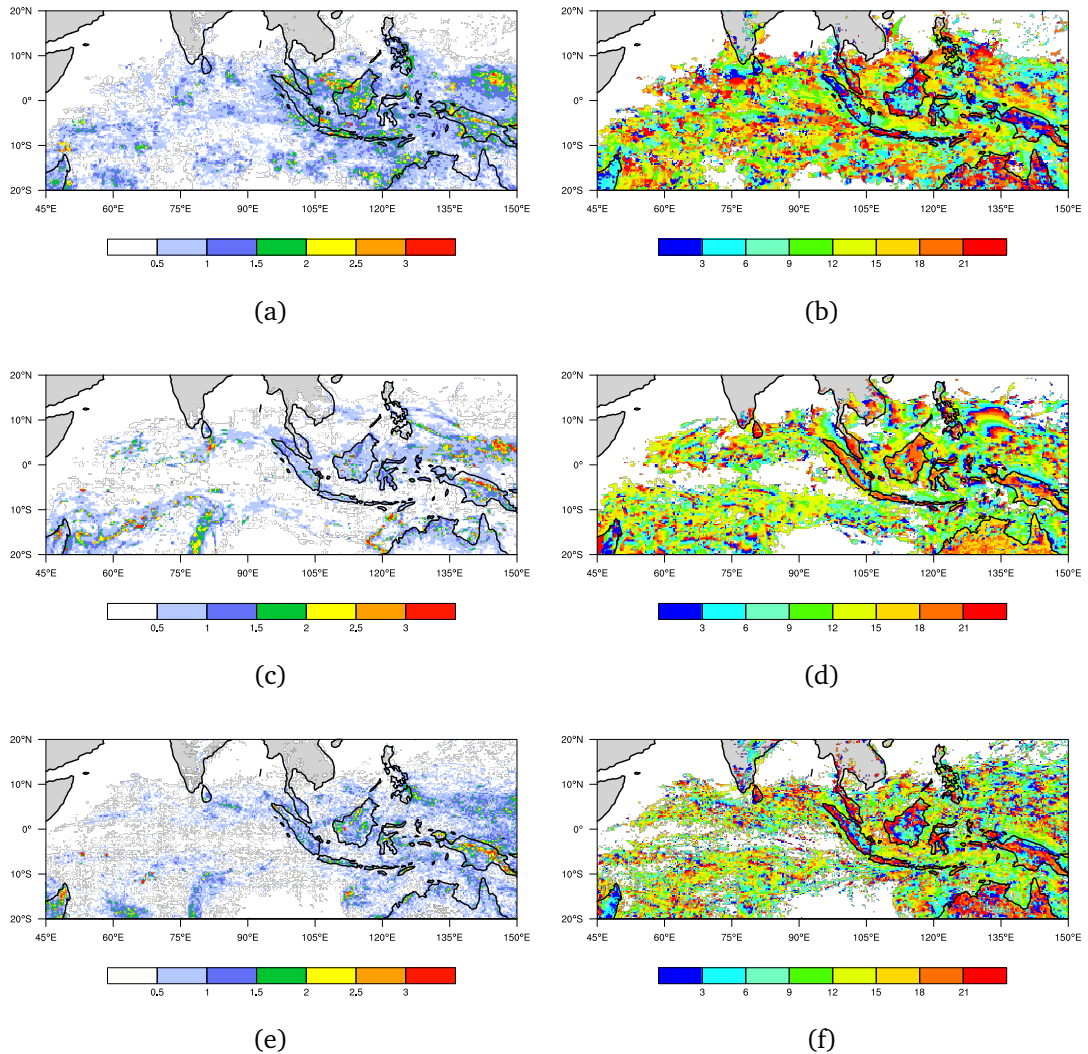


Figure 3.19: Same as in Fig. 3.17, but for the case of 2013.

central Indian Ocean, and (ii) 105°–135°E, 20°S–20°N, corresponding to the central Maritime Continent. For the central Maritime Continent, the diurnal cycle is analysed separately for the land part and for the ocean part. We compare the average diurnal cycle for TRMM, LowRes and HiRes. LST for the first domain is considered as the LST at 75°E and for the second, as the LST at 120°E.

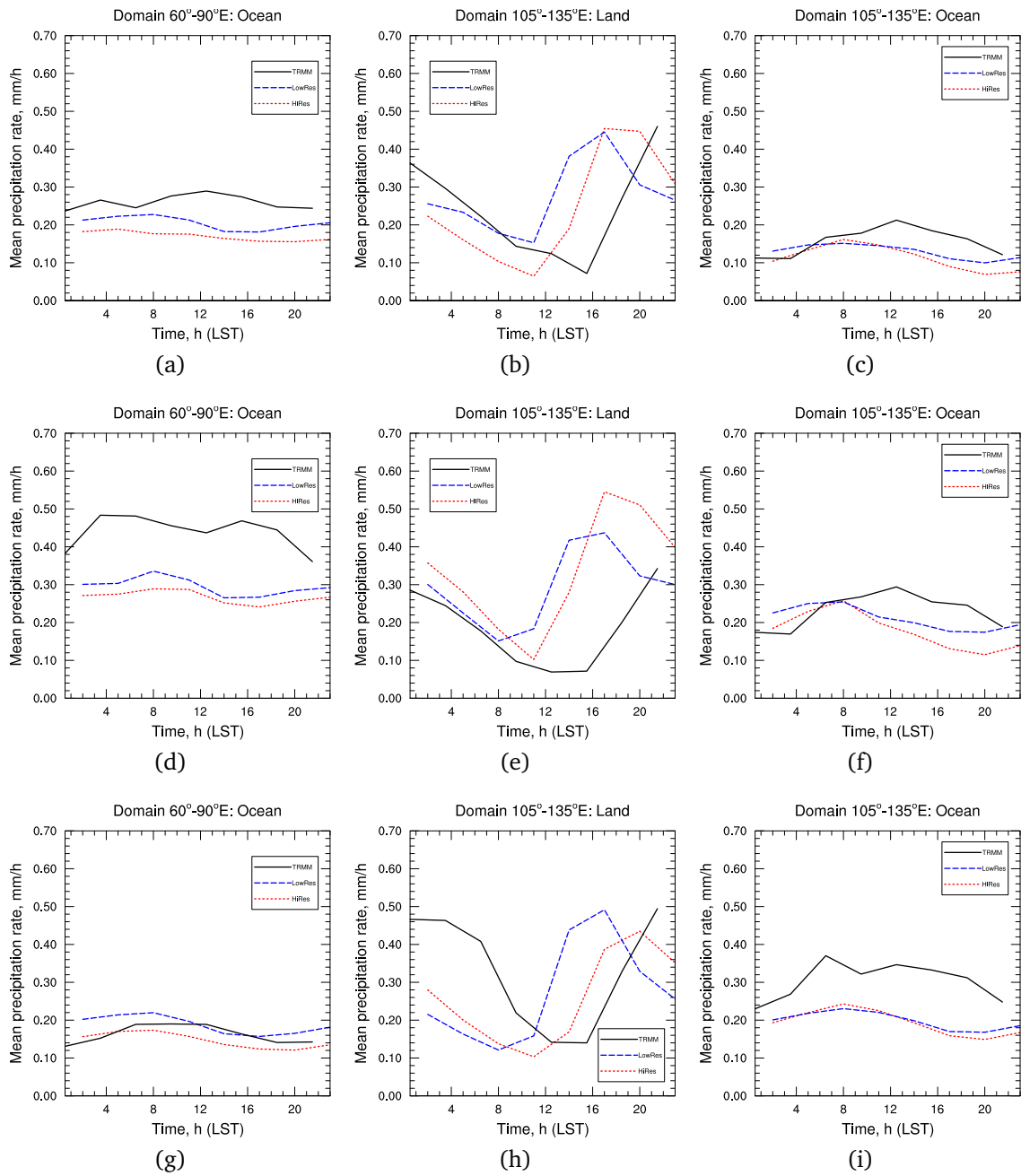


Figure 3.20: Diurnal cycle of precipitation for (a–c) the case of 2009, (d–f) the case of 2011 and (g–i) the case of 2013. It is calculated over (left column) the Indian Ocean, (middle column) the land part and (right column) the ocean of the Maritime Continent.

The diurnal cycle is more pronounced over the land (Fig. 3.20, middle column) than over the ocean (Fig. 3.20, left and right columns). Over the ocean, LowRes and HiRes give generally similar results and the LST corresponding to the maximum and the minimum of the diurnal cycle is also the same or close. The amplitude of the diurnal cycle is well reproduced. There is however a deficit in precipitation as compared to TRMM (more pronounced in HiRes), except the case of 2013 for the Indian Ocean (Fig. 3.20g). The simulated precipitation deficit is the most noticeable for the Indian Ocean in 2011 (Fig. 3.20d) and for the ocean part of the Maritime Continent in 2013 (Fig. 3.20i). Over the land, the amplitude in both HiRes and LowRes is well reproduced for all cases. There is a difference of several hours in the times corresponding to the maximum and the minimum of the daily mean precipitation. HiRes reproduces better than LowRes the time of the minimum in 2011 and 2013, and well reproduces the time of the maximum in 2013. In 2009, in both simulations the LST corresponding to the maximum and the minimum, is around 4 h before TRMM.

3.2.6 Summary

The HiRes simulations in April 2009 and November 2011 are successful in propagating the rain eastward when the zonal wind shows low-level convergence and upper-level divergence. This corresponds to the agreement between the three MJO indices. In contrast, the HiRes simulation in February 2013 fails to reproduce the eastward rain propagation. This event is also characterized by an absence of a propagating zonal wind and a disagreement between the MJO indices.

The spatial distributions of the maximum of precipitation and the corresponding local solar times are better reproduced by HiRes regardless of the MJO

episode. For the average diurnal cycle separately over the Indian Ocean and the land and ocean parts of the Maritime Continent, HiRes gives higher precipitation deficit over the ocean but reproduces better the time of minimum/maximum over the land.

3.3 Sensitivity of the 2011 simulation to the cloud fraction and turbulence parameterizations

The sufficient capability of the model to reproduce the November 2011 event encourages us to make additional sensitivity tests to some parameterizations. The objective is to improve the representation of this event, especially the problem of too dry atmosphere. Due to the long time needed for running a simulation over the selected large domain, only two tests were performed. The first test was performed to study the impact of the cloud parameterization, as the incorrect representation of the cloud cover could influence the radiative exchanges between the surface and the higher levels. The “standard” simulation was performed using a statistical subgrid scale cloud scheme, while the additional simulation was run without any cloud fraction. The second test was on the representation of turbulence, which influences the distribution of the clouds, their life duration and thus, the representation of the convective environment. In this test, the 3D representation of turbulence was used while in the “standard” simulation, the 1D representation of turbulence was chosen.

3.3.1 Impact on the propagation of the precipitation signal

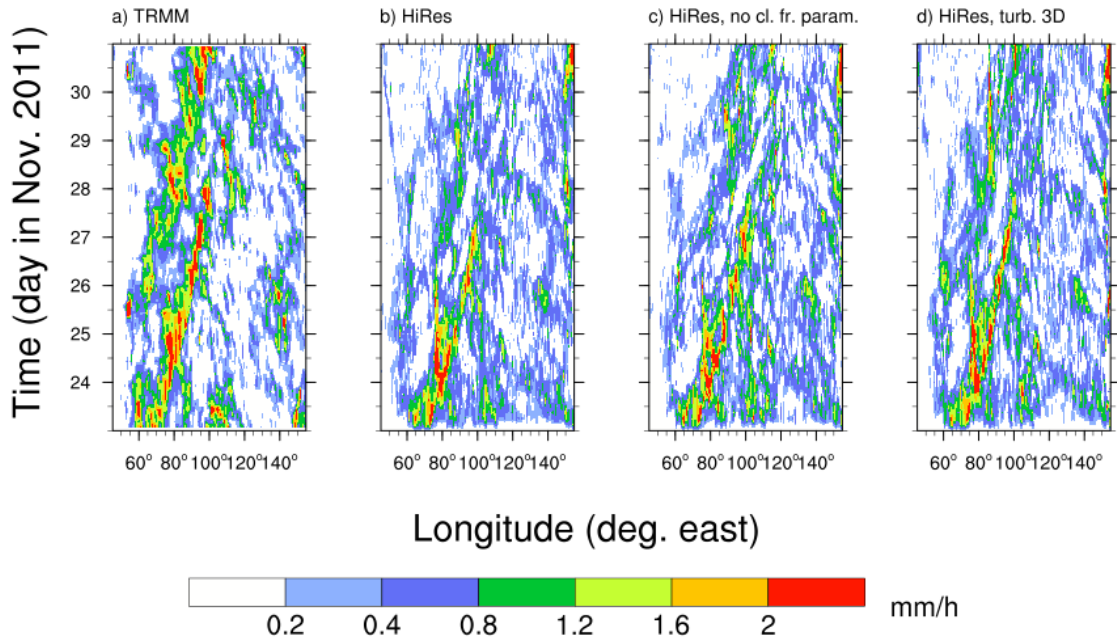


Figure 3.21: Hovmöller diagram of precipitation (mm h^{-1}) averaged between 7.5°S and 7.5°N for the November 2011 event. (a) TRMM, (b) HiRes-2011, (c) HiRes-2011a, (d) HiRes-2011b.

In Fig. 3.21, the precipitation is shown on a Hovmöller diagram for TRMM and three simulations: (i) the “standard” one, or HiRes-2011, (ii) the simulation without the parameterization of the cloud fraction (the “all or nothing” approach), or HiRes-2011a, and (iii) the simulation with 3D turbulence scheme, or HiRes-2011b.

There is no significant difference in the weak precipitation. The most important differences exist in the strong precipitation thus changing the representation of the MJO signal. All the simulations reproduce the first eastward-propagating feature well. In HiRes-2011 this feature however weakens around 120°E , while in HiRes-2011a and HiRes-2011b it propagates further over the Maritime Continent, to 125°E , and has higher amplitude. The second eastward-propagating

feature while well visible in TRMM is weaker for all the simulations, but its amplitude is better reproduced in HiRes-2011a and it has the highest amplitude in HiRes-2011b. In HiRes-2011b, its development around 60°E is well distinct.

3.3.2 Impact on the zonal wind

The impact of the sensitivity tests on the zonal wind is examined. Figure 3.22 shows the time–height diagrams for ECMWF data and three HiRes simulations. Three subdomains close to the equator were chosen for this analysis: central Indian Ocean 60°–80°E, 7.5°S–7.5°N (Figs. 3.22a–d), eastern Indian Ocean 80°–100°E, 7.5°S–7.5°N (Figs. 3.22e–h), and the western Maritime Continent 100°–120°E, 7.5°S–7.5°N (Figs. 3.22i–l).

The ECMWF zonal wind over the central Indian Ocean shows the distinct MJO arrival to this region around 24 November. The wind direction is eastward closer to the surface, and westward in the upper troposphere. The similar structure is seen in the simulations but the low-level wind amplitude is underestimated. The cloud content in the simulations shown by the black contours, is intensified in the active MJO phase (until 26 November in HiRes-2011 and HiRes-2011b, and until 28 November in HiRes-2011a), and reduced in the suppressed MJO phase, after 28 November.

Over the eastern Indian Ocean in the ECMWF data, the upper-level wind changes sign around 1200 UTC 24 November and one more time around 1200 UTC 25 November, indicating the arrival of the active MJO phase. After 1200 UTC 25 November, the upper-level wind amplitude increases. Near the surface, the wind is weak in the beginning, close to zero around 26–28 November, and strengthens after 1200 UTC 28 November. In the simulations, the upper-

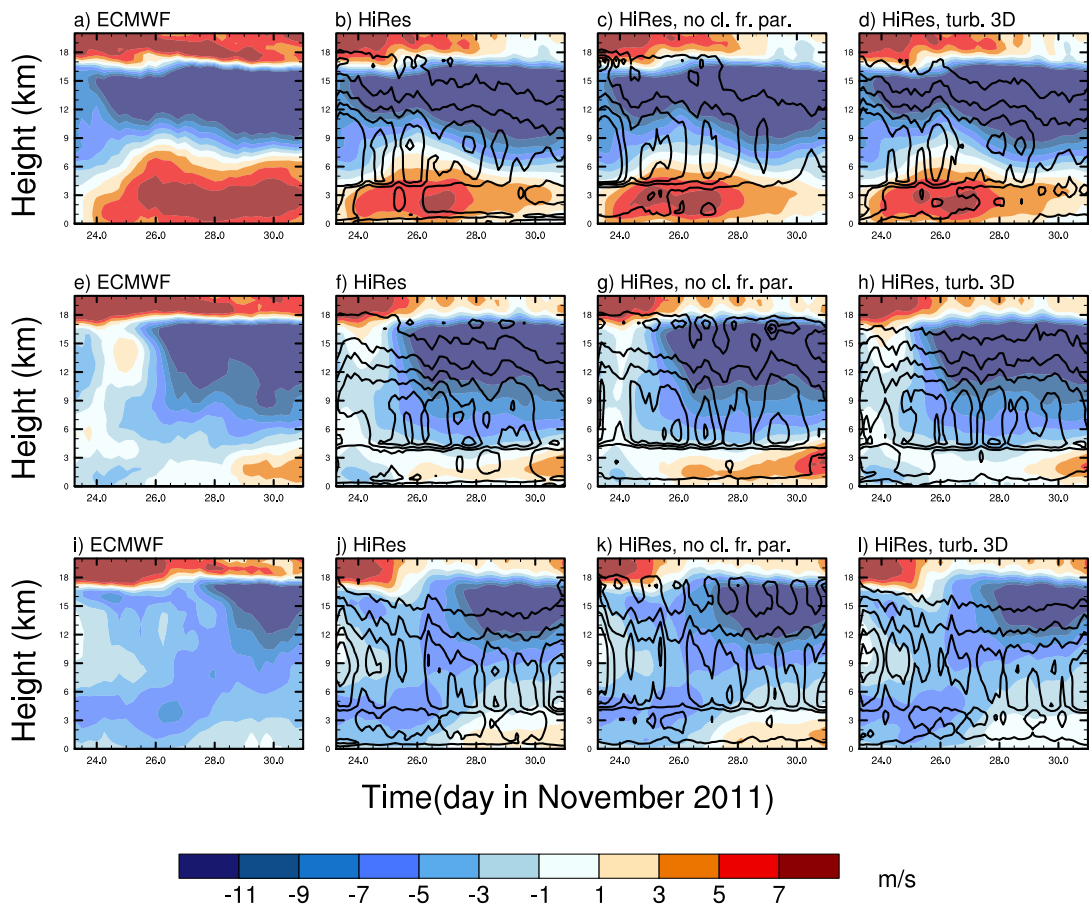


Figure 3.22: Time vs height diagram for the zonal wind averaged between (a)–(d) 60° – 80° E, 7.5° S– 7.5° N, (e)–(h) 80° – 100° E, 7.5° S– 7.5° N, (i)–(l) 100° – 120° E, 7.5° S– 7.5° N, for the November 2011 event. Columns from left to right: ECMWF, HiRes-2011, HiRes-2011a, HiRes-2011b. Contours show the cloud content for HiRes simulations.

level western wind which exists during 1200 UTC 24 November – 1200 UTC 25 November, is not very distinct, the amplitude being too weak. The strong upper-level eastern wind appearing after this, is well simulated. In HiRes-2011 and HiRes-2011a, the low-level wind changes its direction too early, around 26 November, while in HiRes-2011b it happens around the same time as in ECMWF. The cloud content in this region shows diurnal variations and intensifies during the active MJO phase.

Over the western Maritime Continent, the active MJO phase weakens as compared to its intensity over the Indian Ocean. The active MJO phase can be traced in the ECMWF data as the intensification of the upper-level easterly wind around 28 November, while near the surface the wind weakens. In the simulations, the intensification of the upper-level easterly wind is also present. In HiRes-2011 and HiRes-2011a, the westerly wind appears near the surface around 1200 UTC 27 November. In HiRes-2011b, the wind near the surface is weak after 1200 UTC 27 November, thus HiRes-2011b is giving a result closer to the ECMWF analyses. The cloud content shows a pronounced diurnal variability and has the strongest maxima in the beginning and in the end of the simulation, while the maximum corresponding to the arrival of the active MJO phase at the Maritime Continent, is slightly weaker.

Generally, it is possible to conclude that HiRes-2011b improves the simulation of the MJO signal, with HiRes-2011a giving better results than HiRes-2011 over the central Indian Ocean but too strong amplitudes over the eastern Indian Ocean and western Maritime Continent.

3.3.3 Impact on the water vapor and rain

The impact of the sensitivity tests on the vertically-integrated content of water vapor and rain is shown in Fig. 3.23 for the same subdomains. For the central Indian Ocean, the ECMWF water vapor content is nearly constant during the active MJO phase and for some time after its passage (23–27 November). The simulations underestimate the water vapor content, with the HiRes-2011a giving the lowest values and showing strong drying in the end of the simulation. HiRes-2011 curve is located between the HiRes-2011a and HiRes-2011b curves. Despite

too low water vapor values in the middle of the simulation period, HiRes-2011b shows the correct value in the end of the simulation period, on 30 November.

TRMM precipitation shows distinct semi-diurnal variations which are less visible in the simulations. The highest peaks in TRMM appear during the active MJO phase, on 23–24 November. In all simulations, a similar peak is seen at the same time, after the model spinup. With the passage of the MJO, the precipitation decreases. HiRes-2011a has several minima with the lowest precipitation values as compared to the other simulations and TRMM. HiRes-2011b curve stays close to TRMM until 1200 26 November, then decreases during 1200 UTC 26 November – 1200 UTC 30 November while TRMM precipitation values increase, this corresponds to the fact that the second eastward-propagating feature is too weak in the simulations as seen in Fig. 3.21. In the end, all curves converge.

For the eastern Indian Ocean, there is a significant deficit in the water vapor content after 25 November until the end of the simulation period. On 30 November, HiRes-2011b gives higher value as compared to HiRes-2011 and HiRes-2011a. In precipitation, the arrival of the active MJO phase is well noticeable, on 25 November in TRMM and on 24 November in the simulations. The simulated precipitation has lower amplitude as compared to TRMM. This underestimation is the strongest in the end of the simulation period, HiRes-2011b giving the highest values.

For the Maritime Continent, there is again a deficit in the simulated water vapor content. All simulations give close results until 29 November, then they start to slightly differ with HiRes-2011b giving the highest values. The precipitation show the distinct peak in the beginning with the further decrease. The simulations overestimate precipitation during 0000 UTC 24 November – 1200 UTC 27 November, during the suppressed MJO phase. After the arrival of the

active MJO phase, the precipitation is well reproduced. HiRes-2011a gives the values closest to TRMM during the active MJO phase, 1200 UTC 27 November – 0000 UTC 30 November.

In summary, HiRes-2011b allows us to obtain an improved simulation of the water vapor content and precipitation over the Indian Ocean, while there is no significant improvement for the Maritime Continent. HiRes-2011a shows an improvement as compared to HiRes-2011 but for some time periods only. All simulations generally give the precipitation deficit over the Indian Ocean, and show strong drying of the atmosphere in all three subdomains thus underestimating the water vapor content.

3.3.4 Impact on the relative humidity

The impact of the sensitivity tests on the relative humidity is now examined. Figure 3.24 shows the time–height diagrams for ECMWF data and three HiRes simulations for the same subdomains.

For the central Indian Ocean (Figs. 3.24a–d), ECMWF shows the humidifying of the atmosphere during 23–25 November, which corresponds to the active MJO phase. A zone with the relative humidity higher than 80% is seen extending up to 16-km height. With the further MJO propagation, there is drying after 29 November, especially noticeable up to 6-km height. The moistening of the atmosphere is slightly underestimated in the simulations. Nevertheless, high relative humidity is seen around 12–17 km, similar to ECMWF. In HiRes-2011b, around 0000 UTC 24 November and after 28 November the upper-level relative humidity is lower than in HiRes-2011 and HiRes-2011a.

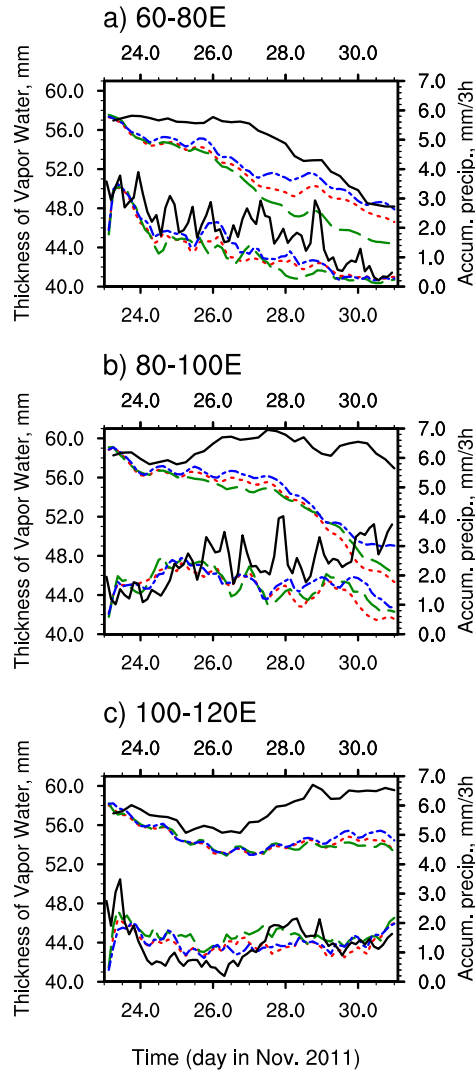


Figure 3.23: Vertically-integrated content of water vapor (in mm, upper part of the plots) and precipitation (in mm/3h, lower part of the plots) averaged in (a) 60° – 80° E, 7.5° S– 7.5° N, (b) 80° – 100° E, 7.5° S– 7.5° N, (c) 100° – 120° E, 7.5° S– 7.5° N, for the November 2011 event. — (black), ECMWF/TRMM; - - - (red), HiRes-2011; -- (green), HiRes-2011a; - - - (blue), HiRes-2011b.

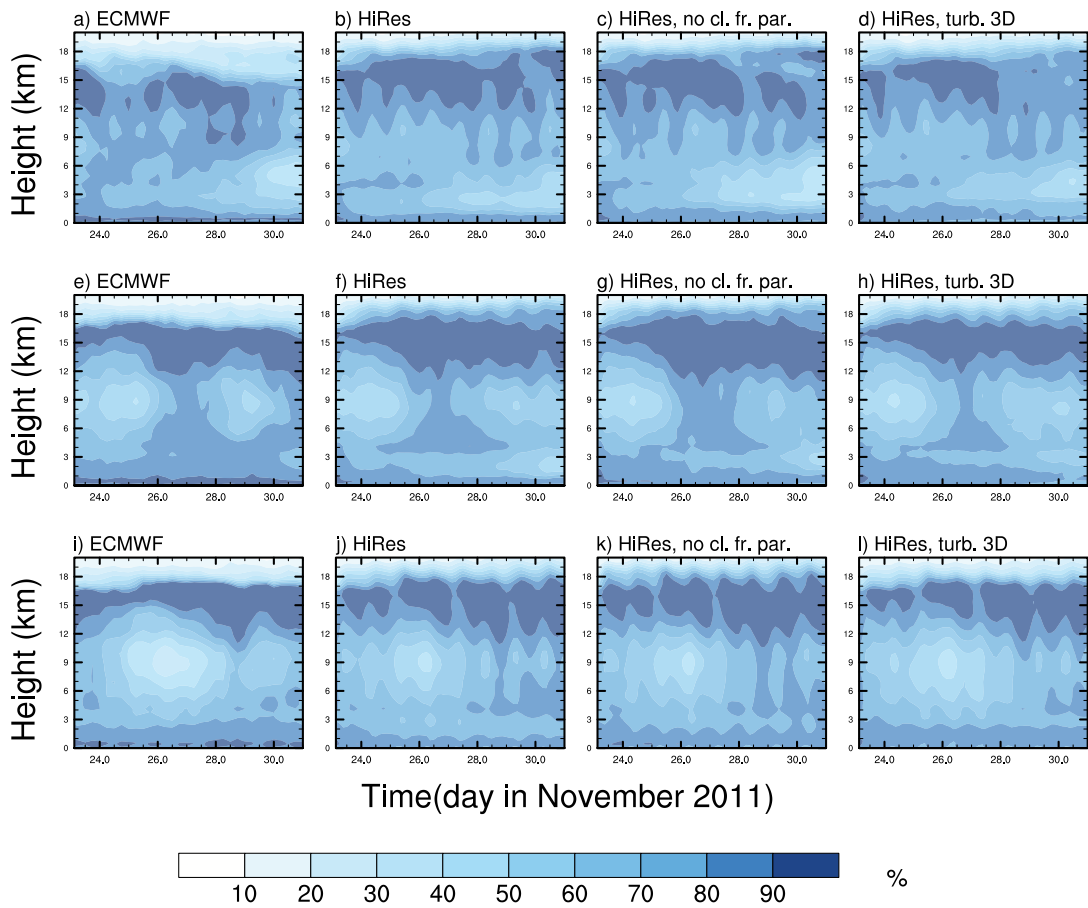


Figure 3.24: Same as in Fig. 3.22, but for the relative humidity.

For the eastern Indian Ocean (Figs. 3.24e–h), the two suppressed MJO phases surrounding the active MJO phase are clearly visible in ECMWF and all simulations. At the upper level, the relative humidity is high, above 80%, this zone is especially thick in HiRes-2011a. In HiRes-2011, a layer of dry air exists at 1–3-km height. It is not present in ECMWF and has less vertical extent in the other simulations.

For the Maritime Continent (Figs. 3.24i–l), the suppressed MJO phase is seen in the middle of the simulation period, around 25–28 November, for all datasets. The active MJO phase is less humid and has less temporal extent than for the Indian Ocean as seen in ECMWF (around 0000 UTC 29 November). The active phase is slightly overestimated in the simulations, especially HiRes-2011 and HiRes-2011a. The diurnal variations are visible, more pronounced for the simulations. The upper-level relative humidity layer is thicker in ECMWF than in the simulations, where it is more influenced by the diurnal cycle.

As we can see, the MJO propagation is well noticeable in the relative humidity, with the maximum during the active phase and the minima during the suppressed phases. The time of the maximum relative humidity corresponds to the time of the arrival of the strong upper-level easterly wind. There is no overall significant improvement in the representation of the relative humidity by changing the model settings to HiRes-2011a or HiRes-2011b. There are local improvements which are region-dependent and they differ for HiRes-2011a and HiRes-2011b.

3.3.5 Summary

Three high-resolution simulations are compared: the “standard” simulation with the parameterized cloud fraction and 1D turbulence scheme (HiRes-2011),

the simulation without the parameterization of the cloud fraction and with 1D turbulence scheme (HiRes-2011a), and the simulation with the parameterized cloud fraction and 3D turbulence scheme (HiRes-2011b). They are all able to reproduce the eastward MJO propagation. HiRes-2011a and HiRes-2011b however show a stronger signal that propagate further over the Maritime Continent. As for the zonal wind, HiRes-2011b shows improvements in the wind amplitude while HiRes-2011a sometimes overestimates it. In all HiRes simulations, there is a strong drying towards the end of the simulation period. This drying is present over the central Indian Ocean in the ECMWF analysis, but absent over the eastern Indian Ocean and the Maritime Continent. Thus, the simulations overestimate the drying of the atmosphere with respect to the ECMWF analysis. HiRes-2011b gives slightly better results than two other simulations. In relative humidity, there is no significant improvement in HiRes-2011a and HiRes-2011b.

In summary, HiRes-2011b allowed to obtain a stronger MJO signal in precipitation (as shown in the Hovmöller diagram) and stronger zonal wind amplitude, even if did not give a significant improvement. Thus, this simulation was chosen to study the atmospheric circulations during the MJO passage over the Indian Ocean and the Maritime Continent.

Chapter 4

Atmospheric overturning during the MJO

Contents

4.1	Introduction	104
4.2	Article: The three atmospheric circulations over the Indian Ocean and the Maritime Continent and their modulation by the passage of the MJO	106
4.3	Discussion	144
4.3.1	Dry air intrusions during the November 2011 MJO event	144
4.3.2	Isentropic diagrams based on ECMWF data	149
4.3.3	The MJO event of April 2009	153

4.1 Introduction

In this chapter, the atmospheric overturning is studied during the MJO passage over the Indian Ocean and the Maritime Continent. An isentropic analysis is applied here, which was developed by Pauluis and Mrowiec (2013) and further generalized by Dauhut et al. (2017). The isentropic analysis has several advantages. One is the elimination of the reversible oscillatory motions due to the time averaging. Another is the reduction of four spatiotemporal coordinates into two, describing the large-scale atmospheric circulations in a phase space. In the isentropic analysis, a vertical coordinate (which here is chosen as z , the height above the ground level) and an isentropic coordinate, conserved during reversible motions (which here is chosen as θ_e , the equivalent potential temperature), are used. The advantage of θ_e consists in its conservation in reversible moist adiabatic processes such as gravity waves or transitions between water vapor and liquid water. (However, during mixing or radiative processes as well as during phase changes involving ice i.e. melting, freezing, sublimation, and deposition, the equivalent potential temperature is no longer conserved.) The use of θ_e allows to separate the downdrafts consisting of cold dry air masses from the updrafts with warm moist air masses. It can be seen on isentropic diagrams such as those shown in Figs. 3d–f of the following article, where the vertical mass flux is represented in the phase space (z, θ_e) . It is visible that the air parcels with larger θ_e are rising while the particles with lower θ_e are descending. (The detailed description can be found in the following article.)

Chen et al. (2018) applied the isentropic analysis to the MJO episode of November 2011 in a convection-permitting simulation with the horizontal grid spacing of 9 km. Their domain of study (20°S–20°N, 48°E–200°E) was divided

into 120 smaller subdomains of the size $450 \times 450 \text{ km}^2$. The vertical mass flux in the atmospheric overturning was further studied by decomposing into different spatial scales: (i) convective scale (all scales less than 450 km), (ii) basin scale (a basinwide ascent), (iii) meridional scale (a zonally symmetric meridional overturning), (iv) regional scale (zonal asymmetries on scales larger than 450 km). Chen et al. (2018) show that over the Indian Ocean, the convective vertical mass transport (corresponding to scales less than 450 km) dominates the mass transport on other scales and increases in the low troposphere before the passage of the MJO. During the passage of the active MJO phase, the vertical mass transport intensifies on all scales.

In the article that follows, the MJO influence on the atmospheric overturning is studied using the isentropic analysis but the main interest is given to the large-scale atmospheric circulations over the Indian Ocean as well as over the Maritime Continent, during the episode of 23–30 November 2011. The isentropic streamfunction shows three key circulations. The first circulation is a tropospheric circulation extending from the surface to around 14-km altitude, and its magnitude increases during the active phase of the MJO. The second circulation is located between 14- and 18-km altitudes and represents overshoots within the tropical tropopause layer, which becomes stronger during the active phase of the MJO. The third circulation found in the low troposphere was unexpected and is characterized by the rising of air masses with low θ_e . Its intensity and vertical extension also vary with the MJO passage. It was obtained that this circulation corresponds to the intrusion of the dry air masses from the subtropics into the equatorial band.

4.2 Article: The three atmospheric circulations over the Indian Ocean and the Maritime Continent and their modulation by the passage of the MJO

Article under review in *Journal of the Atmospheric Sciences* (revised version of 27 November 2018).

1 **The three atmospheric circulations over the Indian Ocean and the Maritime**

2 **Continent and their modulation by the passage of the MJO**

3 Daria Kuznetsova*, Thibaut Dauhut, and Jean-Pierre Chaboureau

4 *Laboratoire d'Aérodynamique, Université de Toulouse, CNRS, UPS, Toulouse, France*

5 **Corresponding author address:* Daria Kuznetsova, Laboratoire d'Aérodynamique, Observatoire Midi-

6 Pyrénées, 14 Ave. Edouard Belin, 31400 Toulouse, France.

7 E-mail: daria.kuznetsova.aero.obs.mip@gmail.com

ABSTRACT

8 The passage of the Madden–Julian oscillation (MJO) over the Indian
9 Ocean and the Maritime Continent is investigated during the episode of 23–
10 30 November 2011. A Meso-NH convection-permitting simulation with a
11 horizontal grid spacing of 4 km is examined. The simulation reproduces the
12 MJO signal correctly, showing the eastward propagation of the primary rain
13 activity. The atmospheric overturning is analyzed using the isentropic method,
14 which separates the ascending air with high equivalent potential temperature
15 from the subsiding air with low equivalent potential temperature. Three key
16 circulations are found. The two first circulations are a tropospheric deep cir-
17 culation spanning from the surface to an altitude of 14 km and an overshoot
18 circulation within the tropical tropopause layer. As expected for circulations
19 associated with deep convection, their intensities, as well as their diabatic ten-
20 dencies, increase during the active phase of the MJO, while their entrainment
21 rates decrease. The third circulation is characterized by a rising of air with
22 low equivalent potential temperature in the lower free troposphere. The in-
23 tensity of the circulation, as well as its depth, varies with the MJO activity.
24 During the suppressed phase, this circulation is associated with a dry air in-
25 trusion from the subtropical region into the tropical band and shows a strong
26 drying of the lower to middle troposphere.

1. Introduction

The MJO, or Madden–Julian oscillation (Madden and Julian 1971, 1972), is a large-scale phenomenon (with a zonal extent of $\sim 12,000$ – $20,000$ km) and the dominant component of the intraseasonal variability in the tropical atmosphere. It is represented by coupled patterns in atmospheric circulation and convection and is accompanied by a distinct signal in many other variables (Zhang 2005). The MJO consists of a zone of widespread, deep convection and enhanced precipitation totals, surrounded on the east and west by zones of relatively weak convection and less precipitation. The MJO propagates eastward around the globe with an intraseasonal period of approximately 30–90 days. Inside the MJO envelope, small-scale convective systems interact with mesoscale convective systems (MCSs) and superclusters, giving the convection a multi-scale structure (Nakazawa 1988; Moncrieff et al. 2012). The convective signals of the MJO are generally most visible over the Indian and western Pacific oceans (Zhang 2005), where the MJO propagates with an average speed of 5 m s^{-1} .

An extensive observational field campaign, the Cooperative Indian Ocean Experiment on Intraseasonal Variability (CINDY)/Dynamics of the Madden–Julian Oscillation (DYNAMO) (Yoneyama et al. 2013; Zhang et al. 2013; Zhang and Yoneyama 2017), was conducted during the period of 2011–2012. This campaign allowed the different processes that contribute to the evolution of the MJO to be observed. Kerns and Chen (2014) and Chen et al. (2016) noted that, during the episode of November 2011 (MJO-II), several large-scale dry air intrusions from the subtropics into the tropical Indian Ocean were observed. They proposed that these dry air intrusions contributed to the eastward propagation of the MJO active phase and the development of the suppressed phase in the following way. The convection located in the Intertropical Convergence Zone (ITCZ) was forced toward the equator by a dry air intrusion, creating favorable conditions

50 for the initiation of the MJO. The following dry air intrusions participated in the suppression of the
51 convection to the west of the MJO active phase. These dry air intrusions are likely to be advected
52 by Rossby wave gyres and are thus consistent with the response to equatorial heating as in Gill
53 (1980).

54 This paper further describes the convective evolution of the atmosphere during the passage of
55 the MJO and the development of the MJO suppressed phase. To have a multi-scale description
56 of convection, we performed a convection-permitting simulation over a vast domain consisting of
57 the Indian Ocean and the Maritime Continent. A specific question addressed here is whether the
58 dry intrusions have an imprint on the atmosphere overturning. Thus, the same period of 23–30
59 November 2011 of Chen et al. (2016) was chosen to analyze the transition from the active phase to
60 the suppressed phase over the Indian Ocean and the arrival of the active phase over the Maritime
61 Continent.

62 To study the large-scale atmospheric circulations, an isentropic analysis is applied. This method
63 was first described by Pauluis and Mrowiec (2013) and allows cold, dry sinking air masses to be
64 separated from warm, moist rising air masses by grouping air particles with similar thermody-
65 namic properties. In addition, reversible motions are excluded via time averaging. This method
66 has been successfully applied in a number of numerical studies, such as analyses of a very deep
67 convective system that hydrates the stratosphere (Dauhut et al. 2017) and the October 2011 MJO
68 event observed during the CINDY/DYNAMO campaign (Chen et al. 2018). In the latter study,
69 the tropospheric overturning up to 16-km height was investigated by decomposition into multiple
70 scales. It was found to be largest at the convective scale (less than 450 km) and to be increasing
71 with the active phase of the MJO. In our paper, an isentropic analysis is applied to the Novem-
72 ber 2011 MJO event characterized by dry intrusions and using a convection-permitting simulation
73 performed at higher resolution. This allows us to investigate the atmospheric overturning up to

74 18-km height with additional features. It is shown to consist of three components, or circulations
75 in an isentropic diagram: a tropospheric circulation similar to the one found by Chen et al. (2018),
76 a smaller circulation corresponding to dry air intrusions, and an overshoot circulation similar to
77 the one obtained in the study of Dauhut et al. (2017). These circulations together with the diabatic
78 tendencies and the entrainment rates are contrasted between the active and suppressed phases of
79 the MJO, as well as between the Indian Ocean and the Maritime Continent.

80 Section 2 describes the model and the methodology. Section 3 analyzes the differences in the
81 convective activity with the passage of the MJO. Section 4 discusses the signature of dry air in-
82 trusions during the MJO propagation as seen in the isentropic diagrams. Section 5 presents the
83 conclusions.

84 **2. Data and methods**

85 *a. Meso-NH high-resolution simulation*

86 The simulation is run using the atmospheric non-hydrostatic regional model Meso-NH (Lafore
87 et al. 1998; Lac et al. 2018), version 5-1-3, over the region of 26.7°S – 26.7°N and 44.6° – 155.4°E to
88 include the Indian Ocean and the Maritime Continent (Fig. 1). This large domain is chosen in order
89 to describe the large-scale variability induced by the passage of the MJO. For the analysis applied
90 here, two subdomains are considered focusing on the Indian Ocean (7.5°S – 7.5°N , 60° – 80°E) and
91 the Maritime Continent (7.5°S – 7.5°N , 100° – 120°E). The 8-day period of 23–30 November 2011
92 is simulated. The simulation is performed with a horizontal grid spacing of 4 km. A total of
93 72 vertical levels are used following the surface elevation with a grid spacing of 60 m near the
94 surface and 600 m at the top of the model. The top of the model is set to 30 km with the upper
95 3 km being a sponge layer to damp any gravity waves generated by convection. Therefore, a

96 domain of $1538 \times 3074 \times 72$ (~ 340 million) grid points is considered. It was possible to run this
97 high-resolution simulation on a very large domain due to the parallel computing capability of the
98 Meso-NH model (Pantillon et al. 2011).

99 The following parameterizations employed in the model: the Surface Externalisée (SURFEX)
100 scheme for the surface fluxes (Masson et al. 2013), the microphysical scheme ICE3 (Pinty and
101 Jabouille 1998) for the mixed-phase clouds containing five hydrometeor types (cloud water, rain,
102 snow, graupel, and ice), a subgrid statistical cloud scheme (Chaboureau and Bechtold 2005), and
103 a subgrid shallow convection parameterization (Pergaud et al. 2009). The radiative schemes used
104 were the Rapid Radiative Transfer Model (Mlawer et al. 1997) for longwave radiation and the
105 two-stream formulation (Fouquart and Bonnel 1986) for shortwave radiation. The turbulence is
106 described using the 1.5-order closure scheme of Cuxart et al. (2000). This scheme was set in our
107 simulation in 3D mode with the mixing length of Deardorff (1980) to obtain a better representa-
108 tion of the cloud organization and their lifetime duration, as shown in Machado and Chaboureau
109 (2015).

110 The model is initialized at 0000 UTC 23 November 2011. The initial and boundary condi-
111 tions are provided by the 6-hourly operational analyses of the European Centre for Medium-range
112 Weather Forecasts (ECMWF). No large-scale forcing is applied. The sea surface temperature was
113 set using the values provided by the ECMWF analyses at the initial time. To assess the simulated
114 rain, the TRMM 3B42 precipitation product (Huffman et al. 2007) with 3-hour temporal resolution
115 and a spatial resolution of $0.25^\circ \times 0.25^\circ$ is used.

116 *b. Isentropic analysis*

117 An isentropic analysis is applied to describe the air mass overturning at the regional scale, elimi-
118 nating any reversible oscillatory motions. For details, the reader is referred to Pauluis and Mrowiec

119 (2013) and Dauhut et al. (2017). In this method, the atmospheric circulations are described using a
120 vertical coordinate and an isentropic coordinate (conserved during the reversible motions), which
121 allows the air masses to be regrouped and reduces the four spatiotemporal coordinates to two. The
122 dynamic and thermodynamic properties of the circulations are then investigated. As the vertical
123 coordinate, we use the height above the ground z , while the isentropic coordinate is the equivalent
124 potential temperature θ_e . The equivalent potential temperature was chosen as the isentropic
125 coordinate because it is conserved in reversible moist adiabatic processes (e.g., gravity waves and
126 transitions between water vapor and liquid water). However, during mixing, radiative processes,
127 or phase changes involving ice, the equivalent potential temperature is no longer conserved. The
128 equivalent potential temperature is defined by the formula of Emanuel (1994):

$$\theta_e = T \left(\frac{p_0}{p} \right)^{R_d/C_p} \exp \left(\frac{L_v r_v}{C_p T} \right) H^{-R_v r_v / C_p}. \quad (1)$$

129 Here, T is the temperature, p_0 is the reference pressure of 1000 hPa, and p is the absolute pressure.
130 R_d and R_v are the ideal gas constants for dry air and water vapor, respectively. $C_p = C_{pd} + r_t C_l$ is
131 the specific heat at constant pressure of moist air, where C_{pd} and C_l represent the specific heat of
132 dry air and liquid water, respectively, and r_t is the mixing ratio of vapor and liquid water. L_v is the
133 latent heat of vaporization, r_v is the mixing ratio of the vapor, and H is the relative humidity.

134 The coordinate transformation is performed in the following manner:

$$\langle f \rangle(\theta_{e0}, z_0) = \frac{1}{PL_x L_y} \int_0^P \int_0^{L_y} \int_0^{L_x} f(x, y, z_0, t) \delta[\theta_{e0} - \theta_e(x, y, z_0, t)] dx dy dt, \quad (2)$$

135 where the units of $\langle f \rangle$ are the units of f per kelvin. δ denotes the Dirac function, approximated
136 numerically by $1/\Delta\theta_{e0}$ over $[\theta_{e0} - \Delta\theta_{e0}/2, \theta_{e0} + \Delta\theta_{e0}/2]$ with $\Delta\theta_{e0} = 1$ K.

137 An important component of the isentropic analysis is the isentropic streamfunction Ψ . It is
138 calculated as the vertical mass flux ρw (where ρ is the density and w is the vertical velocity) from

139 0 to θ_{e0} at each level z_0 :

$$\Psi(\theta_{e0}, z_0) = \int_0^{\theta_{e0}} \langle \rho w \rangle(\theta_e, z_0) d\theta_e. \quad (3)$$

140 This represents the net mass flux at the level z of the air parcels having an equivalent potential
141 temperature less than or equal to θ_{e0} . From the isentropic streamfunction, it is possible to visualize
142 the isentropic streamlines. They can be described as the averaged paths of air parcels with the
143 same (θ_{e0}, z_0) coordinates and correspond to the Lagrangian trajectories followed by those parcels,
144 similar to the streamlines of an unsteady flow.

145 **3. Evolution of the convective activity during the passage of the MJO**

146 *a. MJO signal in the precipitation and an assessment of the model*

147 To assess the quality of the simulation, a Hovmöller diagram for the precipitation averaged in
148 the equatorial band of 7.5°S – 7.5°N is shown (Fig. 2). The longitude range corresponds to the
149 entire simulation domain. In TRMM, the MJO signal showing the eastward propagation of the
150 active phase over the Indian Ocean and the Maritime Continent is clearly visible (Fig. 2a). It
151 consists of two large-scale eastward-propagating features separated by a break of 1–2 days. As
152 noted by Kerns and Chen (2014), the dry air intrusions contribute to this break in the precipitation
153 during the active MJO phase. The two east-propagating features look like the Kelvin waves (KWs)
154 identified by DePasquale et al. (2014). However, their velocity about 8.5 m s^{-1} smaller than the
155 typical values of KWs does not allow to identify them as KWs unambiguously.

156 At 0000 UTC 23 November 2011, the first large-scale eastward-propagating feature character-
157 izing the active MJO phase was located over the Indian Ocean and it arrives over the Maritime
158 Continent around 2100 UTC 27 November 2011. The second large-scale eastward-propagating
159 feature appears over the Indian Ocean around 1200 UTC 25 November 2011, and reaches the

160 Maritime Continent around 1500 UTC 30 November 2011. The MJO signal is well reproduced by
161 the simulation (Fig. 2b). The first large-scale eastward-propagating feature appears over the Indian
162 Ocean at the same time as in TRMM and arrives over the Maritime Continent around 0000 UTC
163 28 November 2011. The second large-scale eastward-propagating feature appears over the Indian
164 Ocean at the same time as in TRMM and arrives over the Maritime Continent at the end of the sim-
165 ulation. This feature is weaker than the first one, as well as the corresponding feature in TRMM,
166 but is still visible. The maximum rainfall in both TRMM and the simulation exceeds 2 mm h^{-1} .
167 Nevertheless, the simulation gives an excess of weak precipitation, including during time periods
168 when TRMM does not show any precipitation. This might be due to systematic errors in simu-
169 lating very low rates of precipitation or due to the fact that the TRMM product is not sensitive to
170 weak precipitation.

171 In the following, three different periods during the MJO propagation are compared: Period 1:
172 1800 UTC 23 November – 0000 UTC 24 November, Period 2: 1800 UTC 27 November – 0000
173 UTC 28 November, and Period 3: 1800 UTC 30 November – 0000 UTC 1 December. These
174 periods are indicated in Fig. 2 by dashed horizontal lines, while the dashed vertical lines show the
175 longitudinal limits for the subdomains chosen for the analyses. For the Indian Ocean, Period 1
176 corresponds to the passage of the active phase, Period 2 corresponds to the transition between
177 the active phase and the suppressed phase (hereafter the “intermediate phase”), and Period 3 cor-
178 responds to the suppressed phase. For the Maritime Continent, Period 1 occurs during the sup-
179 pressed period between the October and November MJO events, Period 2 is just before the active
180 phase, although convection is still suppressed, and Period 3 is after the beginning of the active
181 phase.

182 *b. MJO propagation over the Indian Ocean and the Maritime Continent*

183 The probability distribution function (PDF), the isentropic vertical mass flux, and the isentropic
184 streamfunction for the Indian Ocean (Fig. 3) and for the Maritime Continent (Fig. 4) are shown
185 for Periods 1, 2, and 3. The thick black lines in the figures correspond to the average θ_e profile
186 during the corresponding time period. This profile will be denoted hereafter as $\bar{\theta}_e$.

187 The PDF corresponds to the frequency of each θ_e bin at each z level and shows that the majority
188 of the points have values of θ_e close to the average profile (Figs. 3a–c). The average profile changes
189 with time; its minimum stays at $z \simeq 3$ km but decreases in value from $\theta_e \simeq 335$ K during the active
190 phase (Period 1), to $\theta_e \simeq 330$ K during the intermediate phase (Period 2), and to $\theta_e \simeq 327$ K during
191 the suppressed phase (Period 3). As is shown in Section 4, this decrease is due to the drying of
192 the air in the lower to middle troposphere. The air parcels with larger θ_e , i.e., the parcels with
193 θ_e exceeding the average value by several K, correspond to PDF values less than 2%. Together,
194 they account for less than 6% of the total at every z level for all three phases. In the active
195 phase, air parcels having $\theta_e \leq 330$ K account for less than 14.6% of the total at every z level.
196 With the decrease in $\bar{\theta}_e$ with time, the percentage of these low θ_e points increases up to 47.9% in
197 the intermediate phase and 63.8% in the suppressed phase. This feature is especially noticeable
198 between $z \simeq 3$ km and $z \simeq 6$ km.

199 The vertical mass flux consists of two main parts in the troposphere (Figs. 3d–f). The first
200 part corresponds to upward motions with θ_e higher than $\bar{\theta}_e$, and the second part corresponds to
201 downward motions at low θ_e (generally lower than $\bar{\theta}_e$, including a small zone with $\theta_e > \bar{\theta}_e$).
202 Above 14–15 km, an upward motion is observed with $\theta_e < \bar{\theta}_e$ and a downward motion is seen
203 with $\theta_e > \bar{\theta}_e$. The rising motion of air parcels with $\theta_e < \bar{\theta}_e$ is a signature of overshooting into the
204 stratosphere (Dauhut et al. 2017). The amplitudes of the tropospheric vertical mass flux and the

overshoot are larger during the active phase than during the intermediate and suppressed phases. The rising air parcels are fewer in number than the descending ones, according to Figs. 3a–c. During the active and intermediate phases, small zones with low θ_e and upward motion appear, intensifying during the suppressed phase. This intensification also corresponds to an increase in the percentage of low θ_e air parcels for z levels between 3 and 6 km, as shown previously.

The streamfunction consists of three key circulations (Figs. 3g–i). One circulation is a large-scale tropospheric circulation spanning from the surface to an altitude of 14–15 km (negative Ψ values), where the rising air parcels have high θ_e values up to 352 K. The air masses with high θ_e are ascending, while the air masses with lower θ_e are descending. The intensity of this circulation is greatest at 4 km. The second circulation is an overshoot circulation, with positive Ψ values in the tropical tropopause layer, extending from $z \simeq 13$ –14 km to above 17 km. These first two circulations have a larger amplitude and vertical extent during the active phase of the MJO. The third circulation with positive Ψ values at low θ_e appears during the active and intermediate phases and intensifies during the suppressed phase. This circulation corresponds to the small zone with an upward motion (Figs. 3d–f) described previously and extends from $z \simeq 600$ m to $z \simeq 7$ km during the suppressed phase. It will be shown later that this circulation corresponds to dry air advected from the subtropics.

For the Maritime Continent, the PDF points are concentrated along the average profile (Figs. 4a–c), as in the case of the Indian Ocean. Below a height of 9 km, most of the air parcels (with a probability of more than 5%) have $|\theta_e - \bar{\theta}_e| < 10$ K, while at greater heights most of the air parcels have $|\theta_e - \bar{\theta}_e| < 5$ K. Large θ_e air parcels, i.e., the parcels with θ_e exceeding the average value by several K, correspond to PDF values of less than 2% at every point and together account for less than 3.4% at every z level during the entire simulation period. Before the arrival of the suppressed phase (during Period 1) there are no points with $\theta_e < 325$ K. During the suppressed phase (Period

229 2), the lowest θ_e value is 320 K and this value decreases further to approximately 317 K at the
230 time of the arrival of the active phase (Period 3). During the suppressed phase and just before the
231 arrival of the active phase (Period 2), the percentage of air parcels with low θ_e (less than 327 K)
232 does not exceed 4.5% at any z level. During the active phase, the frequency of air masses with
233 $\theta_e < \bar{\theta}_e$ increases. The average profile of θ_e does not change with the passage of the MJO, unlike
234 in the case of the Indian Ocean.

235 The vertical mass flux (Figs. 4d–f) for $z < 13$ –14 km consists of a zone with higher θ_e charac-
236 terized by rising air and a zone with lower θ_e corresponding to descending air. The descending
237 air parcels are located close to the average profile and, as shown previously, represent a higher
238 percentage than that of the rising air parcels. For $z > 14$ km, the air with $\theta_e < \bar{\theta}_e$ is rising while the
239 air with larger θ_e is descending. This corresponds to an overshoot circulation, as in the case of the
240 Indian Ocean. There are a few low θ_e zones with rising motion on average near $z \simeq 2$ –5 km during
241 Periods 1 and 2. However, their intensity is weak and their corresponding percentage is less than
242 1%. An intensification in the large-scale rising and descending motions is visible during the active
243 MJO phase, and the weakest amplitude corresponds to the suppressed MJO phase.

244 In all the phases, the streamfunction (Figs. 4g–i) consists of a large-scale tropospheric circu-
245 lation and an overshoot circulation. The third circulation, similar to that identified over the In-
246 dian Ocean, appears prior to the passage of the suppressed phase of the MJO and remains during
247 the suppressed phase but with much weaker intensity. Unlike the streamfunction for the Indian
248 Ocean (Figs. 3g–i), the intensities of the large-scale circulation and the overshoot circulation do
249 not change significantly over the Maritime Continent during the passage of the MJO.

250 *c. Diabatic tendencies and entrainment*

251 To further continue this analysis and to better understand the large-scale thermodynamical prop-
252 erties of the system, the diabatic tendency is calculated. The mass-weighted diabatic tendency
253 $\langle \rho \dot{\theta}_e \rangle$ can be calculated as the vertical derivative of the streamfunction in a domain with periodic
254 boundary conditions for an atmosphere in statistical radiative–convective equilibrium (Pauluis and
255 Mrowiec 2013). Its computation can be further generalized for any boundary conditions and time
256 evolution as described by Dauhut et al. (2017), allowing the diabatic tendency to be calculated in
257 our study.

258 For the Indian Ocean, the diabatic tendencies for the three phases are shown in Figs. 5a–c,
259 respectively. Below a height of 3 km, the diabatic tendencies have a dipole structure for all three
260 phases. The most significant diabatic process leading to the changes in θ_e in the lower troposphere
261 is mixing and radiation. The latter acts to cool clear sky areas (i.e. those with low θ_e) while
262 having negligible impact in convective areas (Dauhut et al. 2017). The air parcels with high θ_e
263 (exceeding 342 K) have a negative diabatic tendency. These are rising air masses that are cooling
264 and drying via mixing with the surrounding air. The air parcels with lower θ_e have a positive
265 diabatic tendency showing warming and moistening behavior. Just below the freezing level, the
266 diabatic tendency is negative, with a pronounced minimum in the active and intermediate phases.
267 This likely corresponds to latent heat absorption due to ice melting and radiative cooling. Between
268 the freezing level and $z \simeq 14$ km, the diabatic tendencies also show a dipole structure; however,
269 air parcels with high θ_e have a positive diabatic tendency, while air parcels with low θ_e have a
270 negative diabatic tendency. We suggest interpreting the diabatic tendencies as follows. The high
271 θ_e air parcels undergo latent heat release due to ice formation, which contributes to the positive
272 diabatic tendency, exceeding the negative diabatic tendency due to mixing. The lower θ_e air parcels

273 have a negative diabatic tendency due to mixing with the lower environmental θ_e air masses, as
 274 well as due to ice sublimation and radiative cooling. In Periods 1 and 3 (Figs. 5a,c), a small
 275 number of air parcels with $\theta_e < 334$ K located above the freezing level have positive diabatic
 276 tendencies probably due to mixing because most of the air parcels have larger θ_e . In the overshoot
 277 circulation (Figs. 5a–c), the air masses with $\theta_e > \bar{\theta}_e$ have a negative diabatic tendency while those
 278 with $\theta_e < \bar{\theta}_e$ have a positive diabatic tendency. These tendencies are mostly due to mixing, similar
 279 to the air masses in the lower troposphere, but the contribution of the radiation might also exist
 280 (Dauhut et al. 2017). The amplitude of the diabatic tendencies is the largest in the active phase
 281 (Period 1) and the smallest in the suppressed phase (Period 3). This is in agreement with the
 282 strong convective activity during the active MJO phase and its weakening during the suppressed
 283 MJO phase.

284 For the Maritime Continent (Figs. 6a–c), the diabatic tendencies have a similar structure to
 285 those for the Indian Ocean (Figs. 5a–c). Nevertheless, the diabatic tendencies in the overshoot
 286 circulation have smaller values. Another difference is the absence of low θ_e air parcels with
 287 positive diabatic tendencies close to the freezing level.

288 The rising air parcels entrain the environmental air. The entrainment rate ε is computed in the
 289 form of an isentropic analysis using

$$\varepsilon(\theta_e^{env} - \theta_e) = \frac{\langle \rho \dot{\theta}_e \rangle}{\langle \rho_w \rangle}, \quad (4)$$

290 where θ_e^{env} indicates the environmental profile of θ_e . The entrainment rate is calculated here in a
 291 manner similar to that of Dauhut et al. (2017), while the average profile is used as the environmen-
 292 tal profile. This is a reasonable assumption as the average profile is close to the PDF maxima at
 293 every height (Figs. 3a–c and 4a–c). One condition to compute ε from Eq. (4) is that θ_e variations
 294 are solely due to mixing. This is the case below 4 km. Above, the ice processes and radiation (see

295 Dauhut et al. (2017)) produce diabatic tendencies that prevent the use of Eq. (4). Therefore, only
296 the entrainment below the freezing level is considered.

297 The entrainment rate for the Indian Ocean is shown in Figs. 5d–f. The air masses with θ_e close
298 to $\bar{\theta}_e$ have an entrainment rate larger than 1 km^{-1} , while the points with the largest θ_e values
299 have a weaker entrainment rate of less than 0.05 km^{-1} . As the largest θ_e air masses are located
300 in the core of wide updrafts, they are likely less affected by the entrainment and the subsequent
301 mixing with environmental air. A similar spectrum of entrainment rates as a function of the air
302 mass θ_e was found for the tropical multicellular storm studied by Dauhut et al. (2017) suggesting
303 the importance of a varying entrainment rate in convection parameterization (Del Genio et al.
304 2012). Note that the entrainment increases during the suppressed phase (Period 3). This could
305 be explained by the change of environment in which the updrafts develop. The dry air intrusions
306 (discussed in the following) lead the rising air masses to experience a stronger θ_e decrease when
307 mixed with the environment, leading to larger entrainment values during the suppressed phase. The
308 entrainment rates over the Maritime Continent (Figs. 6d–f) are similar to those over the Indian
309 Ocean in the amplitude, the largest entrainment rate being close to the average θ_e profile. The
310 entrainment rate decreases in Period 1. This corresponds to the result obtained for the Indian
311 Ocean, i.e. the largest entrainment rate corresponds to the suppressed phase of the MJO.

312 *d. Changes in the intensity of the overturning circulations*

313 To better understand the evolution of the large-scale circulations, it is also possible to consider
314 the evolution of a streamfunction calculated in the same way as the isentropic streamfunction in
315 Eq. (3) but without time averaging the vertical mass flux. Using this method, a streamfunction at
316 every output time is obtained.

317 For the Indian Ocean, the time evolutions of the maximum and minimum of this streamfunction,
318 together with the time evolution of the average relative humidity, are shown in Figs. 7a,b. The
319 overshoot circulation is visible with the highest values of the maximum of the streamfunction lo-
320 cated at z between 14 and 17 km. The intensity of the overshoot is highest at the beginning of the
321 simulation and gradually decreases with time. The low θ_e circulation in the streamfunction can
322 also be traced using the streamfunction maximum, but in the low troposphere. At the beginning
323 of the simulation, this circulation is weak with a local maximum exceeding $0.0001 \text{ kg m}^{-2} \text{ s}^{-1}$
324 at 0000 UTC 24 November near $z = 2$ km. This circulation then starts developing vertically after
325 0000 UTC 28 November and reaches 10 km around 1200 UTC 30 November. At several times
326 (around 0000 UTC and 2100 UTC 30 November) the associated values exceed $0.0005 \text{ kg m}^{-2} \text{ s}^{-1}$.
327 A short timescale variability is also observed, corresponding approximately to the diurnal variabil-
328 ity. The tropospheric circulation is depicted by the minimum of the streamfunction. It is the most
329 developed during the active phase of the MJO as stated previously. A second maximum is also
330 present near 0000 UTC 26 November, and a third maximum is present near 1500 UTC 28 Novem-
331 ber both located near 4 km. A moistening of the upper troposphere is visible during the active
332 and intermediate phases of the MJO (23–28 November), as shown in Fig. 7b, while during the
333 suppressed phase (29 November – 1 December), a drying of the lower troposphere is observed.
334 This drying extends in depth with time. At 0000 UTC 1 December, the relative humidity is less
335 than 60% at z between 3 and 5 km, and less than 80% at z between 0.5 and 3 km. A similar
336 drying was described by Wang et al. (2015) as observed in the North Sounding Array during the
337 CINDY/DYNAMO campaign. Hagos et al. (2014) showed the drying during the transition from
338 the active phase of the MJO to the suppressed phase during 3–4 days.

339 For the Maritime Continent, the overshoot circulation has its largest intensity at the beginning
340 and end of the simulation (Fig. 8a). The low θ_e circulation is not very well developed, with

341 discrete maxima between $0.0001 \text{ kg m}^{-2} \text{ s}^{-1}$ and $0.0005 \text{ kg m}^{-2} \text{ s}^{-1}$ for z between 2 and 7 km,
342 until 0000 UTC 29 November. The upper troposphere shows a diurnal variability in its relative
343 humidity (Fig. 8b) and is the closest to saturation at the end of the simulation. The strong drying
344 of the middle troposphere is visible from 0000 UTC 25 November to 1200 UTC 27 November,
345 corresponding to the largest amplitudes of the low θ_e circulation in Fig. 8a. In contrast with the
346 Indian Ocean, the drying does not extend down to the lower troposphere. The relative humidity
347 decreases below 60% at z between 6 and 12 km while remaining above 80% at z between 0 and
348 2.5 km all along the simulation.

349 **4. Signature of dry air intrusions in the propagation of the MJO**

350 As discussed in Section 3b, a low θ_e upward circulation is observed in the streamfunction plots,
351 which is more distinct for the case of the Indian Ocean during the suppressed phase. Here, we
352 concentrate on 1800 UTC 30 November when the suppressed MJO phase is over the Indian Ocean.
353 The timing corresponds with the penetration of dry air intrusions into the equatorial region of the
354 Indian Ocean observed by Kerns and Chen (2014).

355 The horizontal cross sections at an altitude near 5 km (Fig. 9) allow for a better understanding
356 of the presence of the low θ_e circulation. The flow of air masses with low θ_e (less than 332 K)
357 is transported into the Indian Ocean subdomain from the north (Fig. 9a) forming the so-called
358 “dry air intrusion”. This intrusion also influences the average θ_e profile: as shown previously,
359 the minimum of $\bar{\theta}_e$ decreased during the suppressed MJO phase over the Indian Ocean, while the
360 changes in $\bar{\theta}_e$ over the Maritime Continent were weak. In Fig. 9b, the vertical velocity of the low
361 θ_e air masses (less than 330 K, similar to the low θ_e circulation in Fig. 3i) is shown to isolate the
362 dry airflow, with the zoom shown in Fig. 9c for all air masses. The vertical velocity is weak, with
363 upward motions of up to 0.2 m s^{-1} .

364 The vertical section from an altitude of 0 to 7 km, corresponding to the thick black line in the
365 horizontal cross sections (Figs. 9b,c), is shown in Fig. 10. The low θ_e pocket is visible in Fig. 10a
366 between $z \simeq 2$ km and $z \simeq 6$ km. The corresponding vertical velocities in Fig. 10b (shown here
367 for all θ_e) likely indicate the presence of gravity waves that could mix low θ_e air masses with
368 adjacent air masses when breaking. This is consistent with the gravity waves found in the lower
369 troposphere, associated with clear variations in moisture and a stronger activity in the suppressed
370 phase (Bellenger et al. 2017). θ_e shows a strong dependence on the relative humidity, as seen in
371 Fig. 10c. The low θ_e air masses have a relative humidity of less than 60%, including multiple
372 regions where θ_e is less than 327 K and the corresponding relative humidity is less than 20%.
373 Figure 10d shows the dry zones around a height of 5–6 km, with the lowest water vapor mixing
374 ratio being less than 2 g kg^{-1} , which corresponds to $\theta_e < 327 \text{ K}$. The shallow cloud tops are
375 located below 3 km, suggesting that the dry air intrusion limits their vertical development. This is
376 in agreement with the stream function that indicates a predominance of shallow convection during
377 the suppressed phase (Fig. 3i) whereas deep and congestus convection dominate during the active
378 and the intermediate phase, respectively (streamlines at largest values in Figs. 3g,h). This is also
379 consistent with the largest values of entrainment found during the suppressed phase over the Indian
380 Ocean.

381 **5. Conclusions**

382 A convection-permitting simulation of an MJO episode on 23–30 November 2011 was run to
383 describe the evolution of the atmosphere during the passage of the MJO over the Indian Ocean and
384 the Maritime Continent. An isentropic analysis was performed for two subdomains focusing on
385 the central Indian Ocean and the western part of the Maritime Continent.

386 The isentropic analysis showed the existence of three large-scale convective circulations. The
387 first one is a tropospheric circulation extending from the surface up to 14 km above the ground
388 level. Its intensity increases during the active phase of the MJO and decreases during the sup-
389 pressed phase, a feature also found for the October 2011 event by Chen et al. (2018).

390 The second circulation is an overshoot within the tropical tropopause layer, which is a new aspect
391 in this study. Such circulation has been found for a tropical multi cellular storm, but during its very
392 deep convection phase only (Dauhut et al. 2017), and was not obtained by Chen et al. (2018). In
393 this work, the overshoot circulation exists all along the convection-permitting simulation, over both
394 the Indian Ocean and the Maritime Continent. Its intensity is higher during the active phase of the
395 MJO, similar to the evolution of the tropospheric circulation. This suggests that the convective
396 activity can impact the composition of the tropical tropopause layer significantly. Entrainment
397 rates with values as low as 0.05 km^{-1} are seen for the air masses with the largest θ_e values.
398 Similar low values were found for the very deep convective system analyzed by Dauhut et al.
399 (2017) and partly explain the existence of the overshoot circulation. Understanding the reasons
400 for the continuous presence of the overshoot circulation as well as its significance for water vapor
401 transport into the stratosphere will be subject of future research.

402 The third circulation is characterized by low θ_e values and is located in the lower free tropo-
403 sphere, more pronounced in the case of the Indian Ocean. Unlike the two other circulations, the
404 low θ_e circulation intensifies and becomes much stronger during the suppressed phase of the MJO.
405 The appearing of this circulation and its evolution with the MJO passage is another new finding
406 of this study. The development of the low θ_e circulation is related to the dry air intrusions from
407 the subtropical zones into the equatorial region, which contributes to a further suppression of the
408 convection after the passage of the active MJO phase. While the dry air intrusions have already
409 been observed during the November 2011 episode of the MJO (Kerns and Chen 2014), we show

410 that they can be identified by means of the isentropic analysis. The mean vertical motion ob-
411 served during CINDY/DYNAMO (e.g., Johnson and Ciesielski 2013) is further investigated here
412 by decomposition according to θ_e values. This allows us to reveal the vertical motions associ-
413 ated with the dry air intrusions. Low θ_e air masses might be probably transported up by gravity
414 waves. Investigations of additional MJO episodes are necessary in order to understand whether
415 dry air intrusions are common in the passage of the MJO and to assess their inhibiting role in the
416 development of convection.

417 The diabatic tendencies do not show any significant changes in structure during the passage
418 of the MJO. Their amplitudes, however, change with the convective activity, with increases in the
419 amplitudes occurring during the active phase. Such increases are more pronounced over the Indian
420 Ocean than over the Maritime Continent. The entrainment rates increase during the suppressed
421 phase of the MJO over the Indian Ocean, and in a lesser extent over the Maritime Continent. These
422 variations are attributed to the dry air intrusions that lead the mixing between the rising motions
423 and their environment to have a stronger inhibiting impact on convection. Further research on
424 dry air intrusions may help understanding their role in inhibiting convection and drying the lower
425 troposphere and whether this gradual drying is due to gravity wave breaking. Finally, the findings
426 here are based on a simulation that mimics well the passage of the MJO over the Indian Ocean,
427 but which prevents precipitation from crossing the Maritime Continent. As a result, changes of
428 smallest amplitude in different characteristics of the atmospheric overturning over the Maritime
429 Continent should be taken with caution.

430 *Acknowledgments.* Computer resources were allocated by GENCI through Project 90569.
431 Thibaut Dauhut is supported by the IDEX TEASAO project. We thank the anonymous review-
432 ers for their comments, which helped to improve the overall quality of the paper.

References

- Bellenger, H., R. Wilson, J. L. Davison, J. P. Duvel, W. Xu, F. Lott, and M. Katsumata, 2017: Tropospheric turbulence over the tropical open ocean: Role of gravity waves. *J. Atmos. Sci.* **74**, 1249–1271, doi:10.1175/JAS-D-16-0135.1.
- Chaboureaud, J.-P., and P. Bechtold, 2005: Statistical representation of clouds in a regional model and the impact on the diurnal cycle of convection during Tropical Convection, Cirrus and Nitrogen Oxides (TROCCINOX). *J. Geophys. Res.*, **110**, D17 103, doi:10.1029/2004JD005645.
- Chen, S. S., and Coauthors, 2016: Aircraft observations of dry air, the ITCZ, convective cloud systems, and cold pools in MJO during DYNAMO. *Bull. Amer. Meteor. Soc.*, **97** (3), 405–423, doi:10.1175/BAMS-D-13-00196.1.
- Chen, X., O. M. Pauluis, and F. Zhang, 2018: Atmospheric overturning across multiple scales of an MJO event during the CINDY/DYNAMO campaign. *J. Atmos. Sci.*, **75**, 381–399, doi:10.1175/JAS-D-17-0060.1.
- Cuxart, J., P. Bougeault, and J.-L. Redelsperger, 2000: A turbulence scheme allowing for mesoscale and large-eddy simulations. *Quart. J. Roy. Meteor. Soc.*, **126** (562), 1–30, doi:10.1002/qj.497126562022.
- Dauhut, T., J.-P. Chaboureaud, P. Mascart, and O. Pauluis, 2017: The atmospheric overturning induced by Hector the Convecton. *J. Atmos. Sci.*, **74** (10), 3271–3284, doi:10.1175/JAS-D-17-0035.1.
- Deardorff, J. W., 1980: Stratocumulus-capped mixed layers derived from a three-dimensional model. *Bound. Layer Meteor.*, **18** (4), 495–527, doi:10.1007/BF00119502.

- 454 Del Genio, A. D., Y. Chen, D. Kim, and M. Yao, 2012: The MJO transition from shallow to deep
455 convection in CloudSat/CALIPSO data and GISS GCM simulations. *J. Climate*, **25**, 3755–3770,
456 doi:10.1175/JCLI-D-11-00384.1.
- 457 DePasquale, A., C. Schumacher, and A. Rapp, 2014: Radar observations of MJO and Kelvin wave
458 interactions during DYNAMO/CINDY2011/AMIE. *J. Geophys. Res. Atmos.*, **119** (11), 6347–
459 6367, doi:10.1002/2013JD021031.
- 460 Emanuel, K. A., 1994: *Atmospheric convection*. Oxford University Press, 580 pp.
- 461 Fouquart, Y., and B. Bonnel, 1986: Computations of solar heating of the Earth's atmosphere: A
462 new parametrization. *Beitr. Phys. Atmos.*, **53**, 35–62.
- 463 Gill, A. E., 1980: Some simple solutions for heat-induced tropical circulation. *Quart. J. Roy.*
464 *Meteor. Soc.*, **106** (449), 447–462, doi:10.1002/qj.49710644905.
- 465 Hagos, S., Z. Feng, K. Landu, and C.N. Long, 2014: Advection, moistening, and shallow-to-deep
466 convection transitions during the initiation and propagation of Madden–Julian Oscillation. . *J.*
467 *Adv. Model. Earth Syst.*, **6** (3), 938–949, doi:10.1002/2014MS000335.
- 468 Huffman, G. J., and Coauthors, 2007: The TRMM multisatellite precipitation analysis (TMPA):
469 Quasi-global, multiyear, combined-sensor precipitation estimates at fine scales. *J. Hydrometeor.*,
470 **8**, 38–55, doi:10.1175/JHM560.1.
- 471 Johnson, R. H., and P. E. Ciesielski, 2013: Structure and properties of Madden–Julian oscillations
472 deduced from DYNAMO sounding arrays. *jas*, **70**(10),3157–3179, doi = 10.1175/JAS-D-13-
473 065.1.

474 Kerns, B., and S. Chen, 2014: Equatorial dry air intrusion and related synoptic variability in
475 MJO initiation during DYNAMO. *Mon. Wea. Rev.*, **142**, 1326–1343, doi = 10.1175/MWR-D-
476 13-00159.1.

477 Lac, C., and Coauthors, 2018: Overview of the Meso-NH model version 5.4 and its applications.
478 *Geosci. Model Dev. Discuss.*, **11**, 1929–1969, doi:10.5194/gmd-11-1929-2018.

479 Lafore, J.-P., and Coauthors, 1998: The Meso–NH atmospheric simulation system. Part I:
480 adiabatic formulation and control simulations. *Ann. Geophys.*, **16**, 90–109, doi:10.1007/
481 s00585-997-0090-6.

482 Machado, L. A. T., and J.-P. Chaboureaud, 2015: Effect of turbulence parameterization on assess-
483 ment of cloud organization. *Mon. Wea. Rev.*, **143**, 3246–3262, doi:10.1175/MWR-D-14-00393.
484 1.

485 Madden, R., and P. Julian, 1972: Description of global-scale circulation cells in the tropics with a
486 40–50 day period. *J. Atmos. Sci.*, **29**, 1109–1123.

487 Madden, R. A., and P. R. Julian, 1971: Detection of a 40–50 day oscillation in the zonal wind in
488 the tropical Pacific. *J. Atmos. Sci.*, **28**, 702–708.

489 Masson, V., and Coauthors, 2013: The SURFEXv7.2 land and ocean surface platform for coupled
490 or offline simulation of Earth surface variables and fluxes. *Geosci. Model Dev.*, **6**, 929–960,
491 doi:10.5194/gmd-6-929-2013, URL <http://www.geosci-model-dev.net/6/929/2013/>.

492 Mlawer, E. J., S. J. Taubman, P. D. Brown, M. J. Iacono, and S. A. Clough, 1997: Radiative transfer
493 for inhomogeneous atmospheres: RRTM, a validated correlated-k model for the longwave. *J.*
494 *Geophys. Res.*, **102**, 16 663–16 682, doi:10.1029/97JD00237.

- 495 Moncrieff, M. W., D. E. Waliser, M. J. Miller, M. A. Shapiro, G. R. Asrar, and J. Caughey, 2012:
496 Multiscale convective organization and the YOTC Virtual Global Field Campaign. *Bull. Amer.*
497 *Meteor. Soc.*, **93**, 1171–1187, doi:10.1175/BAMS-D-11-00233.1.
- 498 Nakazawa, T., 1988: Tropical super clusters within intraseasonal variations over the western Pa-
499 cific. *J. Meteor. Soc. Japan*, **66**, 823–836.
- 500 Pantillon, F., P. Mascart, J.-P. Chaboureau, C. Lac, J. Escobar, and J. Duron, 2011: Seamless
501 Meso-NH modeling over very large grids. *C. R. Mecanique*, **339**, 136–140, doi:10.1016/j.crme.
502 2010.12.002.
- 503 Pauluis, O. M., and A. A. Mrowiec, 2013: Isentropic analysis of convective motions. *J. Atmos.*
504 *Sci.*, **70**, 3673–3688, doi:10.1175/JAS-D-12-0205.1.
- 505 Pergaud, J., V. Masson, S. Malardel, and F. Couvreux, 2009: A parameterization of dry thermals
506 and shallow cumuli for mesoscale numerical weather prediction. *Bound. Layer Meteor.*, **132**,
507 83–106, doi:10.1007/s10546-009-9388-0.
- 508 Pinty, J.-P., and P. Jabouille, 1998: A mixed-phase cloud parameterization for use in a mesoscale
509 non-hydrostatic model: Simulations of a squall line and of orographic precipitations. *Conf. on*
510 *cloud physics, Everett, WA, Amer. Meteor. Soc.*, 217–220.
- 511 Wang, S., and Coauthors, 2015: Regional simulation of the October and November MJO events
512 observed during the CINDY/DYNAMO field campaign at gray zone resolution. *J. Climate*,
513 **28** (6), 2097–2119, doi:10.1175/JCLI-D-14-00294.1.
- 514 Yoneyama, K., C. Zhang, and C. N. Long, 2013: Tracking pulses of the Madden–Julian oscillation.
515 *Bull. Amer. Meteor. Soc.*, **94**, 1871–1891, doi:10.1175/BAMS-D-12-00157.1.

516 Zhang, C., 2005: Madden–Julian oscillation. *Rev. Geophys.*, **43**, RG2003–2005, doi:10.1029/
517 2004RG000158.

518 Zhang, C., J. Gottschalck, E. D. Maloney, M. W. Moncrieff, F. Vitart, D. E. Waliser, B. Wang,
519 and M. C. Wheeler, 2013: Cracking the MJO nut. *Geophys. Res. Lett.*, **40**, 1223–1230, doi:
520 10.1002/grl.50244.

521 Zhang, C., and K. Yoneyama, 2017: *CINDY/DYNAMO field campaign: Advancing our under-*
522 *standing of MJO initiation*, World Scientific Series on Asia-Pacific Weather and Climate, Vol. 9,
523 339–348. World Scientific Publishing Co. Pte Ltd, doi:10.1142/9789813200913_0027.

524 [FIG. 1 about here.]

525 [FIG. 2 about here.]

526 [FIG. 3 about here.]

527 [FIG. 4 about here.]

528 [FIG. 5 about here.]

529 [FIG. 6 about here.]

530 [FIG. 7 about here.]

531 [FIG. 8 about here.]

532 [FIG. 9 about here.]

533 [FIG. 10 about here.]

534 **LIST OF FIGURES**

535 **Fig. 1.** Domain of simulation (Indian Ocean and Maritime Continent), with elevation (m) shaded. . . . 28

536 **Fig. 2.** Hovmöller diagram of the precipitation averaged over the region of 7.5°S–7.5°N for (a)
 537 TRMM and (b) the simulation. The vertical lines show the studied domains: the Indian
 538 Ocean, 60°–80°E, and the Maritime Continent, 100°–120°E. The horizontal lines show the
 539 time periods chosen for the analyses of the different MJO phases. 29

540 **Fig. 3.** Isentropic diagrams for the Indian Ocean: PDF (upper row), vertical mass flux (middle
 541 row), and streamfunction (bottom row). The left, middle, and right columns correspond to
 542 Periods 1 (the passage of the active phase), 2 (the intermediate phase between the active
 543 and the suppressed ones), and 3 (the suppressed phase), respectively. The thick black line
 544 corresponds to the θ_e profile averaged over all the grid points during the corresponding time
 545 period. 30

546 **Fig. 4.** As in Fig. 3, but for the Maritime Continent. Period 1 occurs during the suppressed MJO
 547 phase, Period 2 is just before the active phase, although convection is still suppressed, and
 548 Period 3 is after the beginning of the active phase. 31

549 **Fig. 5.** Isentropic diagrams for the Indian Ocean: diabatic tendency (upper row) and entrainment
 550 rate (bottom row). The left, middle, and right columns correspond to Periods 1, 2, and 3,
 551 respectively. The black line near $z = 5$ km corresponds to the average freezing level. The
 552 gray contour shows the isentropic envelope. The average θ_e profile is also shown. 32

553 **Fig. 6.** As in Fig. 5, but for the Maritime Continent. 33

554 **Fig. 7.** Evolution of (a) the isentropic streamfunction maximum and (b) the relative humidity for the
555 Indian Ocean. The black contours in (a) correspond to the evolution of isentropic stream-
556 function minimum. The vertical lines show the time periods (Periods 1, 2, and 3) chosen for
557 the analyses of the different MJO phases. 34

558 **Fig. 8.** As in Fig. 7, but for the Maritime Continent. 35

559 **Fig. 9.** (a) Spatial distribution of θ_e at 4.9-km height at 1800 UTC 30 November for the entire
560 simulation domain. The white rectangle denotes the Indian Ocean subdomain (7.5°S – 7.5°N ,
561 60° – 80°E). (b) Horizontal section of the vertical velocity for $\theta_e < 330\text{ K}$ for the domain
562 shown by the white rectangle in (a). The black rectangle denotes the zoom on (1.5°N – 4.5°N ,
563 69° – 73°E). (c) Horizontal section of the vertical velocity (for all θ_e) for the domain shown
564 by the black rectangle in (b). The black contour shows the cloud envelope at 0.001 g kg^{-1} .
565 The arrows in all figures represent the horizontal wind at 4.9-km height. The black line in
566 (b) and (c) corresponds to the vertical sections shown in Fig. 10. 36

567 **Fig. 10.** Vertical section of (a) θ_e , (b) vertical velocity, (c) relative humidity, and (d) water vapor
568 mixing ratio frequency at 1800 UTC 30 November along 2.75°N latitude. The height range
569 is 0–7 km and the longitude range is 69.8° – 72.6°E . The black contour shows the cloud
570 envelope at 0.001 g kg^{-1} . The arrows represent the tangent wind (the vertical component
571 has been multiplied by a factor of 100). 37

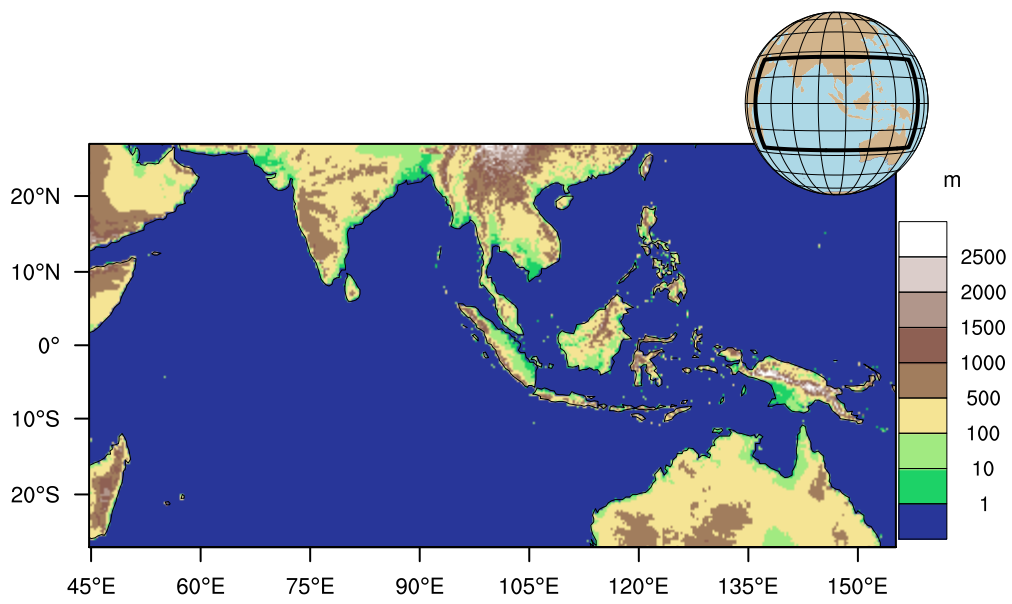
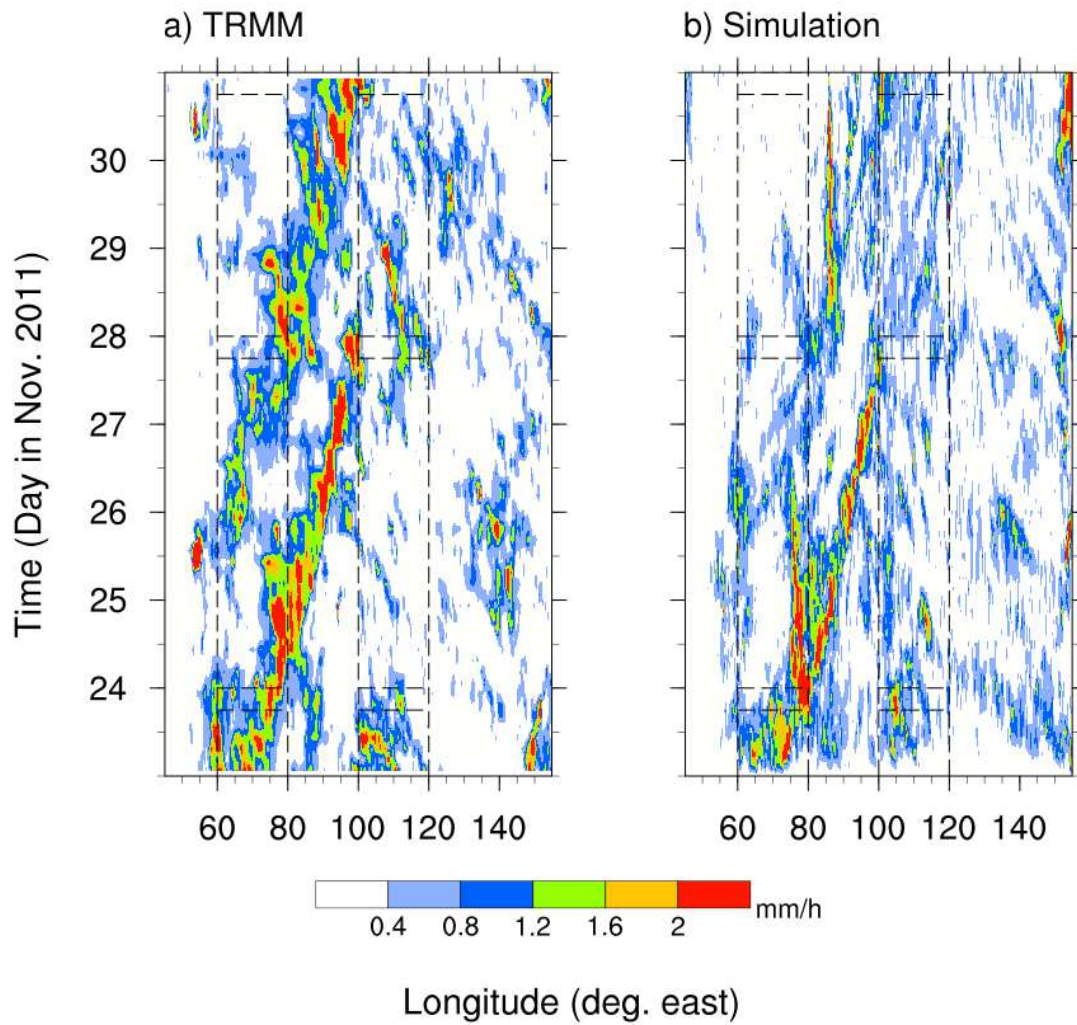
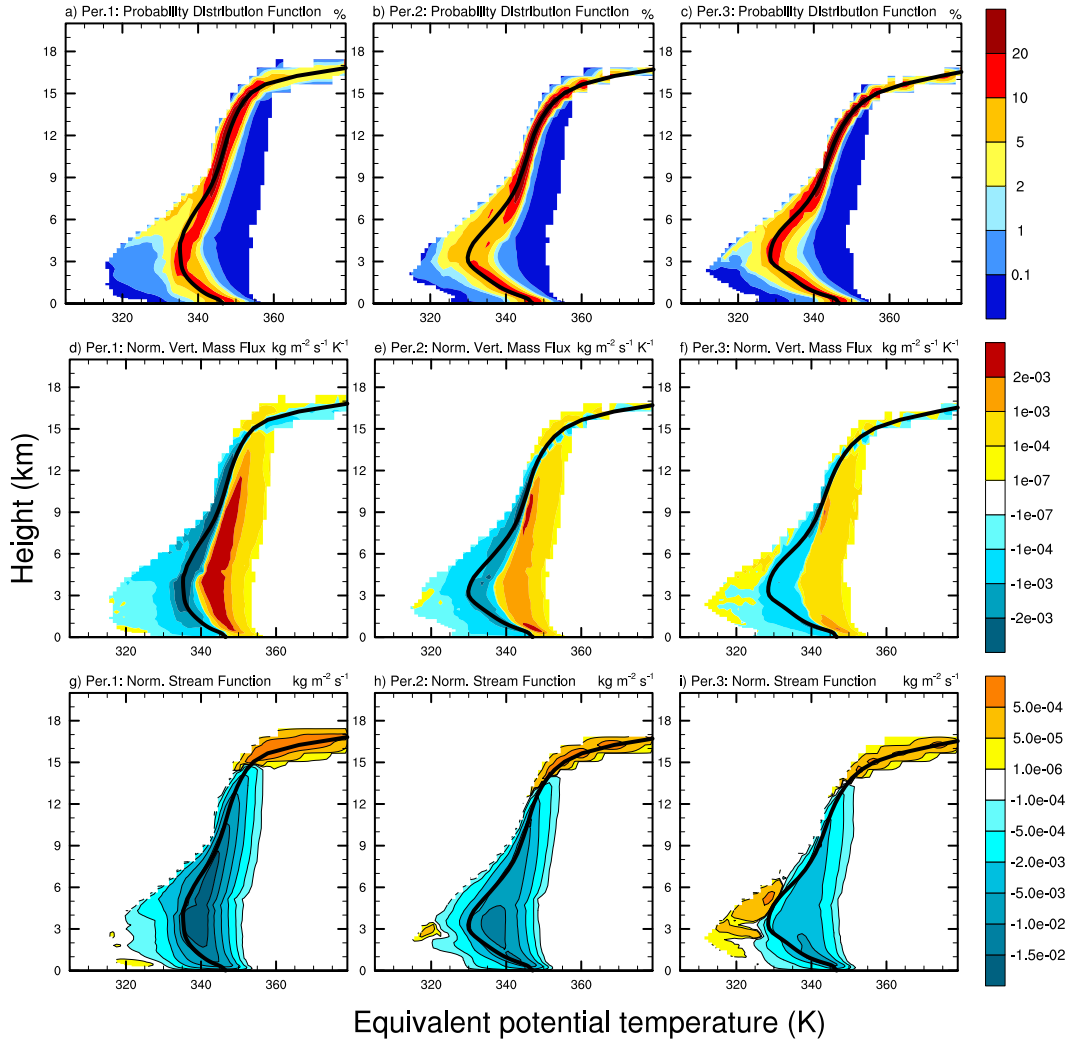


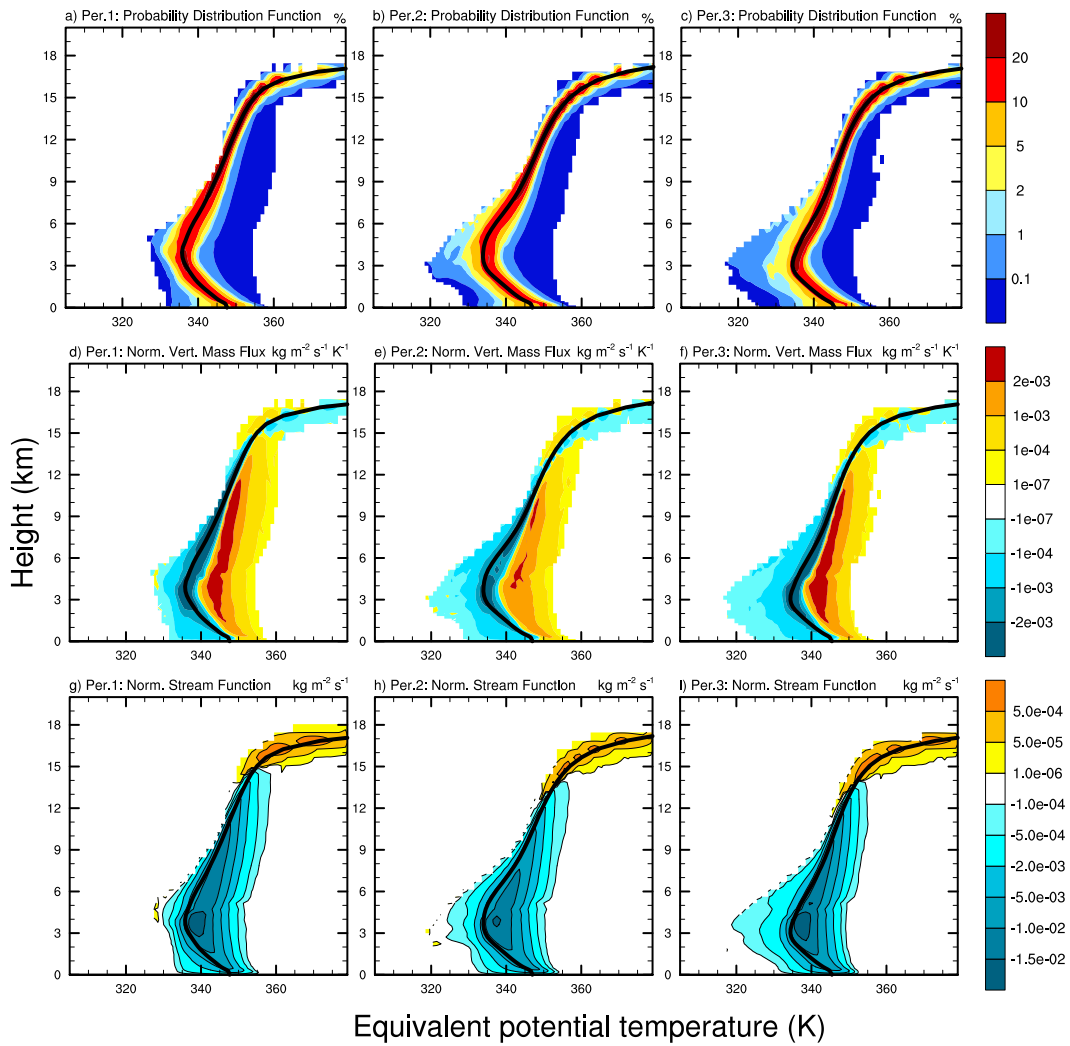
FIG. 1. Domain of simulation (Indian Ocean and Maritime Continent), with elevation (m) shaded.



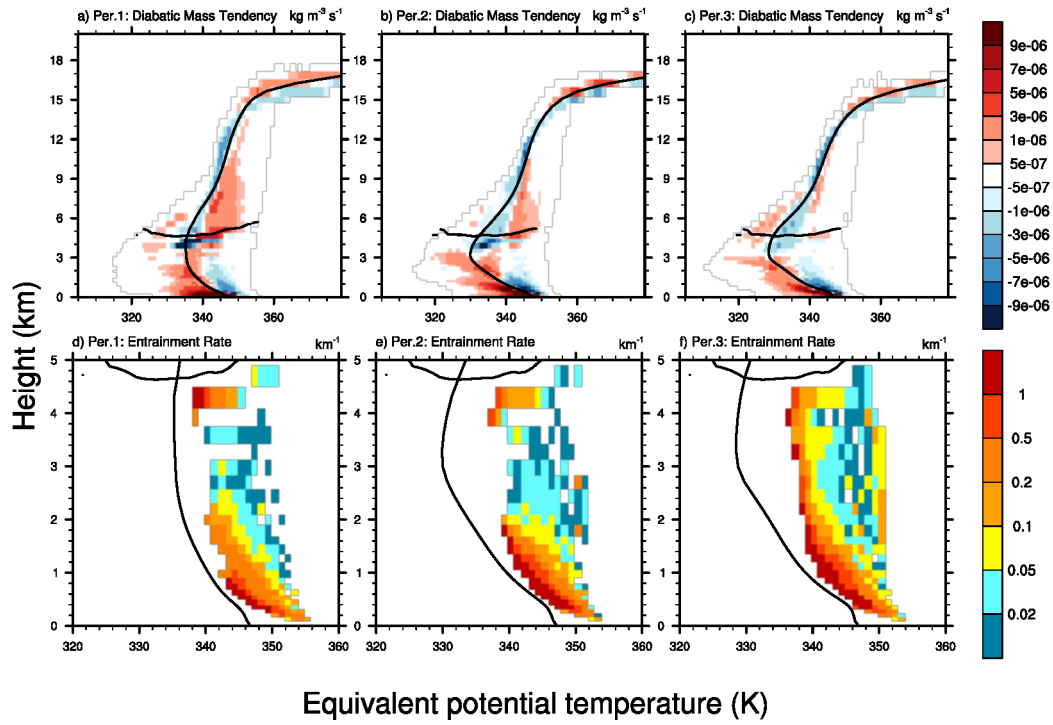
572 FIG. 2. Hovmöller diagram of the precipitation averaged over the region of 7.5°S – 7.5°N for (a) TRMM and
 573 (b) the simulation. The vertical lines show the studied domains: the Indian Ocean, 60° – 80°E , and the Maritime
 574 Continent, 100° – 120°E . The horizontal lines show the time periods chosen for the analyses of the different MJO
 575 phases.



576 FIG. 3. Isentropic diagrams for the Indian Ocean: PDF (upper row), vertical mass flux (middle row), and
 577 streamfunction (bottom row). The left, middle, and right columns correspond to Periods 1 (the passage of the
 578 active phase), 2 (the intermediate phase between the active and the suppressed ones), and 3 (the suppressed
 579 phase), respectively. The thick black line corresponds to the θ_e profile averaged over all the grid points during
 580 the corresponding time period.



581 FIG. 4. As in Fig. 3, but for the Maritime Continent. Period 1 occurs during the suppressed MJO phase,
 582 Period 2 is just before the active phase, although convection is still suppressed, and Period 3 is after the beginning
 583 of the active phase.



584 FIG. 5. Isentropic diagrams for the Indian Ocean: diabatic tendency (upper row) and entrainment rate (bottom
 585 row). The left, middle, and right columns correspond to Periods 1, 2, and 3, respectively. The black line near
 586 $z = 5$ km corresponds to the average freezing level. The gray contour shows the isentropic envelope. The average
 587 θ_e profile is also shown.

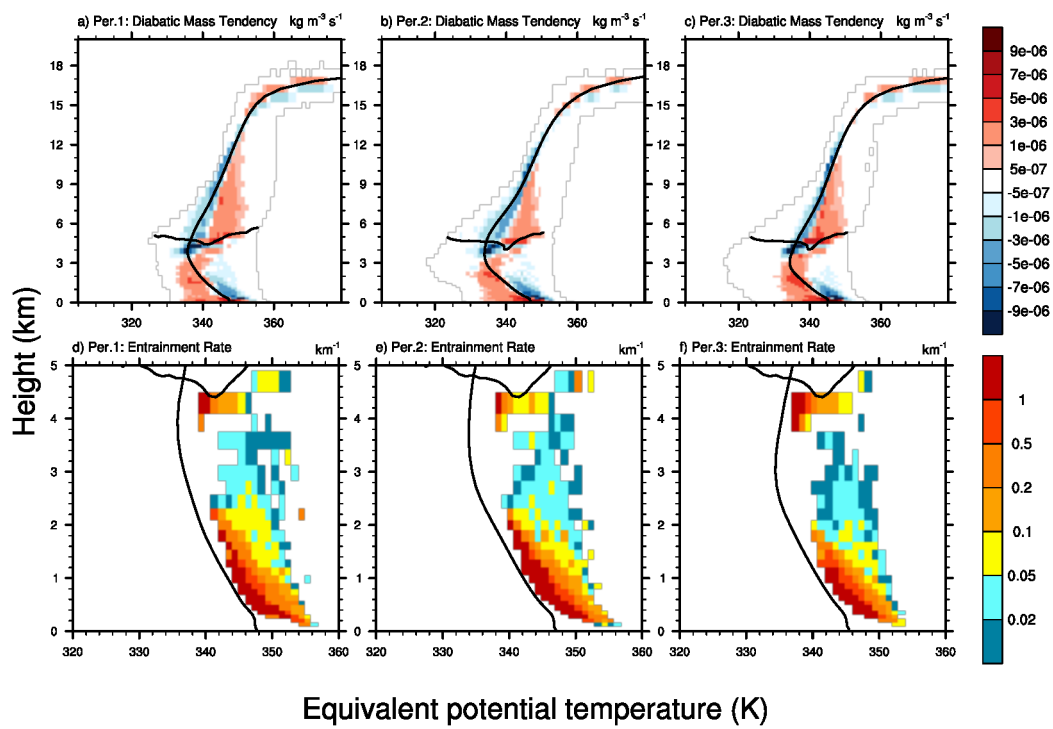
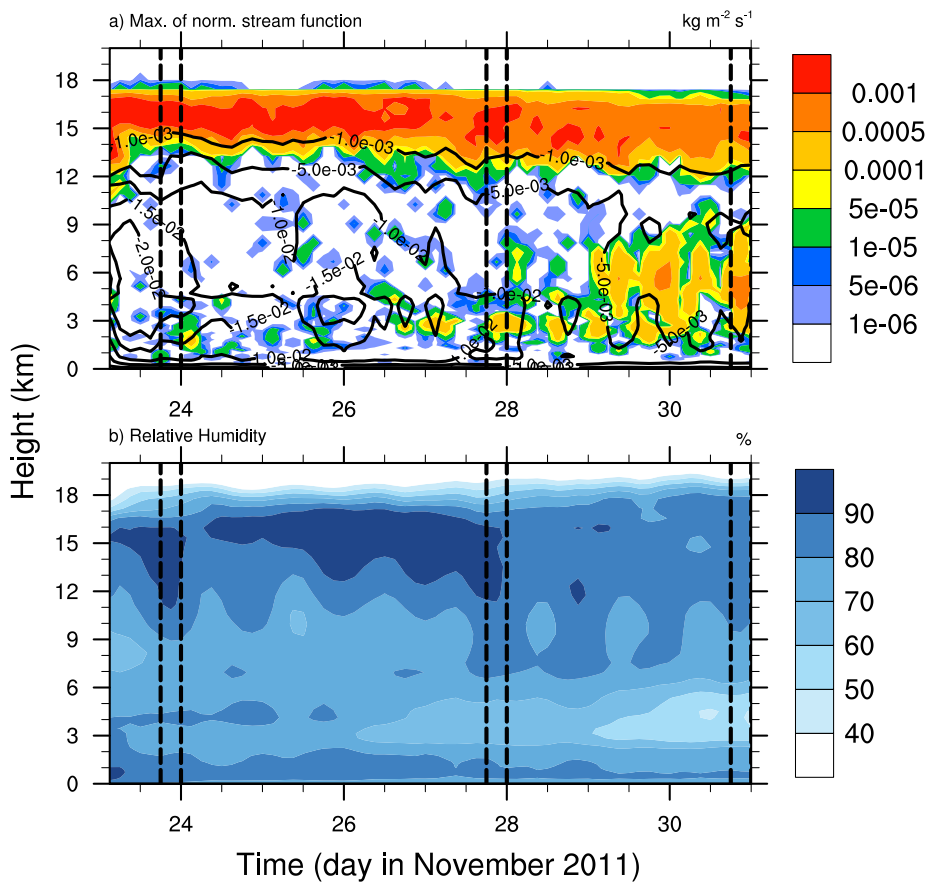


FIG. 6. As in Fig. 5, but for the Maritime Continent.



588 FIG. 7. Evolution of (a) the isentropic streamfunction maximum and (b) the relative humidity for the Indian
 589 Ocean. The black contours in (a) correspond to the evolution of isentropic streamfunction minimum. The
 590 vertical lines show the time periods (Periods 1, 2, and 3) chosen for the analyses of the different MJO phases.

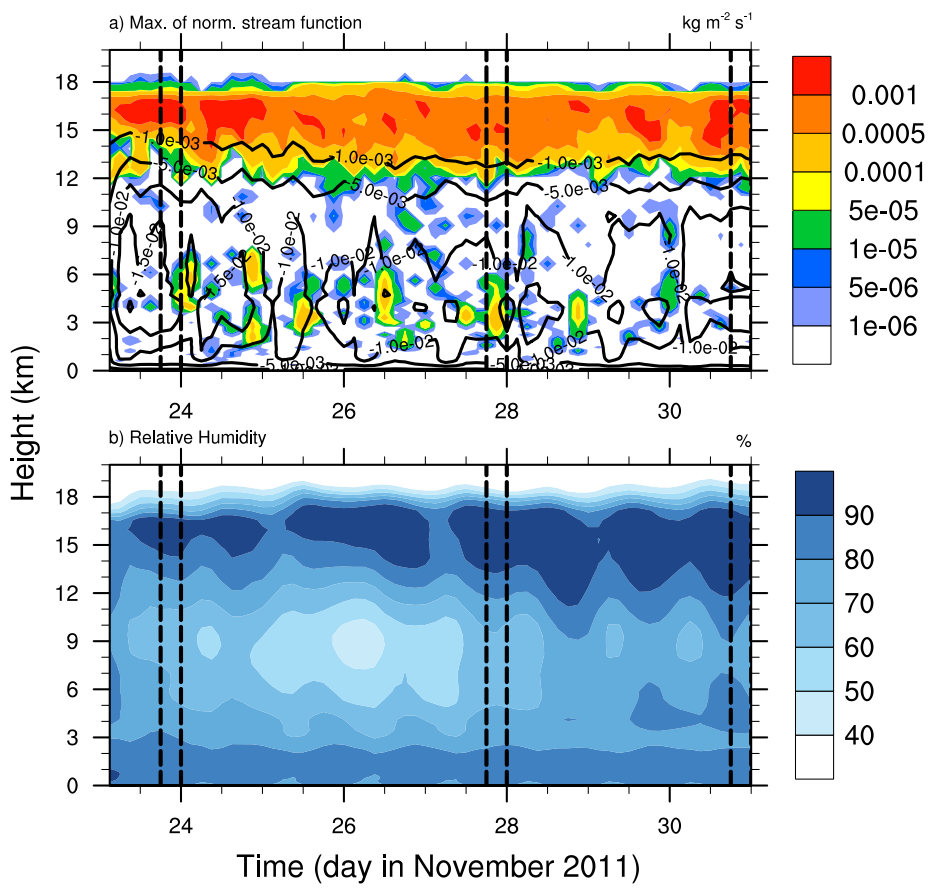
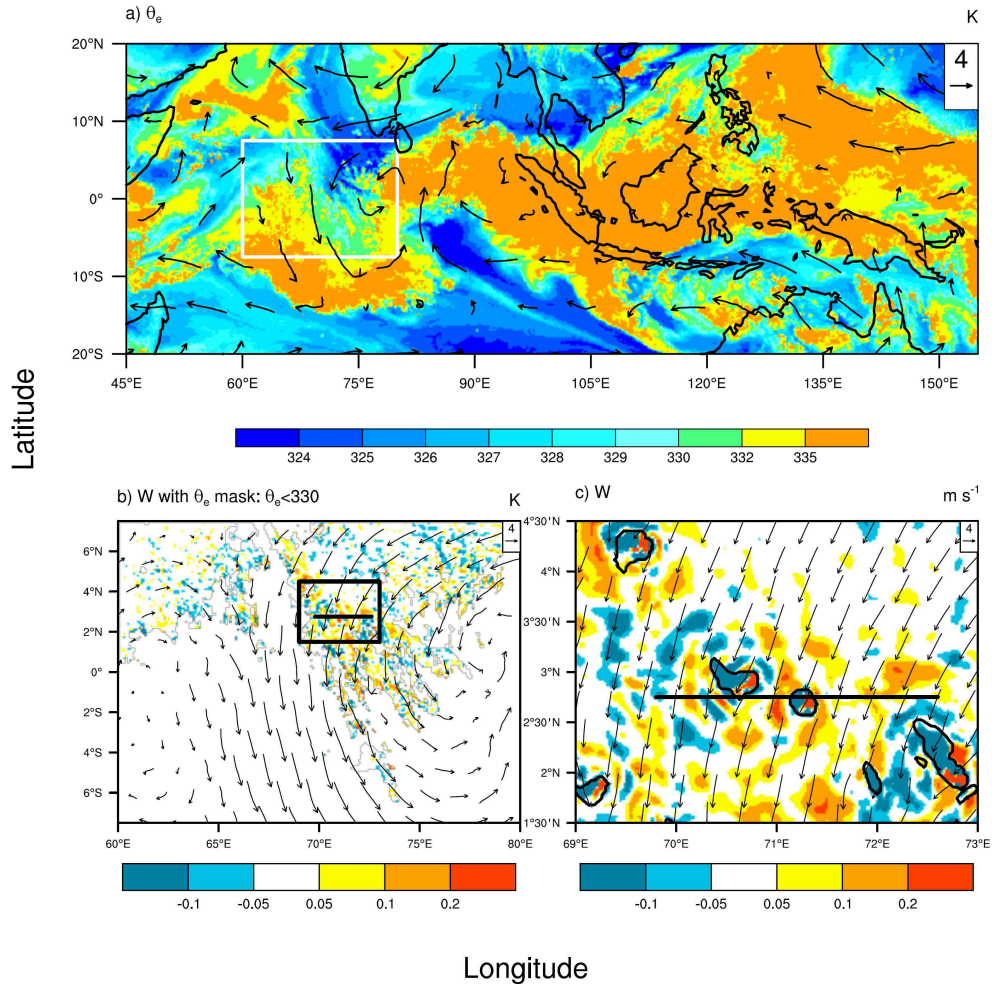
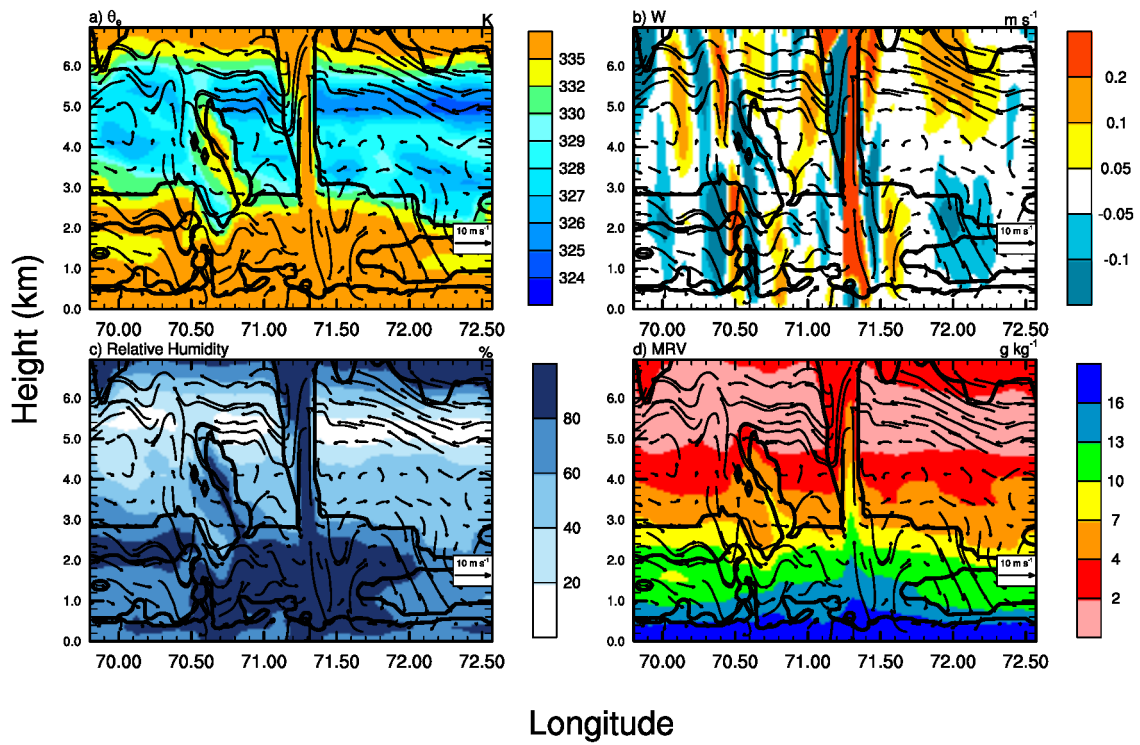


FIG. 8. As in Fig. 7, but for the Maritime Continent.



591 FIG. 9. (a) Spatial distribution of θ_e at 4.9-km height at 1800 UTC 30 November for the entire simulation
 592 domain. The white rectangle denotes the Indian Ocean subdomain (7.5°S–7.5°N, 60°–80°E). (b) Horizontal
 593 section of the vertical velocity for $\theta_e < 330$ K for the domain shown by the white rectangle in (a). The black
 594 rectangle denotes the zoom on (1.5°N–4.5°N, 69°–73°E). (c) Horizontal section of the vertical velocity (for
 595 all θ_e) for the domain shown by the black rectangle in (b). The black contour shows the cloud envelope at
 596 0.001 g kg^{-1} . The arrows in all figures represent the horizontal wind at 4.9-km height. The black line in (b) and
 597 (c) corresponds to the vertical sections shown in Fig. 10.



598 FIG. 10. Vertical section of (a) θ_e , (b) vertical velocity, (c) relative humidity, and (d) water vapor mixing ratio
 599 frequency at 1800 UTC 30 November along 2.75°N latitude. The height range is 0–7 km and the longitude range
 600 is 69.8° – 72.6°E . The black contour shows the cloud envelope at 0.001 g kg^{-1} . The arrows represent the tangent
 601 wind (the vertical component has been multiplied by a factor of 100).

4.3 Discussion

4.3.1 Dry air intrusions during the November 2011 MJO event

As shown in this article, some large-scale dry air flows develop in the subtropics and “intrude” into the equatorial region. It is interesting to see the development of these dry air intrusions during the passage of the MJO.

The evolution of large-scale spatial distribution of θ_e at $z \simeq 2.9$ km in case of the 2011 episode is shown in Fig. 4.1 for 1800 UTC 23 November 2011, 0000 UTC 28 November 2011, and 1800 UTC 30 November 2011. The white rectangles correspond to the domains described in the article included previously. To illustrate the relationship between θ_e and the relative humidity, the corresponding spatial distribution of the relative humidity for 1800 UTC 30 November 2011 is shown in Fig. 4.2 corresponding to Fig. 4.1c.

Comparing Figs. 4.1a–c, it is noticeable that in the simulation, the average θ_e in the whole domain is decreasing, e.g. by looking at the decrease of the total area of θ_e which exceeds 336 K. This decrease is not only due to the dry air intrusions, but also to the decrease of the highest θ_e values. On 1800 UTC 23 November 2011 (Fig. 4.1a), some dry air masses are located in the northwest of the simulation domain (around 15°N, 50°–80°E), in the northeast (20°N, 130°–140°E), and in the south (20°S, 55°–135°E). Their further intrusion towards the equator is especially visible over the Indian Ocean on 0000 UTC 28 November 2011 (Fig. 4.1b), where a large-scale air flow arrived from the north. Over the Maritime Continent, the dry air flows are more narrow and have greater θ_e values (mostly exceeding 321 K) as compared to the dry air flows in the western and the middle parts of the simulation domain with θ_e less than 315 K. On 1800 UTC 30 November 2011 (Fig. 4.1c, Fig. 4.2), the dry air intrusions are concentrated

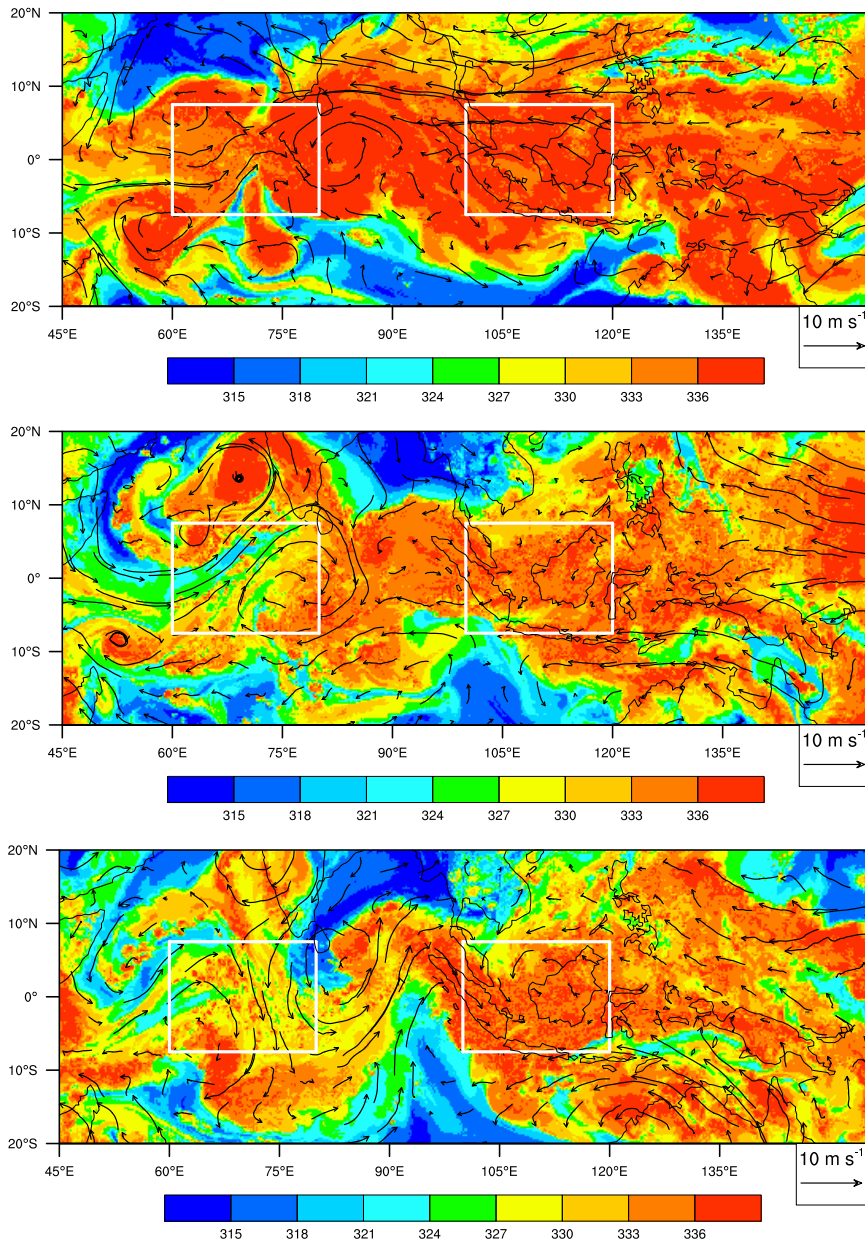


Figure 4.1: Spatial distribution of θ_e (K) at $z = 2.9$ km for the whole simulation domain. Top: 1800 UTC 23 November 2011, Middle: 0000 UTC 28 November 2011, Bottom: 1800 UTC 30 November 2011. White rectangles show the subdomains (Indian Ocean, 7.5°S–7.5°N, 60°–80°E, and Maritime Continent, 7.5°S–7.5°N, 100°–120°E). The arrows represent the horizontal wind (u, v).

in the north of the domain, around 20°N , $80^\circ\text{--}100^\circ\text{E}$, and in the south, around 15°S , $90^\circ\text{--}105^\circ\text{E}$. Most of the dry air intrusions occurred over the Indian Ocean.

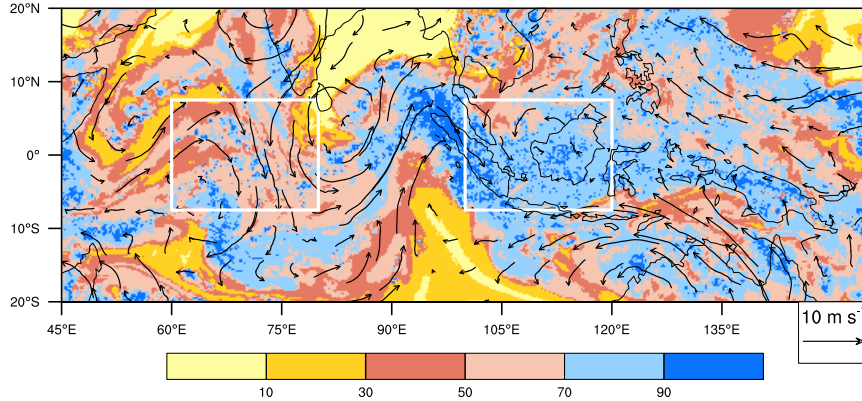


Figure 4.2: Spatial distribution of the relative humidity (%) at $z = 2.9$ km for the whole simulation domain at 1800 UTC 30 November 2011. White rectangles show the subdomains as in Fig. 4.1. The arrows represent the horizontal wind (u, v).

The evolution of the air properties over the Indian Ocean subdomain is shown in Figs. 4.3-4.6. On 1800 UTC 23 November, the low θ_e air intrusions around $z = 2.9$ km were located in the south of the subdomain focused on the Indian Ocean, around 7°S (Fig. 4.3a). These air flows have the distinct signature in the air temperature and they are at least 1 K warmer than the surrounding air (Fig. 4.3b). They show the relative humidity less than 40% and the water vapor mixing ratio less than 5 g kg^{-1} .

The vertical sections corresponding to the horizontal line at 6.7°S in Figs. 4.3a-d are shown in Fig. 4.4. The minima of these low θ_e air pockets are located at $z \simeq 3$ km (Fig. 4.4a) and the horizontal extent of these pockets does not exceed 1 degree of longitude. The positive vertical velocities in these zones are quite weak in this MJO phase, less than 0.1 m s^{-1} (Fig. 4.4b). The vertical section showing relative humidity (Fig. 4.4c) also allows to see two very dry air currents with relative humidity less than 20%, surrounded by the humid zones

with relative humidity reaching 80% and higher, concentrated inside the cloud contours of 0.001 g kg^{-1} . The corresponding water vapor mixing ratio is less than 2 g kg^{-1} in the dry zones (Fig. 4.4d).

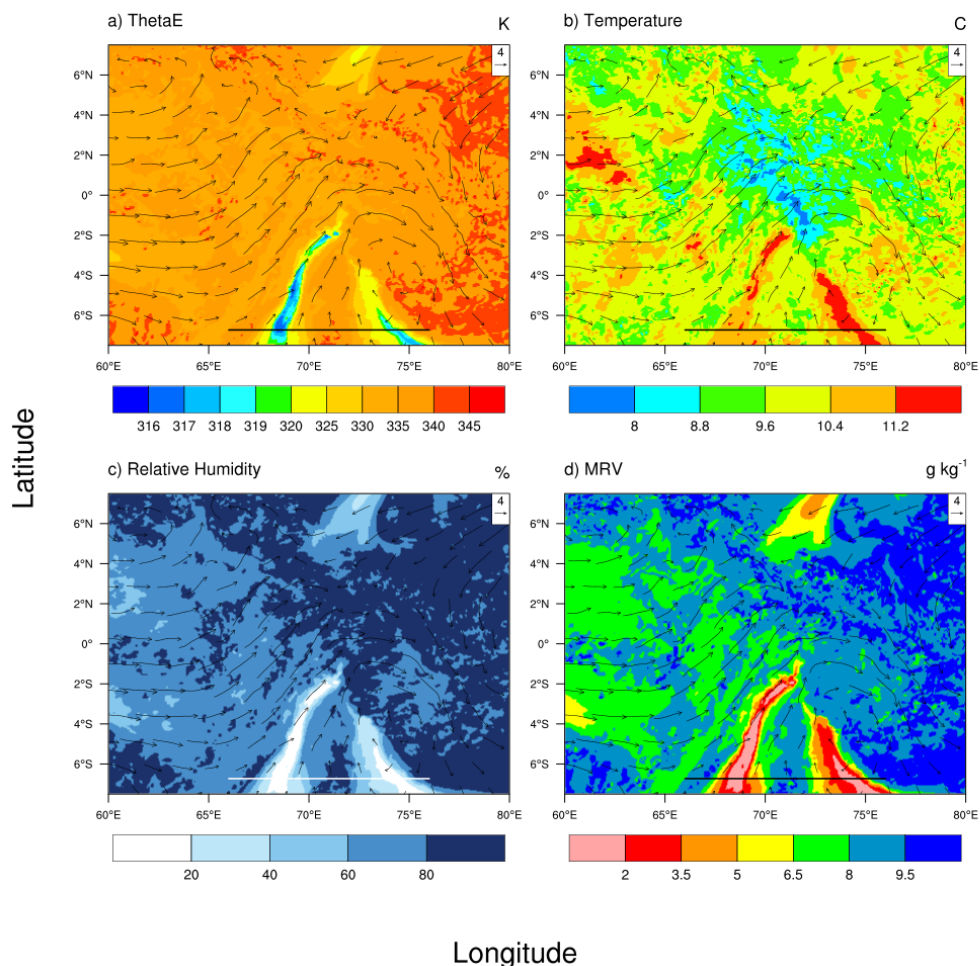


Figure 4.3: Horizontal sections of (a) θ_e , (b) temperature, (c) relative humidity, and (d) water vapor mixing ratio for the Indian Ocean subdomain ($60^\circ\text{--}80^\circ\text{E}$, $7.5^\circ\text{S--}7.5^\circ\text{N}$), at 1800 UTC 23 November 2011 and at $z = 2.9 \text{ km}$. The horizontal line at 6.7°S corresponds to the vertical sections shown in Fig. 4.4. The arrows represent the horizontal wind (u, v) .

During the intermediate MJO phase over the Indian Ocean, at 0000 UTC 28 November 2011, θ_e in the domain shown in Fig. 4.5a, decreases as compared to Fig. 4.3a. The temperature over the Indian Ocean becomes slightly higher

(Fig. 4.5b) and the air becomes drier (Figs. 4.5c–d). The horizontal extent of the low θ_e pockets (Fig. 4.6a) is now around 3 degrees of longitude. The updrafts become slightly stronger than during the active MJO phase (Fig. 4.6b). Nevertheless, the updrafts corresponding to the low θ_e pockets have generally the same amplitude as previously. The air in the low θ_e pocket becomes moister and reaches 40% in relative humidity (Fig. 4.6c), while the water vapor mixing ratio is around 2–6 g kg^{-1} in the most part of the dry zones (Fig. 4.6d).

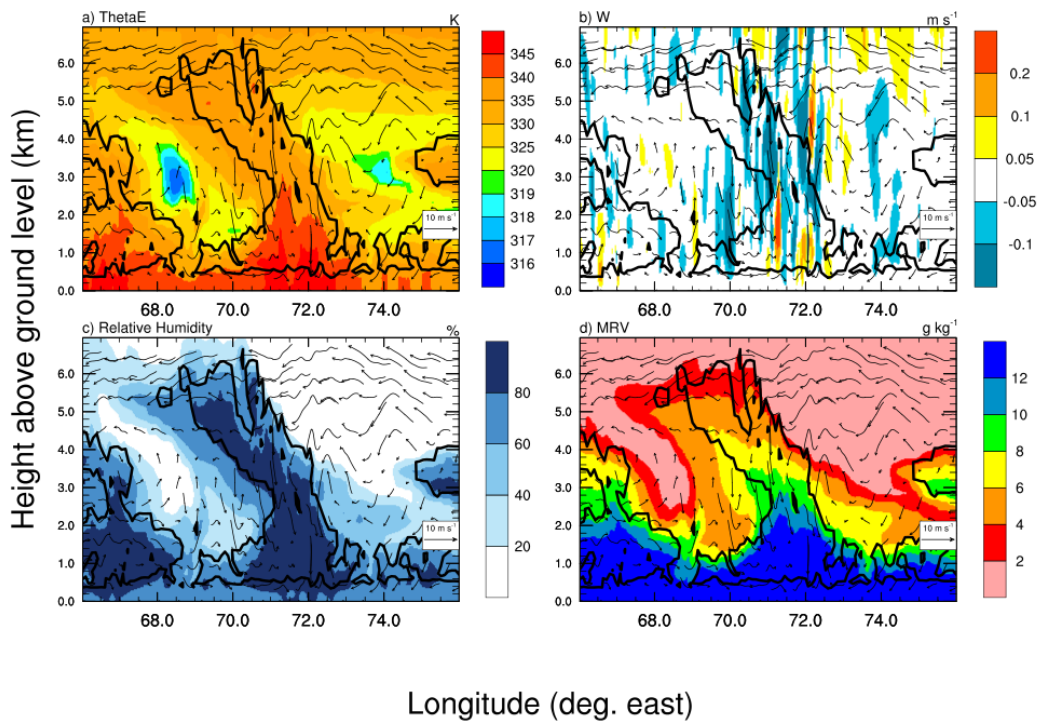


Figure 4.4: Vertical sections of (a) θ_e , (b) temperature, (c) relative humidity, and (d) water vapor mixing ratio at 1800 UTC 23 November 2011 along 6.7°S . The height range is 0–7 km and the longitude range is 66° – 76°E . The black contour shows the cloud envelope at 0.001 g kg^{-1} . The arrows represent the tangent wind ($u, 100 \cdot w$) where the vertical component has been multiplied by a factor of 100.

As shown in Figs. 9 and 10 of the article presented previously, the low θ_e pockets over the Indian Ocean are the most developed horizontally and vertically in the suppressed MJO phase.

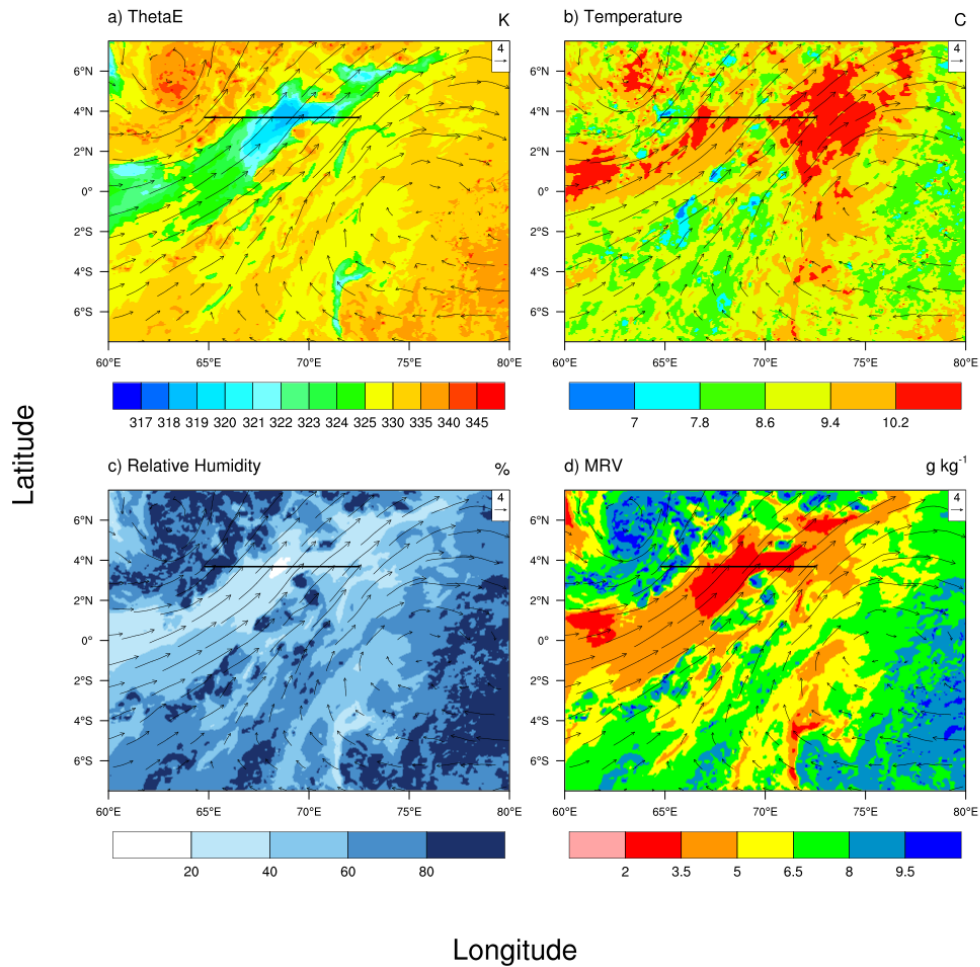


Figure 4.5: As in Fig. 4.3 but for 0000 UTC 28 November 2011. The horizontal line at 3.7°N corresponds to the vertical sections shown in Fig. 4.6. The arrows represent the horizontal wind (u, v).

4.3.2 Isentropic diagrams based on ECMWF data

Another way to see the correlation of the low θ_e and the low relative humidity is to use isentropic diagrams for the relative humidity. The comparison of Fig. 3 from the article with Figs. 4.7g–i shows that the zones with low θ_e appearing around $z = 3\text{--}6$ km correspond to the lowest relative humidity values, while the

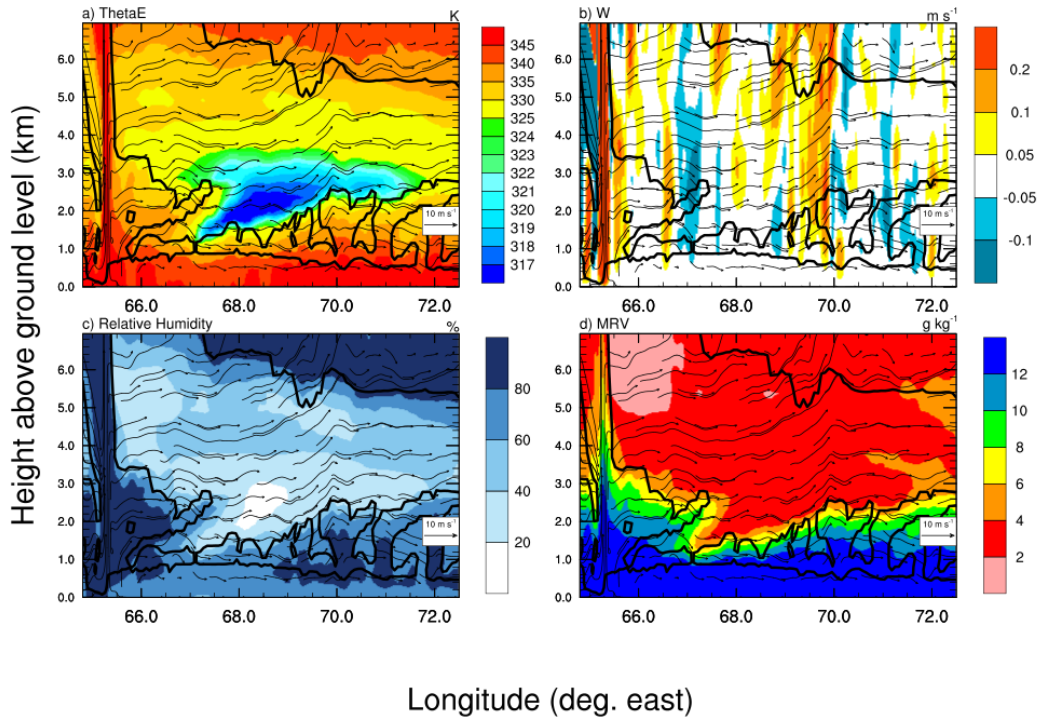


Figure 4.6: Vertical sections of (a) θ_e , (b) temperature, (c) relative humidity, and (d) water vapor mixing ratio at 0000 UTC 28 November 2011 along 3.7°N latitude. The height range is 0–7 km and the longitude range is 64.8° – 72.5°E . The black contour shows the cloud envelope at 0.001 g kg^{-1} . The arrows represent the tangent wind ($u, 100 \cdot w$) where the vertical component has been multiplied by a factor of 100.

largest relative humidity values correspond to high θ_e air masses.

The conclusion of the article can be further verified by looking at the isentropic diagrams constructed for the ECMWF analyses for the same time periods. Comparing Figs. 4.7a–c with Figs. 4.7d–f, it is possible to see that the simulation reproduces the same patterns existing in the ECMWF analyses, in spite of too large relative humidity values corresponding to the air parcels with $\theta_e > \bar{\theta}_e$.

The distribution of air parcels in the ECMWF analyses over the Indian Ocean (Figs. 4.7g–i) is generally similar to that obtained in the simulation. Nevertheless, in the ECMWF diagrams the air parcels with the highest frequency are located not exactly around the average profile, but on the right of it for z be-

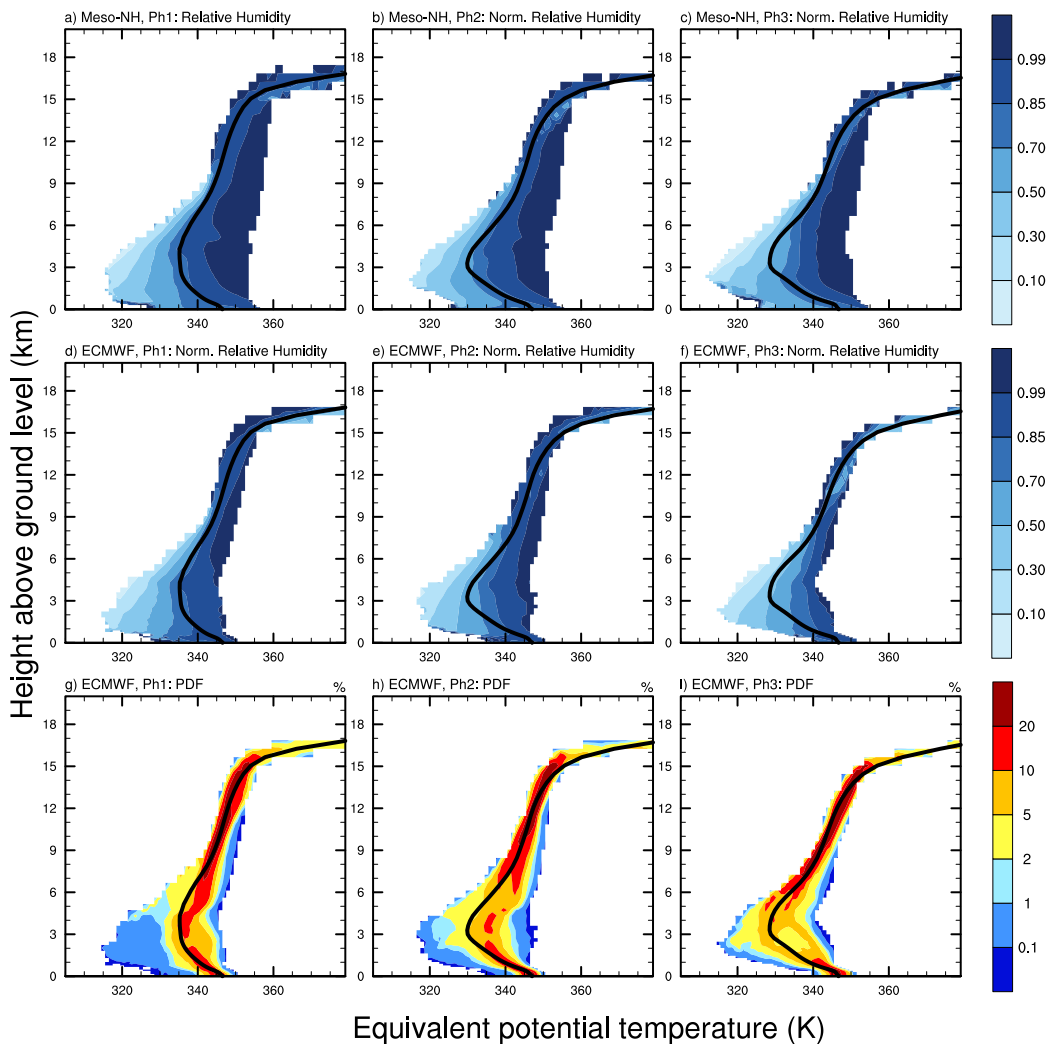


Figure 4.7: Isentropic diagrams for the Indian Ocean: relative humidity for the simulation (upper row), relative humidity for ECMWF (middle row), and PDF for ECMWF (bottom row). The left column corresponds to the Period 1 (the passage of the active phase of the MJO), the middle column, to the Period 2 (the intermediate phase between the active and the suppressed ones), and the right column, to the Period 3 (the suppressed phase of the MJO). The thick black line corresponds to the θ_e profile averaged over all grid points during the corresponding time period.

tween 1 and 8 km in the active and the intermediate MJO phases (Periods 1 and 2). During the suppressed phase (Fig. 4.7i), there is a drop in frequency around $z = 2$ km for air parcels with θ_e between 330 and 340 K, close to the average

profile, which was not observed in the simulation. On the contrary, the increase in frequency for low θ_e air parcels is well reproduced.

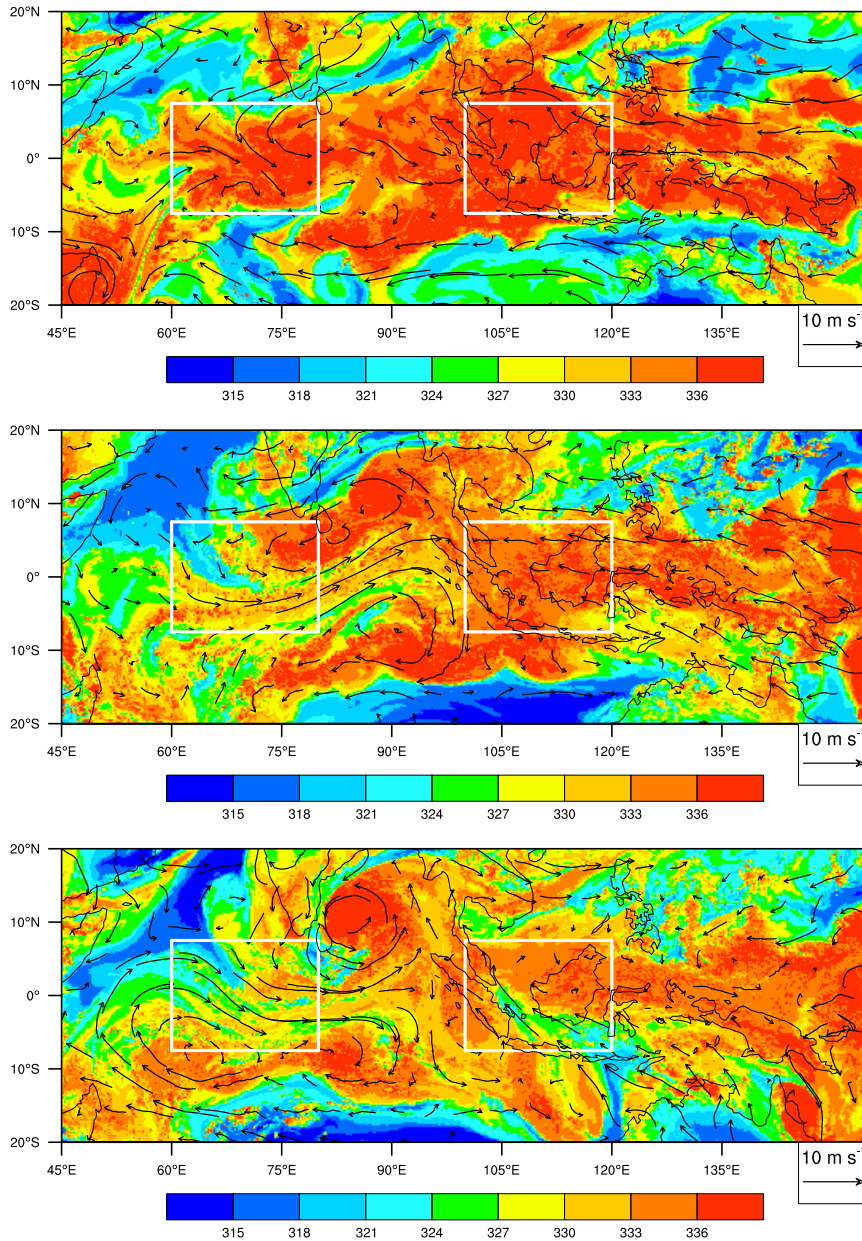


Figure 4.8: As in Fig. 4.1, but for (a): 1800 UTC 6 April 2009, (b): 1800 UTC 11 April 2009, (c): 1800 UTC 14 April 2009.

4.3.3 The MJO event of April 2009

One of the questions for further investigation is whether dry air intrusions are characteristic of the MJO passage and what is the relationship between these intrusions and the suppression of convection. Similar dry air intrusions contributing to the inhibition of convection have been also seen over West Africa (Flaounas et al., 2012) and over the west tropical Pacific during the TOGA COARE campaign (Yoneyama and Parsons, 1999; Parsons et al., 2000). To respond at these questions, a simulation of other MJO episodes would be required. As a preliminary study, the episode of April 2009 can be considered. The simulated evolution of the spatial distribution of θ_e in case of the April 2009 episode is shown in Fig. 4.8. As for the November 2011 episode, the large-scale dry air flows are visible in the northern and southern parts of the simulation domain. The average θ_e also decreases with the MJO passage. In this case, the dry air intrusions are the most pronounced over the Indian Ocean. Nevertheless, they also exist over the Maritime Continent and reach the equatorial zone over the Maritime Continent at 1800 UTC 14 April 2009 (Fig. 4.8c).

Conclusions and perspectives

This work concentrated on the analysis of three MJO episodes — (1) 6–14 April 2009, (2) 23–30 November 2011, and (3) 9–28 February 2013. These episodes were chosen as cases illustrating the MJO activity over the Indian Ocean and the Maritime Continent. The numerical simulations were carried out for a large domain 26.7°S – 26.7°N , 44.6° – 155.4°E by means of the meteorological mesoscale atmospheric model Méso-NH. For every episode, a high-resolution simulation with explicit convection (HiRes, horizontal grid spacing of 4 km) was compared with a low-resolution simulation with parameterized convection (LowRes, horizontal grid spacing of 32 km).

First of all, the capability of Méso-NH to simulate a distinct MJO signal was assessed for both parameterized convection and explicit convection. The simulations were assessed against the TRMM 3B42 rain product and the wind fields from the ECMWF operational analyses. It was found that the simulations with parameterized convection fail to reproduce an eastward-propagating signal in the convective activity and the zonal wind change across the Indian Ocean and the Maritime Continent for any episode. For 2009 and 2011, the convection-permitting simulations show a visible eastward-propagating signal in precipitation accompanied by the low-level zonal wind convergence and upper-level zonal wind divergence. This corresponds to an agreement between the MJO indices

based separately on convection or large-scale circulation. In contrast, the HiRes simulation for the 2013 event fails to reproduce the eastward MJO propagation. This event is characterized by an absence of any propagating zonal wind and a disagreement between the MJO indices.

The spatial distribution and the diurnal cycle of precipitation were analyzed. The spatial distribution of precipitation shows a deficit for the simulated rainfall and the simulations sometimes overestimate the precipitation associated with cyclones. The precipitation distribution in HiRes is fairly well reproduced. The spatial distributions of the maximum of precipitation and the corresponding local solar times are better reproduced by HiRes, LowRes being ahead by several hours. For the average diurnal cycle separately over the Indian Ocean and the land and ocean parts of the Maritime Continent, HiRes and LowRes have a similar quality of the representation as compared to TRMM. The simulated phase has several hours of delay compared to the observations, but the amplitude is correct. The diurnal cycle of precipitation is more pronounced above the land than above the ocean, for both the observations and simulations.

The sensitivity of the convection-permitting simulation to the subgrid-scale cloud fraction parameterization and to the turbulence scheme is examined for the event of 23–30 November 2011. Impacts on the zonal wind, water vapor, precipitation, and relative humidity as well as on the strength of the MJO signal are studied. All HiRes simulations show a strong drying towards the end of the simulation period. The HiRes simulation with the 3D turbulence scheme provides the best results in capturing the MJO passage.

Then, this simulation was used to further investigate the atmospheric overturning over the Indian Ocean for the episode of 2011, which corresponds to the second MJO event observed during the CINDY/DYNAMO/AMIE field campaign. The isentropic analysis (Pauluis and Mrowiec, 2013) was adopted to separate

the ascending air with high equivalent potential temperature from the subsiding air with low equivalent potential temperature. The study focused on two subdomains focusing on the central Indian Ocean and the western part of the Maritime Continent. The isentropic analysis showed the existence of three large-scale convective circulations. The two first circulations are a troposphere deep circulation spanning from the surface to 15 km above the ground level and an overshoot circulation within the tropical tropopause layer. As expected for circulations associated with deep convection, their intensity increases during the active phase of the MJO and decreases during the suppressed phase. The third circulation is characterized by the rising of air masses with low equivalent potential temperature in the low free troposphere and is more pronounced in the case of the Indian Ocean. Its intensity and depth also vary with the MJO activity: this circulation becomes visible and more intensive during the suppressed phase of the MJO. Its development is related to the large-scale dry (relative humidity less than 40%) air intrusions from the subtropical zones into the equatorial band, pointing out a strong drying of the low to middle troposphere during the suppressed phase. This contributes to the further suppression of convection after the passage of the MJO. The diabatic tendencies show an increase during the active MJO phase that is more pronounced over the Indian Ocean than over the Maritime Continent. The entrainment rates generally do not change with the MJO phase but the regions with the larger entrainment extend higher (up to 4 km) during the suppressed MJO phase.

The MJO being a large-scale and complex phenomenon, many questions are remaining unanswered concerning the governing processes of the MJO and the numerical representation of the MJO can still be improved.

The processes contributing to the suppression of convection, also should be further investigated. The dry air intrusions accompanying the MJO

passage in the episode of November 2011, were also described in the CINDY/DYNAMO/AMIE campaign (Kerns and Chen, 2014). Similar dry air intrusions from subtropical band were also present during the TOGA COARE experiment (e.g. Yoneyama and Parsons, 1999). The investigation of more MJO episodes is needed in order to understand the relationship of the MJO propagation with the dry air large-scale flows, to find out if they are common to the MJO passage and to assess their inhibiting role in the development of convection.

The isentropic analysis is shown to be a successful method to study the large-scale atmospheric overturning. While the equivalent potential temperature was demonstrated to be useful for distinguishing the circulations of different type, including the one due to the dry air, it does not allow to separate the mixing from the ice formation and to calculate the entrainment rate above the freezing level. To continue the study, it is also possible to use the liquid moist static energy (Pauluis and Mrowiec, 2013; Dauhut et al., 2017) instead of the equivalent potential temperature as the isentropic coordinate.

Another approximation used in this work was the fixed SST. Another possibility would be to use the SST prescribed by the large-scale analyses, or use the coupling with an ocean model. Even if it was suggested in the literature that the air–ocean interaction is not fundamental to the MJO evolution and the models can simulate a realistic MJO without the coupling with the ocean (Hendon, 2000), it might be possible that taking into account this interaction can influence the results of higher-resolution convection-permitting simulations. Performing the convection-permitting simulations with the air–sea coupling can thus be a potential way to improve the strength of the simulated MJO signal.

Another possible question is the influence of the MJO on tropospheric aerosol. The relationships between aerosols and rainfall are complex and can be influenced by different mechanisms such as low-level wind variability or cloud con-

tamination (Tian et al., 2008). From one side, during the active MJO phase, the precipitation is significantly enhanced which can contribute significantly to the aerosol removal through wet deposition (e.g. Koch et al., 2003; Wilcox and Ramanathan, 2004). At the same time, this is not the only mechanism influencing the aerosol transport over the Indian Ocean. Strong surface winds during convection activity contribute to the increase of sea salt aerosols and thus the properties of aerosols change: while before the active MJO phase, the aerosols are represented mostly by the submicrometer sulfate aerosol originated from continents, afterwards the sea sprays dominate (DeWitt et al., 2013). Thus, it is important to continue the study of the aerosol intraseasonal variability.

With the increasing of the computer power, it would be possible to also perform convection-permitting simulations with even higher resolution than 4 km as well as using LES. Méso-NH model was shown to give a distinct MJO signal in convection-permitting simulations and can be thus successfully used for future investigations of the MJO. The higher-resolution simulations seem very promising for the further investigation of the processes governing the MJO. For example, Takemi (2015) run convection-resolving nested simulations with a 100-m grid resolution for the inner domain. He shows the importance of the interaction of cumulus convection and the atmospheric moistening for the MJO initiation. The cloud-core parcels are not always diluted and can rise to upper levels thus contributing to the moistening of the atmosphere and the development of the MJO.

It would be also interesting to perform simulations with the Méso-NH model in the whole equatorial band and to see if the model is able to propagate the signal in such a large-scale domain. This would also allow to see the change of the MJO strength in different equatorial areas. Also, such simulations would also make easier the quantitative estimation of the MJO signal according to the

MJO diagnostics (Waliser et al., 2009). Indeed, the MJO indices such as RMM are constructed for the whole tropical band (Wheeler and Hendon, 2004). Holloway et al. (2013) proposed a way to calculate the RMM index based on a limited-area domain, but in this method the EOFs and PCs would slightly differ from those obtained for the whole tropical band, which can create potential difficulties for the direct comparison with the observational data or with the results obtained with large-scale models.

Conclusions et perspectives (en français)

Ce travail s'est concentré sur l'analyse de trois épisodes MJO — (1) 6–14 avril 2009, (2) 23–30 novembre 2011, et (3) 9–28 février 2013. Ces épisodes ont été choisis comme des cas illustrant l'activité de la MJO sur l'océan Indien et le continent maritime. Les simulations numériques ont été effectuées pour un grand domaine $26,7^{\circ}\text{S}$ – $26,7^{\circ}\text{N}$, $44,6^{\circ}$ – $155,4^{\circ}\text{E}$ par le modèle atmosphérique Méso-NH. Pour chaque épisode, une simulation haute résolution avec convection explicite (HiRes, espacement horizontal de grille de 4 km) a été comparée à une simulation basse résolution avec convection paramétrée (LowRes, espacement horizontal de grille de 32 km).

Tout d'abord, la capacité de Méso-NH à simuler un signal MJO distinct a été évaluée à la fois pour la convection paramétrée et la convection explicite. Les simulations ont été évaluées par rapport au produit de pluie TRMM 3B42 et aux champs de vent des analyses opérationnelles du Centre européen pour les prévisions météorologiques à moyen terme (European Centre for Medium-Range Weather Forecasts, ECMWF). Il a été constaté que les simulations avec convection paramétrée ne reproduisaient pas la propagation du signal MJO pour la convection et le vent zonal au-dessus de l'océan Indien et du continent mar-

itime. Pour 2009 et 2011, les simulations avec convection explicite ont montré un signal dans les précipitations accompagné de la convergence des vents zonaux à basse altitude et de la divergence des vents zonaux de niveau supérieur. Cela correspond à un accord entre les indices MJO basés séparément sur la convection et sur ceux basés sur la circulation à grande échelle. En revanche, la simulation HiRes pour l'épisode de 2013 n'a pas réussi à reproduire la propagation MJO vers l'est. Cet événement est caractérisé par l'absence de la structure convergence-divergence dans le vent zonal et par un désaccord entre les indices MJO.

La distribution spatiale et le cycle diurne des précipitations ont été analysés. La distribution spatiale des précipitations montre un déficit des précipitations simulées et les simulations surestiment parfois les précipitations associées aux cyclones. La distribution des précipitations dans HiRes est assez bien reproduite. Les distributions spatiales du maximum de précipitations et les heures solaires locales correspondantes sont mieux reproduites par HiRes, LowRes étant en avance de plusieurs heures. Pour le cycle diurne moyenné séparément sur l'océan Indien, les parties terrestres et les parties océaniques du continent maritime, HiRes et LowRes ont une qualité de représentation similaire. La phase du cycle diurne moyenné simulé a plusieurs heures de retard par rapport aux observations, mais l'amplitude est correcte. Le cycle diurne des précipitations est plus prononcé au-dessus de la terre qu'au-dessus de l'océan, tant pour les observations que pour les simulations.

La sensibilité de la simulation avec convection explicite au paramétrisation de la fraction nuageuse d'échelle sous-maille et au schéma de turbulence est examinée pour l'événement du 23 au 30 novembre 2011. Les impacts sur le vent zonal, la vapeur d'eau, la précipitation et l'humidité relative ainsi que sur l'amplitude du signal MJO sont étudiés. Toutes les simulations HiRes montrent un fort assèchement vers la fin de la période de simulation. La simulation HiRes

avec le schéma de turbulence 3D fournit les meilleurs résultats pour reproduire le passage de la MJO.

Ensuite, cette simulation a été utilisée pour étudier la circulation atmosphérique sur l'océan Indien pour l'épisode de 2011, ce qui correspond au deuxième événement MJO observé lors de la campagne CINDY/DYNAMO/AMIE. L'analyse isentropique (Pauluis and Mrowiec, 2013) a été adoptée pour séparer l'air ascendant à forte température potentielle équivalente de l'air subsident à faible température potentielle équivalente. Deux sous-domaines centrés sur l'océan Indien central et la partie occidentale du continent maritime ont été analysés. L'analyse isentropique a montré l'existence de trois circulations convectives de grande échelle. Les deux premières circulations sont une circulation profonde troposphérique qui s'étend de la surface à 15 km au-dessus du niveau du sol et une circulation de percées nuageuses dans la couche de tropopause tropicale. Leur intensité augmente pendant la phase active du MJO et diminue pendant la phase supprimée, ce qui correspond aux propriétés des circulations associées à la convection profonde. La troisième circulation est caractérisée par l'ascendance des masses d'air à faible température potentielle équivalente dans la basse troposphère libre et est plus prononcée dans le cas de l'océan Indien. Son intensité et sa profondeur varient également avec l'activité de la MJO : cette circulation devient plus intense pendant la phase supprimée de la MJO. Son développement est lié aux intrusions d'air sec de grande échelle (humidité relative inférieure à 40%) des zones subtropicales dans la bande équatoriale, indiquant un fort assèchement de la troposphère basse à moyenne pendant la phase supprimée. Ceci contribue à la suppression de la convection après le passage de la MJO. Les tendances diabatiques ont montré une augmentation au cours de la phase active de la MJO qui est plus prononcée sur l'océan Indien que sur le continent maritime. Les taux d'entraînement ne changent généralement pas avec la

phase de la MJO mais les zones avec le plus grand entraînement s'étendent plus haut (jusqu'à 4 km) pendant la phase supprimée de la MJO.

Le MJO étant un phénomène de grande échelle et complexe, de nombreuses questions concernant les mécanismes de la MJO restent sans réponse et la représentation numérique de la MJO peut encore être améliorée.

Les processus contribuant à la suppression de la convection, devraient également être étudiés plus en détail. Les intrusions d'air sec pendant le passage de la MJO en novembre 2011 ont également été trouvées dans la campagne CINDY/DYNAMO/AMIE (Kerns and Chen, 2014). Des intrusions similaires d'air sec provenant de la bande subtropicale étaient également présentes au cours de la campagne TOGA COARE (e.g. Yoneyama and Parsons, 1999). L'étude de plusieurs épisodes MJO est nécessaire pour comprendre la relation entre la propagation de la MJO et les flux d'air sec de grande échelle, pour savoir si leur existence est liée au passage de la MJO et pour évaluer leur rôle inhibiteur dans le développement de la convection.

L'analyse isentropique est une méthode efficace pour étudier la circulation atmosphérique de grande échelle. Si la température potentielle équivalente s'est révélée utile pour distinguer les circulations dans la troposphère, y compris celle due à l'air sec, cette variable ne permet pas de séparer le mélange de la formation de glace et par conséquent, de calculer le taux d'entraînement au-dessus du niveau de congélation. Pour poursuivre cet étude, il est également possible d'utiliser l'énergie statique humide (Pauluis and Mrowiec, 2013; Dauhut et al., 2017) au lieu de la température potentielle équivalente comme coordonnée isentropique.

Une autre approximation utilisée dans ce travail était la température de la surface de mer fixe. Une autre possibilité serait d'utiliser la la température de la surface de mer prescrite par les analyses de grande échelle, ou d'utiliser le cou-

plage avec un modèle océanique. Même s'il a été suggéré dans la littérature que l'interaction air-mer n'est pas fondamentale dans l'évolution de la MJO et que les modèles peuvent simuler une MJO réaliste sans couplage avec l'océan (Hendon, 2000), cette interaction pourrait influencer des résultats de simulations avec convection explicite. Les simulations avec convection explicite et avec le couplage air-mer pourraient donc permettre potentiellement d'améliorer l'amplitude du signal MJO simulé.

Une autre question est l'influence de la MJO sur les aérosols troposphériques. Les relations entre les aérosols et les précipitations sont complexes et peuvent être influencées par différents mécanismes tels que la variabilité du vent à basse altitude ou la contamination des nuages (Tian et al., 2008). D'un côté, pendant la phase active de la MJO les précipitations s'intensifient ce qui peut contribuer de manière significative à l'élimination des aérosols par dépôt humide (e.g. Koch et al., 2003; Wilcox and Ramanathan, 2004). En même temps, ce n'est pas le seul mécanisme qui influence le transport des aérosols au-dessus de l'océan Indien. Les forts vents de surface pendant l'activité de convection contribuent à l'augmentation des particules de sel marin et donc les propriétés des aérosols changent : alors qu'avant la phase active de la MJO, les aérosols sont principalement représentés par les particules submicrométriques de sulfate provenant des continents, plus tard ce sont les sels marins qui dominant (DeWitt et al., 2013). Ainsi, il est important de poursuivre l'étude de la variabilité intra-saisonnière prenant en compte des aérosols.

Avec l'augmentation de la capacité du calcul haute performance, il serait également possible d'effectuer des simulations permettant la convection avec une résolution encore plus fine que 4 km ainsi que d'utiliser la LES. Il a été montré que le modèle Méso-NH donne un signal MJO distinct dans les simulations avec convection explicite et peut donc être utilisé avec succès pour des études de

la MJO. Les simulations à plus haute résolution semblent très prometteuses pour la poursuite de l'étude des mécanismes de la MJO. Par exemple, Takemi (2015) a réalisé des simulations imbriquées à convection explicite avec un espacement de grille de 100 m pour le domaine intérieur. Il montre l'importance de l'interaction de la convection et de l'humidification atmosphérique pour l'initiation de la MJO. Les masses d'air ne sont pas toujours diluées et peuvent atteindre les niveaux supérieurs, contribuant ainsi à l'humidification de l'atmosphère et au développement de la MJO.

Il serait également intéressant d'effectuer des simulations avec le modèle Méso-NH dans toute la bande équatoriale et de voir si le modèle est capable de reproduire le signal MJO dans un tel domaine. Cela permettrait également de voir le changement de l'amplitude de la MJO pendant son passage autour de la Terre. De plus, ces simulations faciliteraient également l'estimation quantitative du signal MJO avec les diagnostics de la MJO (Waliser et al., 2009). En effet, les indices MJO tels que RMM sont calculés pour toute la bande tropicale (Wheeler and Hendon, 2004). Holloway et al. (2013) ont proposé une méthode pour calculer l'indice RMM sur un domaine limité, mais dans cette méthode, les EOF et les PC diffèrent légèrement de ceux calculés pour toute la bande tropicale. Cela pourrait créer des difficultés pour la comparaison directe des simulations avec les données des observations ou avec les résultats obtenus avec les modèles de grande échelle.

Bibliography

- Abdel-Lathif, A. Y., R. Roehrig, I. Beau, and H. Douville, 2018: Single-column modeling of convection during the CINDY2011/DYNAMO field campaign with the CNRM climate model version 6. *J. Adv. Model. Earth Syst.*, **10** (3), 578–602, doi:10.1002/2017MS001077.
- Adames, A. F., and D. Kim, 2016: The MJO as a dispersive, convectively coupled moisture wave: Theory and observations. *J. Atmos. Sci.*, **73** (3), 913–941, doi:10.1175/JAS-D-15-0170.1.
- Bechtold, P., E. Bazile, F. Guichard, P. Mascart, and E. Richard, 2001: A mass flux convection scheme for regional and global models. *Quart. J. Roy. Meteor. Soc.*, **127**, 869–886, doi:10.1002/qj.4971275730.
- Bechtold, P., M. Köhler, T. Jung, F. Doblas-Reyes, M. Leutbecher, M. J. Rodwell, F. Vitart, and G. Balsamo, 2008: Advances in simulating atmospheric variability with the ECMWF model: From synoptic to decadal time-scales. *Quart. J. Roy. Meteor. Soc.*, **134** (634), 1337–1351, doi:10.1002/qj.289.
- Belamari, S., and A. Pirani, 2007: *Validation of the optimal heat and momentum fluxes using the ORCA2-LIM global ocean-ice model*. Marine Environment and Security for the European Area-Integrated Project (MERSEA IP) Deliverable D4.1.3, 88 pp.
- Bellenger, H., and J. P. Duvel, 2012: The event-to-event variability of the boreal winter MJO. *Geophys. Res. Lett.*, **39** (8), L08 701, doi:10.1029/2012GL051294.
- Benedict, J. J., and D. A. Randall, 2007: Observed characteristics of the MJO relative to maximum rainfall. *J. Atmos. Sci.*, **64**, 2332–2354, doi:10.1175/JAS3968.1.
- Benedict, J. J., and D. A. Randall, 2009: Structure of the Madden–Julian oscillation in the superparameterized CAM. *J. Atmos. Sci.*, **66**, 3277–3296, doi:10.1175/2009JAS3030.1.

- Bladé, I., and D. L. Hartmann, 1993: Tropical intraseasonal oscillations in a simple nonlinear model. *J. Atmos. Sci.*, **50** (17), 2922–2939, doi:10.1175/1520-0469(1993)050<2922:TIOIAS>2.0.CO;2.
- Bougeault, P., and P. Lacarrère, 1989: Parameterization of orographic induced turbulence in a mesobetascale model. *Mon. Wea. Rev.*, **117**, 1872–1890, doi:10.1175/1520-0493(1989)117<1872:POOITI>2.0.CO;2.
- Brockhaus, P., D. Lüthi, and C. Schär, 2008: Aspects of the diurnal cycle in a regional climate model. *Meteorologische Zeitschrift*, **17** (4), 433–443, doi:10.1127/0941-2948/2008/0316.
- Cassou, C., 2008: Intraseasonal interaction between the Madden–Julian Oscillation and the North Atlantic Oscillation. *Nature*, **455**, 523–527, doi:10.1038/nature07286.
- Chaboureau, J.-P., and P. Bechtold, 2005: Statistical representation of clouds in a regional model and the impact on the diurnal cycle of convection during Tropical Convection, Cirrus and Nitrogen Oxides (TROCCINOX). *J. Geophys. Res.*, **110**, D17 103, doi:10.1029/2004JD005645.
- Chen, S. S., R. A. Houze, and B. E. Mapes, 1996: Multiscale variability of deep convection in relation to large-scale circulation in TOGA COARE. *J. Atmos. Sci.*, **53** (10), 1380–1409, doi:10.1175/1520-0469(1996)053<1380:MVODCI>2.0.CO;2.
- Chen, X., O. M. Pauluis, and F. Zhang, 2018: Atmospheric overturning across multiple scales of an MJO event during the CINDY/DYNAMO campaign. *J. Atmos. Sci.*, **75**, 381–399, doi:10.1175/JAS-D-17-0060.1.
- Chen, Y., and A. D. Del Genio, 2009: Evaluation of tropical cloud regimes in observations and a general circulation model. *Climate Dyn.*, **32**, 355–369.
- Chikira, M., 2010: A cumulus parameterization with state-dependent entrainment rate: Part II. Impact on climatology in a general circulation model. *J. Atmos. Sci.*, **67** (7), 2194–2211.
- Christensen, H. M., A. Dawson, and C. E. Holloway, 2018: Forcing single-column models using high-resolution model simulations. *J. Adv. Model. Earth Syst.*, **10** (8), 1833–1857, doi:10.1029/2017MS001189.

- Cuxart, J., P. Bougeault, and J.-L. Redelsperger, 2000: A turbulence scheme allowing for mesoscale and large-eddy simulations. *Quart. J. Roy. Meteor. Soc.*, **126**, 1–30, doi:10.1002/qj.497126562022.
- Dauhut, T., J.-P. Chaboureau, P. Mascart, and O. Pauluis, 2017: The atmospheric overturning induced by Hector the Convecton. *J. Atmos. Sci.*, **74(10)**, 3271–3284, doi:10.1175/JAS-D-17-0035.1.
- Deardorff, J. W., 1980: Stratocumulus-capped mixed layers derived from a three-dimensional model. *Bound. Layer Meteor.*, **18 (4)**, 495–527, doi:10.1007/BF00119502.
- Del Genio, A. D., Y. Chen, D. Kim, and M.-S. Yao, 2012: The MJO transition from shallow to deep convection in CloudSat/CALIPSO data and GISS GCM simulations. *J. Climate*, **25 (11)**, 3755–3770, doi:10.1175/JCLI-D-11-00384.1.
- Déqué, M., and Coauthors, 2007: An intercomparison of regional climate simulations for Europe: Assessing uncertainties in model projections. *Clim. Change*, **81 (1)**, 53–70.
- DeWitt, H. L., D. J. Coffman, K. J. Schulz, W. A. Brewer, T. S. Bates, and P. K. Quinn, 2013: Atmospheric aerosol properties over the equatorial Indian Ocean and the impact of the Madden–Julian oscillation. *Journal of Geophysical Research: Atmospheres*, **118 (11)**, 5736–5749, doi:10.1002/jgrd.50419.
- Donald, A., H. Meinke, B. Power, A. d. H. N. Maia, M. C. Wheeler, N. White, R. C. Stone, and J. Ribbe, 2006: Near-global impact of the Madden–Julian oscillation on rainfall. *Geophys. Res. Lett.*, **33 (9)**, L09 704, doi:10.1029/2005GL025155.
- Done, J., C. A. Davis, and M. Weisman, 2004: The next generation of NWP: explicit forecasts of convection using the weather research and forecasting (WRF) model. *Atmos. Sci. Lett.*, **5 (6)**, 110–117, doi:10.1002/asl.72.
- Duvel, J.-P., 2015: Initiation and intensification of tropical depressions over the southern Indian Ocean: Influence of the MJO. *Mon. Wea. Rev.*, **143 (6)**, 2170–2191, doi:10.1175/MWR-D-14-00318.1.
- Ellingson, R. G., J. Ellis, and F. S., 1991: The intercomparison of radiation codes used in climate models: Long wave results. *J. Geophys. Res.*, **96 (D5)**, 8929–8953.

- Emanuel, K. A., 1987: An air–sea interaction model of intraseasonal oscillations in the tropics. *J. Atmos. Sci.*, **44** (16), 2324–2340, doi:10.1175/1520-0469(1987)044<2324:AASIMO>2.0.CO;2.
- Flaounas, E., S. Janicot, S. Bastin, and R. Roca, 2012: The West African monsoon onset in 2006: Sensitivity to surface albedo, orography, SST and synoptic scale dry-air intrusions using WRF. *Climate Dyn.*, **38** (3), 685–708, doi:10.1007/s00382-011-1255-2.
- Flatau, M., P. J. Flatau, P. Phoebus, and P. P. Niiler, 1997: The feedback between equatorial convection and local radiative and evaporative processes: The implications for intraseasonal oscillations. *J. Atmos. Sci.*, **54** (19), 2373–2386, doi:10.1175/1520-0469(1997)054<2373:TFBECA>2.0.CO;2.
- Fouquart, Y., and B. Bonnel, 1986: Computations of solar heating of the Earth’s atmosphere: A new parametrization. *Beitr. Phys. Atmos.*, **53**, 35–62.
- Gaspar, P., Y. Grégoris, and J.-M. Lefevre, 1990: A simple eddy kinetic energy model for simulations of the oceanic vertical mixing: Tests at station Papa and long-term upper ocean study site. *J. Geophys. Res.*, **95**, 16 179–16 193, doi:10.1029/JC095iC09p16179.
- Godfrey, J. S., R. A. Houze Jr., R. H. Johnson, R. Lukas, J.-L. Redelsperger, A. Sumi, and R. Weller, 1998: Coupled ocean-atmosphere response experiment (COARE): An interim report. *Journal of Geophysical Research: Oceans*, **103** (C7), 14 395–14 450, doi:10.1029/97JC03120.
- Goswami, B. N., 2005: *South Asian monsoon*. In: *Intraseasonal Variability in the Atmosphere–Ocean Climate System*, 19–61. Springer Praxis Books (Environmental Sciences). Springer, Berlin, Heidelberg, doi:10.1007/3-540-27250-X_10.
- Grabowski, W. W., 2003: MJO-like coherent structures: Sensitivity simulations using the cloud-resolving convection parameterization (CRCP). *J. Atmos. Sci.*, **60** (6), 847–864, doi:10.1175/1520-0469(2003)060<0847:MLCSSS>2.0.CO;2.
- Hagos, S., and L. R. Leung, 2011: Moist thermodynamics of the Madden–Julian oscillation in a cloud-resolving simulation. *J. Climate*, **24** (21), 5571–5583, doi:10.1175/2011JCLI4212.1.
- Hagos, S., L. R. Leung, and J. Dudhia, 2011: Thermodynamics of the Madden–Julian oscillation in a regional model with constrained moisture. *J. Atmos. Sci.*, **68**, 1974–1989, doi:10.1175/2011JAS3592.1.

- Henderson, G. R., B. S. Barrett, and D. M. Lafleur, 2014: Arctic sea ice and the Madden–Julian oscillation (MJO). *Climate Dyn.*, **43** (7), 2185–2196, doi:10.1007/s00382-013-2043-y.
- Henderson-Sellers, A., Z. Yang, and R. Dickinson, 1993: The project for intercomparison of land-surface parameterization schemes. *Bull. Amer. Meteor. Soc.*, **74** (7), 1335–1349.
- Hendon, H. H., 2000: Impact of air–sea coupling on the Madden–Julian oscillation in a general circulation model. *J. Atmos. Sci.*, **57** (24), 3939–3952, doi:10.1175/1520-0469(2001)058<3939:IOASCO>2.0.CO;2.
- Hendon, H. H., and M. L. Salby, 1994: The life cycle of the Madden–Julian oscillation. *J. Atmos. Sci.*, **51**, 2225–2237.
- Hendon, H. H., C. Zhang, and J. D. Glick, 1999: Interannual variation of the Madden–Julian oscillation during austral summer. *J. Climate*, **12**, 2538–2550.
- Higgins, R. W., J.-K. E. Schemm, W. Shi, and A. Leetmaa, 2000: Extreme precipitation events in the western United States related to tropical forcing. *J. Climate*, **13** (4), 793–820, doi:10.1175/1520-0442(2000)013<0793:EPEITW>2.0.CO;2.
- Holloway, C. E., S. J. Woolnough, and G. M. S. Lister, 2013: The effects of explicit versus parameterized convection on the MJO in a large-domain high-resolution tropical case study. Part I: Characterization of large-scale organization and propagation. *J. Atmos. Sci.*, **70**, 1342–1369, doi:10.1175/JAS-D-12-0227.1.
- Holloway, C. E., S. J. Woolnough, and G. M. S. Lister, 2015: The effects of explicit versus parameterized convection on the MJO in a large-domain high-resolution tropical case study. Part II: Processes leading to differences in MJO development. *J. Atmos. Sci.*, **72**, 2719–2743, doi:10.1175/JAS-D-14-0308.1.
- Hsu, H.-H., B. J. Hoskins, and F.-F. Jin, 1990: The 1985/86 intraseasonal oscillation and the role of the extratropics. *J. Atmos. Sci.*, **47** (7), 823–839, doi:10.1175/1520-0469(1990)047<0823:TIOATR>2.0.CO;2.
- Hu, Q., and D. A. Randall, 1994: Low-frequency oscillations in radiative-convective systems. *J. Atmos. Sci.*, **51** (8), 1089–1099, doi:10.1175/1520-0469(1994)051<1089:LFOIRC>2.0.CO;2.

- Hu, Q., and D. A. Randall, 1995: Low-frequency oscillations in radiative-convective systems. Part II: An idealized model. *J. Atmos. Sci.*, **52** (4), 478–490, doi:10.1175/1520-0469(1995)052<0478:LFOIRC>2.0.CO;2.
- Huffman, G. J., and Coauthors, 2007: The TRMM Multisatellite Precipitation Analysis (TMPA): Quasi-global, multiyear, combined-sensor precipitation estimates at fine scales. *J. Hydrometeor.*, **8**, 38–55, doi:10.1175/JHM560.1.
- Johnson, R. H., and P. E. Ciesielski, 2013: Structure and properties of Madden–Julian oscillations deduced from DYNAMO sounding arrays. *J. Atmos. Sci.*, **70** (10), 3157–3179, doi:10.1175/JAS-D-13-065.1.
- Kalnay, E., and Coauthors, 1996: The NCEP/NCAR 40-year reanalysis project. *Bull. Amer. Meteor. Soc.*, **77** (3), 437–470, doi:10.1175/1520-0477(1996)077<0437:TNYRP>2.0.CO;2.
- Kapur, A., C. Zhang, J. Zavala-Garay, and H. H. Hendon, 2012: Role of stochastic forcing in ENSO in observations and a coupled GCM. *Climate Dyn.*, **38** (1), 87–107, doi:10.1007/s00382-011-1070-9.
- Katsumata, M., R. H. Johnson, and P. E. Ciesielski, 2009: Observed synoptic-scale variability during the developing phase of an ISO over the Indian Ocean during MISMO. *J. Atmos. Sci.*, **66** (11), 3434–3448, doi:10.1175/2009JAS3003.1.
- Kemball-Cook, S. R., and B. C. Weare, 2001: The onset of convection in the Madden–Julian oscillation. *J. Climate*, **14**, 780–793.
- Kerns, B., and S. Chen, 2014: Equatorial dry air intrusion and related synoptic variability in MJO initiation during DYNAMO. *Mon. Wea. Rev.*, **142**, 1326–1343, doi:10.1175/MWR-D-13-00159.1.
- Kerns, B. W., and S. S. Chen, 2016: Large-scale precipitation tracking and the MJO over the Maritime Continent and Indo-Pacific warm pool. *J. Geophys. Res. Atmos.*, **121**, 8755–8776, doi:10.1002/2015JD024661.
- Khairoutdinov, M., D. Randall, and C. DeMott, 2005: Simulations of the atmospheric general circulation using a cloud-resolving model as a superparameterization of physical processes. *J. Atmos. Sci.*, **62** (7), 2136–2154, doi:10.1175/JAS3453.1.

- Kiladis, G. N., J. Dias, K. H. Straub, M. C. Wheeler, S. N. Tulich, K. Kikuchi, K. M. Weickmann, and V. M. J., 2014: A comparison of OLR and circulation-based indices for tracking the MJO. *Mon. Wea. Rev.*, **142**, 1697–1715, doi:10.1175/MWR-D-13-00301.1.
- Kiladis, G. N., K. H. Straub, G. C. Reid, and K. S. Gage, 2001: Aspects of interannual and intraseasonal variability of the tropopause and lower stratosphere. *Quart. J. Roy. Meteor. Soc.*, **127 (576)**, 1961–1983, doi:10.1002/qj.49712757606.
- Kim, D., A. H. Sobel, E. D. Maloney, D. M. W. Frierson, and I.-S. Kang, 2011: A systematic relationship between intraseasonal variability and mean state bias in AGCM simulations. *J. Climate*, **24 (21)**, 5506–5520, doi:10.1175/2011JCLI4177.1.
- Klotzbach, P. J., 2014: The Madden–Julian oscillation’s impacts on worldwide tropical cyclone activity. *J. Climate*, **27 (6)**, 2317–2330, doi:10.1175/JCLI-D-13-00483.1.
- Knutson, T. R., and K. M. Weickmann, 1987: 30–60 day atmospheric oscillations: Composite life cycles of convection and circulation anomalies. *Mon. Wea. Rev.*, **115**, 1407–1436.
- Knutson, T. R., K. M. Weickmann, and J. E. Kutzbach, 1986: Global-scale intraseasonal oscillations of Outgoing Longwave Radiation and 250 mb zonal wind during Northern Hemisphere summer. *Mon. Wea. Rev.*, **114 (3)**, 605–623, doi:10.1175/1520-0493(1986)114<0605:GSIOOO>2.0.CO;2.
- Koch, D., J. Park, and A. Del Genio, 2003: Clouds and sulfate are anticorrelated: A new diagnostic for global sulfur models. *Journal of Geophysical Research: Atmospheres*, **108 (D24)**, 4781, doi:10.1029/2003JD003621.
- Krishnamurti, T. N., and D. Subrahmanyam, 1982: The 30–50 day mode at 850 mb during MONEX. *J. Atmos. Sci.*, **39 (9)**, 2088–2095, doi:10.1175/1520-0469(1982)039<2088:TDMAMD>2.0.CO;2.
- Lac, C., and Coauthors, 2018: Overview of the Meso-NH model version 5.4 and its applications. *Geosci. Model Dev. Discuss.*, **11**, 1929–1969, doi:10.5194/gmd-11-1929-2018.
- Lafore, J.-P., and Coauthors, 1998: The Méso-NH atmospheric simulation system. Part I: adiabatic formulation and control simulations. *Ann. Geophys.*, **16**, 90–109, doi:10.1007/s00585-997-0090-6.

- Lau, K.-M., and L. Peng, 1987: Origin of low-frequency (intraseasonal) oscillations in the tropical atmosphere. Part I: Basic theory. *J. Atmos. Sci.*, **44** (6), 950–972, doi:10.1175/1520-0469(1987)044<0950:OOLFOI>2.0.CO;2.
- Lau, K.-M., P.-J. Sheu, and I.-S. Kang, 1994: Multiscale low-frequency circulation modes in the global atmosphere. *J. Atmos. Sci.*, **51** (9), 1169–1193, doi:10.1175/1520-0469(1994)051<1169:MLFCMI>2.0.CO;2.
- Lean, H. W., P. A. Clark, M. Dixon, N. M. Roberts, A. Fitch, R. Forbes, and C. Halliwell, 2008: Characteristics of high-resolution versions of the Met Office Unified Model for forecasting convection over the United Kingdom. *Mon. Wea. Rev.*, **136** (9), 3408–3424, doi:10.1175/2008MWR2332.1.
- L'Heureux, M. L., and R. W. Higgins, 2008: Boreal winter links between the Madden–Julian oscillation and the Arctic Oscillation. *J. Climate*, **21** (12), 3040–3050, doi:10.1175/2007JCLI1955.1.
- Li, T., L. Wang, M. Peng, B. Wang, C. Zhang, W. Lau, and H.-C. Kuo, 2018: A paper on the tropical intraseasonal oscillation published in 1963 in a Chinese journal. *Bull. Amer. Meteor. Soc.*, **99** (9), 1765–1779, doi:10.1175/BAMS-D-17-0216.1.
- Liebmann, B., H. H. Hendon, and J. D. Glick, 1994: The relationship between tropical cyclones of the Western Pacific and Indian oceans and the Madden–Julian oscillation. *Bull. Amer. Meteor. Soc.*, **77**, 1275–1277.
- Lin, J.-L., and Coauthors, 2006: Tropical intraseasonal variability in 14 IPCC AR4 climate models. Part I: Convective signals. *J. Climate*, **19** (12), 2665–2690, doi:10.1175/JCLI3735.1.
- Lin, J. W.-B., J. D. Neelin, and N. Zeng, 2000: Maintenance of tropical intraseasonal variability: Impact of evaporation–wind feedback and midlatitude storms. *J. Atmos. Sci.*, **57** (17), 2793–2823, doi:10.1175/1520-0469(2000)057<2793:MOTIVI>2.0.CO;2.
- Lin, X., and R. Johnson, 1996: Kinematic and thermodynamic characteristics of the flow over the Western Pacific warm pool during TOGA COARE. *J. Atmos. Sci.*, **53** (5), 695–715, doi:10.1175/1520-0469(1996)053<0695:KATCOT>2.0.CO;2.

- Ling, J., P. Bauer, P. Bechtold, A. Beljaars, R. Forbes, F. Vitart, M. Ulate, and C. D. Zhang, 2014: Global versus local MJO forecast skill of the ECMWF model during DYNAMO. *Mon. Wea. Rev.*, **142**, 2228–2247, doi:10.1175/MWR-D-13-00292.
- Ling, J., C. Li, and X. Jia, 2009: Impacts of cumulus momentum transport on MJO simulation. *Adv. Atmos. Sci.*, **26** (5), 864–876, doi:10.1007/s00376-009-8016-8.
- Liu, P., and Coauthors, 2009: An MJO simulated by the NICAM at 14- and 7-km resolutions. *Mon. Wea. Rev.*, **137** (10), 3254–3268, doi:10.1175/2009MWR2965.1.
- Lo, F., and H. H. Hendon, 2000: Empirical extended-range prediction of the Madden–Julian oscillation. *Mon. Wea. Rev.*, **128**, 2528–2543.
- Lorenc, A. C., 1984: The evolution of planetary-scale 200 mb divergent flow during the FGGE year. *Quart. J. Roy. Meteor. Soc.*, **110** (464), 427–441, doi:10.1002/qj.49711046408.
- Machado, L. A. T., and J.-P. Chaboureaud, 2015: Effect of turbulence parameterization on assessment of cloud organization. *Mon. Wea. Rev.*, **143**, 3246–3262, doi:10.1175/MWR-D-14-00393.1.
- Madden, R., and P. Julian, 1971: Detection of a 40–50 day oscillation in the zonal wind in the tropical Pacific. *J. Atmos. Sci.*, **28**, 702–708.
- Madden, R., and P. Julian, 1972: Description of global-scale circulation cells in the tropics with a 40–50 day period. *J. Atmos. Sci.*, **29**, 1109–1123.
- Maloney, E. D., and A. H. Sobel, 2004: Surface fluxes and ocean coupling in the tropical intraseasonal oscillation. *J. Climate*, **17** (22), 4368–4386, doi:10.1175/JCLI-3212.1.
- Masson, V., 2000: A physically-based scheme for the urban energy budget in atmospheric models. *Bound. Layer. Meteor.*, **94**, 357–397.
- Masson, V., J.-L. Champeaux, F. Chauvin, C. Meriguet, and R. Lacaze, 2003: A global database of land surface parameters at 1-km resolution in meteorological and climate models. *J. Climate*, **16**(9), 1261–1282.
- Masson, V., and Coauthors, 2013: The SURFEXv7.2 land and ocean surface platform for coupled or offline simulation of Earth surface variables and fluxes. *Geosci. Model Dev.*, **6**, 929–960, doi:10.5194/gmd-6-929-2013.

- Matsuno, T., 1966: Quasi-geostrophic motions in the equatorial area. *J. Meteor. Soc. Japan*, **44** (1), 25–43, doi:10.2151/jmsj1965.44.1_25.
- Matthews, A. J., 2008: Primary and successive events in the Madden–Julian oscillation. *Quart. J. Roy. Meteor. Soc.*, **134**, 439–453, doi:10.1002/qj.224.
- Matthews, A. J., B. J. Hoskins, J. M. Slingo, and M. Blackburn, 1996: Development of convection along the SPCZ within a Madden–Julian oscillation. *Quart. J. Roy. Meteor. Soc.*, **122** (531), 669–688, doi:10.1002/qj.49712253106.
- Matthews, A. J., and G. N. Kiladis, 1999: The tropical–extratropical interaction between high-frequency transients and the Madden–Julian oscillation. *Mon. Wea. Rev.*, **127**, 661–677.
- Matthews, A. J., and M. P. Meredith, 2004: Variability of Antarctic circumpolar transport and the Southern Annular Mode associated with the Madden–Julian Oscillation. *Geophys. Res. Lett.*, **31** (24), L24312, doi:10.1029/2004GL021666.
- Meetoo, C. C., 2014: Tropical cyclogenesis conditions in the Southwestern Indian Ocean. Phd dissertation, Université Toulouse III Paul Sabatier, URL <https://tel.archives-ouvertes.fr/tel-01128104>.
- Mesinger, F., and A. Arakawa, 1976: *Numerical methods used in atmospheric models*, GARP publications series No. 17, Vol. 1. World Meteorological Organization, International Council of Scientific Unions, 64 pp.
- Mironov, D., E. Heise, E. Kourzeneva, B. Ritter, N. Schneider, and A. Terzhevik, 2010: Implementation of the lake parameterisation scheme FLake into the numerical weather prediction model COSMO. *Boreal Environ. Res.*, **15**, 218–230.
- Mlawer, E. J., S. J. Taubman, P. D. Brown, M. J. Iacono, and S. A. Clough, 1997: Radiative transfer for inhomogeneous atmospheres: RRTM, a validated correlated-k model for the longwave. *J. Geophys. Res.*, **102**, 16 663–16 682, doi:10.1029/97JD00237.
- Moore, A. M., and R. Kleeman, 1999: Stochastic forcing of ENSO by the intraseasonal oscillation. *J. Climate*, **12** (5), 1199–1220, doi:10.1175/1520-0442(1999)012<1199:SFOEBT>2.0.CO;2.

- Myers, D. S., and D. E. Waliser, 2003: Three-dimensional water vapor and cloud variations associated with the Madden–Julian oscillation during Northern Hemisphere winter. *J. Climate*, **16** (6), 929–950, doi:10.1175/1520-0442(2003)016<0929:TDWVAC>2.0.CO;2.
- Nakazawa, T., 1988: Tropical super clusters within intraseasonal variations over the western Pacific. *J. Meteor. Soc. Japan*, **66**, 823–836.
- Neale, R., and J. Slingo, 2003: The Maritime Continent and its role in the global climate: A GCM study. *J. Climate*, **16** (5), 834–848, doi:10.1175/1520-0442(2003)016<0834:TMCAIR>2.0.CO;2.
- Neelin, J. D., I. M. Held, and K. H. Cook, 1987: Evaporation–wind feedback and low-frequency variability in the tropical atmosphere. *J. Atmos. Sci.*, **44** (16), 2341–2348, doi:10.1175/1520-0469(1987)044<2341:EWFALF>2.0.CO;2.
- Noilhan, J., and S. Planton, 1989: A simple parameterization of land surface processes for meteorological models. *Mon. Wea. Rev.*, **117**, 536–549.
- Pai, D. S., J. Bhate, O. P. Sreejith, and H. R. Hatwar, 2011: Impact of MJO on the intraseasonal variation of summer monsoon rainfall over India. *Climate Dyn.*, **36** (1), 41–55, doi:10.1007/s00382-009-0634-4.
- Pantillon, F., P. Mascart, J.-P. Chaboureau, C. Lac, J. Escobar, and J. Duron, 2011: Seamless Meso-NH modeling over very large grids. *C. R. Mecanique*, **339**, 136–140, doi:10.1016/j.crme.2010.12.002.
- Parsons, D. B., K. Yoneyama, and J.-L. Redelsperger, 2000: The evolution of the tropical western Pacific atmosphere–ocean system following the arrival of a dry intrusion. *Quart. J. Roy. Meteor. Soc.*, **126** (563), 517–548, doi:10.1002/qj.49712656307.
- Pauluis, O. M., and A. A. Mrowiec, 2013: Isentropic analysis of convective motions. *J. Atmos. Sci.*, **70**, 3673–3688, doi:10.1175/JAS-D-12-0205.1.
- Peatman, S. C., A. J. Matthews, and D. P. Stevens, 2015: Propagation of the Madden–Julian oscillation and scale interaction with the diurnal cycle in a high-resolution GCM. *Climate Dyn.*, **45** (9), 2901–2918, doi:10.1007/s00382-015-2513-5.

- Pedersen, C. A., and J.-G. Winther, 2005: Intercomparison and validation of snow albedo parameterization schemes in climate models. *Climate Dyn.*, **25** (4), 351–362.
- Pergaud, J., V. Masson, S. Malardel, and F. Couvreur, 2009: A parameterization of dry thermals and shallow cumuli for mesoscale numerical weather prediction. *Bound. Layer. Meteor.*, **132**, 83–106, doi:10.1007/s10546-009-9388-0.
- Pinty, J.-P., and P. Jabouille, 1998: A mixed-phase cloud parameterization for use in a mesoscale non-hydrostatic model: Simulations of a squall line and of orographic precipitations. *Conf. on cloud physics, Everett, WA, Amer. Meteor. Soc.*, 217–220.
- Poehl, B., and A. J. Matthews, 2007: Observed changes in the lifetime and amplitude of the Madden–Julian oscillation with interannual ENSO sea surface temperature anomalies. *J. Climate*, **20**, 2659–2674.
- Prein, A. F., and Coauthors, 2015: A review on regional convection-permitting climate modeling: Demonstrations, prospects, and challenges. *Rev. Geophys.*, **53**, 323–361, doi:10.1002/2014RG000475.
- Ramage, C. S., 1968: Role of a tropical “maritime continent” in the atmospheric circulation. *Mon. Wea. Rev.*, **96** (6), 365–370.
- Raymond, D. J., and v. Fuchs, 2009: Moisture modes and the Madden–Julian oscillation. *J. Climate*, **22** (11), 3031–3046, doi:10.1175/2008JCLI2739.1.
- Reinares Martínez, I., and J.-P. Chaboureau, 2018: Precipitation and mesoscale convective systems: Explicit versus parameterized convection over Northern Africa. *Mon. Wea. Rev.*, **146**, 797–812, doi:10.1175/MWR-D-17-0202.1.
- Risi, C., and J.-P. Duvel, 2014: L’oscillation de Madden–Julian, principal mode de variabilité intrasaisonnière dans les tropiques. *La Météorologie*, **86**, 57–65, doi:10.4267/2042/54074.
- Rui, H., and B. Wang, 1990: Development characteristics and dynamic structure of tropical intraseasonal convection anomalies. *J. Atmos. Sci.*, **47**, 357–379.
- Salby, M. L., and R. R. Garcia, 1987: Transient response to localized episodic heating in the tropics. Part I: Excitation and short-time near-field behavior. *J. Atmos. Sci.*, **44** (2), 458–498, doi:10.1175/1520-0469(1987)044<0458:TRTLEH>2.0.CO;2.

- Shinoda, T., and H. H. Hendon, 1998: Mixed layer modeling of intraseasonal variability in the tropical western Pacific and Indian Oceans. *J. Climate*, **11** (10), 2668–2685, doi:10.1175/1520-0442(1998)011<2668:MLMOIV>2.0.CO;2.
- Simpson, J., C. Kummerow, W.-K. Tao, and R. F. Adler, 1996: On the Tropical Rainfall Measuring Mission (TRMM). *Meteorol. Atmos. Phys.*, **60** (1-3), 19–36, doi:10.1007/BF01029783.
- Slingo, J. M., and Coauthors, 1996: Intraseasonal oscillations in 15 atmospheric general circulation models: Results from an AMIP diagnostic subproject. *Climate Dyn.*, **12** (5), 325–357, doi:10.1007/BF00231106.
- Sobel, A., and E. Maloney, 2013: Moisture modes and the eastward propagation of the MJO. *J. Atmos. Sci.*, **70** (1), 187–192, doi:10.1175/JAS-D-12-0189.1.
- Song, X., and G. J. Zhang, 2009: Convection parameterization, tropical pacific double ITCZ, and upper-ocean biases in the NCAR CCSM3: Part I. Climatology and atmospheric feedback. *J. Climate*, **22** (16), 4299–4315.
- Straub, K. H., 2013: MJO initiation in the Real-Time Multivariate MJO Index. *J. Climate*, **26** (4), 1130–1151, doi:10.1175/JCLI-D-12-00074.1.
- Subramanian, A. C., and G. J. Zhang, 2014: Diagnosing MJO hindcast biases in NCAR CAM3 using nudging during the DYNAMO field campaign. *J. Geophys. Res. Atmos.*, **119** (12), 7231–7253, doi:10.1002/2013JD021370.
- Takemi, T., 2015: Relationship between cumulus activity and environmental moisture during the CINDY2011/DYNAMO field experiment as revealed from convection-resolving simulations. *J. Meteor. Soc. Japan*, **93A**, 41–58, doi:10.2151/jmsj.2015-035.
- Tian, B., and Coauthors, 2008: Does the Madden–Julian oscillation influence aerosol variability? *Journal of Geophysical Research: Atmospheres*, **113**, D12 215, doi:10.1029/2007JD009372.
- Tromeur, E., and W. B. Rossow, 2010: Interaction of deep tropical convection with the large-scale circulation in the MJO. *J. Climate*, **23**, 1837–1853.
- Ventrice, M. J., M. C. Wheeler, H. H. Hendon, C. J. Schreck III, C. D. Thorncroft, and G. N. Kiladis, 2013: A modified multivariate Madden–Julian oscillation index using velocity potential. *Mon. Wea. Rev.*, **141**, 4197–4120.

- Virts, K. S., and J. M. Wallace, 2010: Annual, interannual, and intraseasonal variability of tropical tropopause transition layer cirrus. *J. Atmos. Sci.*, **67** (10), 3097–3112, doi:10.1175/2010JAS3413.1.
- Virts, K. S., J. M. Wallace, Q. Fu, and T. P. Ackerman, 2010: Tropical tropopause transition layer cirrus as represented by calipso lidar observations. *J. Atmos. Sci.*, **67** (10), 3113–3129, doi:10.1175/2010JAS3412.1.
- Voldoire, A., and Coauthors, 2017: SURFEX v8.0 interface with OASIS3-MCT to couple atmosphere with hydrology, ocean, waves and sea-ice models, from coastal to global scales. *Geosci. Model Dev.*, **10**, 4207–4227, doi:10.5194/gmd-10-4207-2017.
- Waliser, D., and Coauthors, 2009: MJO simulation diagnostics. *J. Climate*, **22**, 3006–3030, doi:10.1175/2008JCLI2731.1.
- Waliser, D. E., K. M. Lau, and J.-H. Kim, 1999: The influence of coupled sea surface temperatures on the Madden–Julian oscillation: A model perturbation experiment. *J. Atmos. Sci.*, **56** (3), 333–358, doi:10.1175/1520-0469(1999)056<0333:TIOCSS>2.0.CO;2.
- Wang, B., 1988: Dynamics of tropical low-frequency waves: An analysis of the moist Kelvin wave. *J. Atmos. Sci.*, **45** (14), 2051–2065, doi:10.1175/1520-0469(1988)045<2051:DOTLFW>2.0.CO;2.
- Wang, B., 2005: *Theory*. In: *Intraseasonal Variability in the Atmosphere–Ocean Climate System*, 307–360. Springer Praxis Books (Environmental Sciences). Springer, Berlin, Heidelberg, doi:10.1007/3-540-27250-X_10.
- Wang, B., and X. Xie, 1997: A model for the boreal summer intraseasonal oscillation. *J. Atmos. Sci.*, **54** (1), 72–86, doi:10.1175/1520-0469(1997)054<0072:AMFTBS>2.0.CO;2.
- Wang, B., and X. Xie, 1998: Coupled modes of the warm pool climate system. Part I: The role of air–sea interaction in maintaining Madden–Julian oscillation. *J. Climate*, **11** (8), 2116–2135, doi:10.1175/1520-0442(1998)011<2116:CMOTWP>2.0.CO;2.
- Weare, B. C., 2003: Composite singular value decomposition analysis of moisture variations associated with the Madden–Julian oscillation. *J. Climate*, **16**, 3779–3792.

- Webster, P. J., and R. Lukas, 1992: TOGA COARE: The coupled ocean–atmosphere response experiment. *Bull. Amer. Meteor. Soc.*, **73** (9), 1377–1416, doi:10.1175/1520-0477(1992)073<1377:TCTCOR>2.0.CO;2.
- Wheeler, M. C., and H. H. Hendon, 2004: An all-season real-time multivariate MJO index: Development of an index for monitoring and prediction. *Mon. Wea. Rev.*, **132**, 1917–1932.
- Wilcox, E. M., and V. Ramanathan, 2004: The impact of observed precipitation upon the transport of aerosols from South Asia. *Tellus B: Chemical and Physical Meteorology*, **56** (5), 435–450, doi:10.3402/tellusb.v56i5.16464.
- Woolnough, S. J., F. Vitart, and M. A. Balmaseda, 2007: The role of the ocean in the Madden–Julian oscillation: Implications for MJO prediction. *Quart. J. Roy. Meteor. Soc.*, **133** (622), 117–128, doi:10.1002/qj.4.
- Woolnough, S. J., and Coauthors, 2010: Modelling convective processes during the suppressed phase of a Madden–Julian oscillation: Comparing single-column models with cloud-resolving models. *Quart. J. Roy. Meteor. Soc.*, **136** (647), 333–353, doi:10.1002/qj.568.
- Wu, X., L. Deng, X. Song, G. Vettoretti, W. R. Peltier, and G. J. Zhang, 2007: Impact of a modified convective scheme on the Madden–Julian Oscillation and El Niño–Southern Oscillation in a coupled climate model. *Geophys. Res. Lett.*, **34** (16), L16 823, doi:10.1029/2007GL030637.
- Xie, Y.-B., S.-J. Chen, I.-L. Zhang, and Y.-L. Hung, 1963: A preliminarily statistic and synoptic study about the basic currents over southeastern Asia and the initiation of typhoons. *Acta Meteorologica Sinica*, **33**, 206–217.
- Xu, W., and S. A. Rutledge, 2014: Convective characteristics of the Madden–Julian oscillation over the central Indian Ocean observed by shipborne radar during DYNAMO. *J. Atmos. Sci.*, **71** (8), 2859–2877, doi:10.1175/JAS-D-13-0372.1.
- Yano, J.-I., and K. Emanuel, 1991: An improved model of the equatorial troposphere and its coupling with the stratosphere. *J. Atmos. Sci.*, **48** (3), 377–389, doi:10.1175/1520-0469(1991)048<0377:AIMOTE>2.0.CO;2.
- Yoneyama, K., and D. B. Parsons, 1999: A proposed mechanism for the intrusion of dry air into the tropical Western Pacific region. *J. Atmos. Sci.*, **56** (11), 1524–1546, doi:10.1175/1520-0469(1999)056<1524:APMFTI>2.0.CO;2.

- Yoneyama, K., C. Zhang, and C. N. Long, 2013: Tracking pulses of the Madden–Julian oscillation. *Bull. Amer. Meteor. Soc.*, **94**, 1871–1891, doi:10.1175/BAMS-D-12-00157.1.
- Yoneyama, K., and Coauthors, 2008: MISMO field experiment in the equatorial Indian Ocean. *Bull. Amer. Meteor. Soc.*, **89** (12), 1889–1904, doi:10.1175/2008BAMS2519.1.
- Yu, J.-Y., and J. D. Neelin, 1994: Modes of tropical variability under convective adjustment and the Madden–Julian Oscillation. Part II: Numerical results. *J. Atmos. Sci.*, **51** (13), 1895–1914, doi:10.1175/1520-0469(1994)051<1895:MOTVUC>2.0.CO;2.
- Zhang, C., 2005: Madden–Julian oscillation. *Rev. Geophys.*, **43**, RG2003–2005, doi:10.1029/2004RG000158.
- Zhang, C., 2013: Madden–Julian oscillation: Bridging weather and climate. *Bull. Amer. Meteor. Soc.*, **94** (12), 1849–1870, doi:10.1175/BAMS-D-12-00026.1.
- Zhang, C., J. Gottschalck, E. D. Maloney, M. W. Moncrieff, F. Vitart, D. E. Waliser, B. Wang, and M. C. Wheeler, 2013: Cracking the MJO nut. *Geophys. Res. Lett.*, **40**, 1223–1230, doi:10.1002/grl.50244.
- Zhang, C., and J. Ling, 2017: Barrier effect of the Indo-Pacific Maritime Continent on the MJO: Perspectives from tracking MJO precipitation. *J. Climate*, **30** (9), 3439–3459.
- Zhang, C., and K. Yoneyama, 2017: *CINDY/DYNAMO field campaign: Advancing our understanding of MJO initiation*. In: *World Scientific Series on Asia–Pacific Weather and Climate*, World Scientific Series on Asia–Pacific Weather and Climate, Vol. 9, 339–348. World Scientific Publishing Co. Pte Ltd, doi:10.1142/9789813200913_0027.
- Zhang, G. J., and M. Mu, 2005: Simulation of the Madden–Julian oscillation in the NCAR CCM3 using a revised Zhang–McFarlane convection parameterization scheme. *J. Climate*, **18** (19), 4046–4064, doi:10.1175/JCLI3508.1.
- Zhang, G. J., and X. Song, 2010: Convection parameterization, tropical Pacific double ITCZ, and upper-ocean biases in the NCAR CCSM3: Part II. Coupled feedback and the role of ocean heat transport. *J. Climate*, **23** (3), 800–812.
- Zhou, S., and A. J. Miller, 2005: The interaction of the Madden–Julian oscillation and the Arctic Oscillation. *J. Climate*, **18** (1), 143–159, doi:10.1175/JCLI3251.1.